



<https://theses.gla.ac.uk/>

Theses Digitisation:

<https://www.gla.ac.uk/myglasgow/research/enlighten/theses/digitisation/>

This is a digitised version of the original print thesis.

Copyright and moral rights for this work are retained by the author

A copy can be downloaded for personal non-commercial research or study,
without prior permission or charge

This work cannot be reproduced or quoted extensively from without first
obtaining permission in writing from the author

The content must not be changed in any way or sold commercially in any
format or medium without the formal permission of the author

When referring to this work, full bibliographic details including the author,
title, awarding institution and date of the thesis must be given

Enlighten: Theses

<https://theses.gla.ac.uk/>
research-enlighten@glasgow.ac.uk

CONTRIBUTIONS TO THE PREDICTION OF LOW REYNOLDS

NUMBER AEROFOIL PERFORMANCE

by

Frank N. Coton, B.Sc.

Dissertation submitted to the Faculty of Engineering, University of
Glasgow, for the Degree of Doctor of Philosophy

November, 1987

© F.N. Coton, 1987

ProQuest Number: 10948176

All rights reserved

INFORMATION TO ALL USERS

The quality of this reproduction is dependent upon the quality of the copy submitted.

In the unlikely event that the author did not send a complete manuscript and there are missing pages, these will be noted. Also, if material had to be removed, a note will indicate the deletion.



ProQuest 10948176

Published by ProQuest LLC (2018). Copyright of the Dissertation is held by the Author.

All rights reserved.

This work is protected against unauthorized copying under Title 17, United States Code
Microform Edition © ProQuest LLC.

ProQuest LLC.
789 East Eisenhower Parkway
P.O. Box 1346
Ann Arbor, MI 48106 – 1346

CONTENTS

	Acknowledgements	i
	Abstract	ii
	Nomenclature	iii
Chapter 1	Introduction	1
1.1	Overview	1
1.2	Low Reynolds Number Aerofoils	4
1.3	Specific Aerofoil Analysis Code Requirements	10
1.4	Current Analysis Schemes	14
1.5	Description of the Present Analysis Technique	18
Chapter 2	Potential Flow Calculation	22
2.1	Introduction to Basic Model	22
2.2	Separated Flow Modelling	25
2.3	Modelling of Laminar Separation Effects	30
2.4	Inviscid Analysis with Short Separation Bubble	33
Chapter 3	Boundary Layer Calculation	35
3.1	Introduction	35
3.2	Detailed Procedure Adopted	37

3.3	Laminar Boundary Layer	39
3.4	Turbulent Boundary Layer Calculation	47
3.5	Transition	50
Chapter 4	Development of a Long Separation Bubble Reattachment Criterion	52
4.1	Introduction	52
4.2	Separated Shear Layer	57
4.3	Reattachment Criterion	61
4.4	Results of the Reattachment Criterion for the GU25-5(11)8 Aerofoil.	63
4.5	General Application of the Criterion	65
Chapter 5	Extension of the Boundary Layer Calculation to Separated Flow	67
5.1	Introduction	67
5.2	Extension of the Laminar Boundary Layer Calculation	70
5.3	Application of the method to Laminar Separation Problems	81
5.4	Extension of the Turbulent Boundary Layer Calculation	84
5.5	Comparitive Studies	87
5.6	Separation Bubble Calculations Based on Horton's Method	91

Chapter 6	Results of the Predictive Scheme	93
6.1	Introduction	93
6.2	GU25-5(11)8	94
6.3	Wortmann FX63-137	97
6.4	GA(W)-1	99
6.5	NACA 4412 and NACA 4415	103
6.6	NACA 23012	106
6.7	Gottigen GO 797	109
Chapter 7	Conclusions	110
	Appendices	113
Appendix 1:	Calculation of Vortex Panel Influence Coefficients	113
Appendix 2:	Calculation of Separation Panel Influence Coefficients	115
Appendix 3:	Inviscid Wake Calculation	117
Appendix 4:	Calculation of the Bubble Panel Influence Coefficient	120
Appendix 5:	Derivation of the Equations of Le Foll From the Standard Form	122
Appendix 6:	Horton's Separation Bubble Growth Prediction Method	127
	References	132
	Tables	140
	Figures	142

ACKNOWLEDGEMENTS

A large number of individuals have, at some time, been involved in this project and have made invaluable contributions, without which certain aspects of the work may not have been successful. In particular, the author would wish to express his appreciation to Dr. Roderick Galbraith who, throughout the programme, provided guidance, encouragement and, often, a new perspective on seemingly insoluble problems. The author would also wish to acknowledge the support and encouragement of Professor Bryan Richards, and Mr. Peter Swan who, as external supervisor, provided many useful observations on the practical applications of the work.

Thanks are also due to Miss Margaret Simpson, Aeronautics and Fluid Mechanics Departmental Secretary, for her assistance in the preparation of this document, and to Dr. Douglas Thomson for his advice on certain computational matters in the initial stages. The author would also like to express his appreciation to Mrs. Linda McCormick whose technical support and advice were inestimable.

A debt of deepest gratitude is also owed to the authors parents and grandparents for their encouragement and financial support, and to Miss Sheila Duncan for her understanding when things did not go smoothly.

Finally, the author would wish to thank the Science and Engineering Research Council and British Aerospace Plc. who, under CASE award No. EB 048, provided the finance for this project.

ABSTRACT

The dominant aspects of low Reynolds number flows are identified and their relevance to aerofoil performance discussed. A method for assessing two-dimensional aerofoil performance characteristics, including trailing edge and gross laminar separation, is developed, along with a subsidiary direct boundary layer calculation scheme capable of accounting for short laminar separation bubbles.

The constituent parts of the performance prediction scheme, which consists a vortex panel method with boundary layer corrections and an inviscidly modelled wake, are described in some detail. Predictions obtained for both laminar and turbulent separation are also presented. For laminar separation, an inviscid Wake Factor Increment correlation is developed to account for the effects of the free laminar shear layers. Generally, the predictions of lift and pitching moment may be considered to be within the experimental error, but where this is not the case, the applicability of the modelling technique is discussed.

The developed direct boundary layer calculation technique is demonstrated to provide an indication of the boundary layer growth through a separation bubble for a prescribed pressure distribution whilst encountering no difficulty at separation. Comparisons with inverse calculations are made and exhibit good general agreement.

Finally, the general applicability of the predictive scheme is discussed along with possible future enhancements.

NOMENCLATURE

CD	Dissipation coefficient	$\frac{2}{\rho u_e^2} \int_0^{\delta} \tau(y) \frac{du}{dy} dy$
Cd	Drag coefficient	
C _f	Skin friction coefficient	
C _L	Lift coefficient	
C _{Lmax}	Maximum lift coefficient	
C _{mq}	Pitching moment coefficient about quarter chord	
C _p	Pressure coefficient	
D*	Dissipation integral from Head's method	
E	Kinetic energy dissipation	$\rho \epsilon \frac{u_e^3}{2}$
f, f ₁ , f ₂ , f ₃	Velocity profile shape functions	
F ₁ , F ₂	Shear layer departure angles	
F(n), G(n)	Approximate velocity profiles	
G	Rotta-Clauser form factor	$\frac{H - 1}{H\sqrt{C_f}/2}$
H	Momentum form parameter	δ^*/θ
H _ε	Energy form parameter	ϵ/θ
L	Ordinate of Le Foll's plane	
l	Velocity profile parameter from Head's method	
l _t	Length of laminar separation bubble prior to transition	
l ₂	Length of laminar separation bubble after transition	
l _b	Total separation bubble length	
L _j	Vortex panel length	
L _s	Length from corner point to separation	
M	Semi-empirical function of Le Foll's method	
m	Velocity profile parameter of Head's Method	

\vec{n}	Panel normal vector
q	Boundary layer calculation velocity term $\ln \frac{u_e}{U_0}$
Re_θ	Momentum thickness Reynolds number
Re_c	Chord Reynolds number
Re_δ^*	Displacement thickness Reynolds number
Re_s	Reynolds number based on surface distance
s, y	Coordinates along and normal to surface
Sc	Distance from vortex panel corner point to control point
TF	Taylor's turbulence factor
Tu	Turbulence intensity
t^*	Boundary layer calculation term in Head's method $\left[\frac{\theta}{c} \right]^2 Re_c$
u, v	Velocities within the boundary layer in the s,y directions
u', v'	Boundary layer fluctuation velocities in the s,y directions
U_0	Freestream velocity
u_e	Velocity at edge of boundary layer
\bar{U}	$\frac{u_e}{U_0}$
u_τ	Friction velocity $\sqrt{\tau_w/\rho}$
\vec{V}_∞	Freestream velocity vector
WF	Wake factor
WFI	Wake factor increment
WH	Wake height
WL	Wake length
x,y	Coordinates of cartesian plane
X	Abscissa of Le Foll's plane
y^+	Boundary layer thickness Reynolds number $\frac{u_\tau y}{\nu}$
α	Angle of Attack

β	Aerofoil trailing edge angle for wake analysis
γ	Vorticity
Γ	Head's pressure gradient parameter $\frac{\theta^2}{\nu} \frac{du}{ds}$
δ	Boundary layer thickness
δ^*	Boundary layer displacement thickness
ϵ	Boundary layer energy thickness
ζ	Mean wake direction angle
η	y/δ
θ	Boundary layer momentum thickness
Λ_R	Horton's reattachment parameter $\left[\frac{\theta}{u_e} \frac{du_e}{ds} \right]_R$
λ	Wake iteration modification angle
μ	Absolute viscosity
ν	Kinematic viscosity
Π	Coles' wake parameter
π_1	Equilibrium parameter $\frac{\delta^*}{\tau_w} \frac{dp}{ds}$
ρ	Density
τ	Shear stress
ϕ	Velocity potential

Subscripts

c	Chord
i	i th term
j	j th term
n	normal
s	Surface distance (inviscid calculation)

sep **Separation**
t **Transition**
 θ_{tr} **Momentum thickness at transition**

CHAPTER 1

INTRODUCTION

1.1 Overview

The recent upsurge of interest in low Reynolds number aerofoil performance has provided a deeper understanding of the inherent flow phenomena and has thus, to some extent, produced a requirement for appropriate analysis techniques (Ref. 1). Much of this interest has been stimulated by the development of remotely piloted vehicles (R.P.V's) (Ref.1) which include such devices as high altitude aircraft platforms and mini target, or decoy, drones etc. Other devices (Fig.1.1) (Ref. 2) employing an aerofoil operating in the low Reynolds number regime as a prime element, include wind turbines, man-powered vehicles and aeromodels. For the purposes of this study, the low Reynolds number regime was considered to cover the range $5 \times 10^4 < Re < 1 \times 10^7$. The upper limit of this range, whilst possibly somewhat above that normally taken as the upper limit (Ref. 1), was considered to provide a realistically achievable operating range for any developed aerofoil analysis scheme.

The performance of an aerofoil section at low Reynolds numbers, especially in the range $Re < 1.5 \times 10^6$ is dependent on its specific application and the associated flow phenomena present (Ref. 3).

Interpretation of test results is therefore fraught with difficulties and requires careful consideration of, not only the test facility, but also

its relevance to the full scale application (Ref. 2). Indeed, it is often the case that data collected in one facility, for a particular aerofoil section, may be quite different from that obtained via a different facility (Fig. 1.2) (Ref. 4). It is this lack of correspondence between, not only the full scale machine and the test model, but also, between different test facilities which prevents simplistic extrapolation from the model test to the full scale machine.

Design of aerofoil sections at low Reynolds number has, in the past, relied heavily on extensive wind tunnel testing, with often a 'try it and see' approach being adopted (Ref. 5). This process was considerably hampered by the above-mentioned lack of correlation between the test data and the result achieved on the full scale machine. Recently (Ref. 6), a greater awareness of the influencing disturbance factors has allowed the designer to specify, more accurately, the exact conditions under which the aerofoil section will operate, and so to assess the applicability of any test results obtained. The design process (Ref. 7), however, could be accelerated if a reliable predictive technique for assessing aerofoil performance in this Reynolds number regime was available. The advantages of this type of method would be such that apart, from aerofoil performance predictions, it may be possible to assess the effects of in-flight contamination and the tolerance of the design to build specifications by calculating the performance of suitably distorted profiles. Such an approach may ultimately produce a more robust design at relatively low cost. Unfortunately, the ability of current methods (Refs. 8,9) is such that the final choice of aerofoil section remains in the domain of the wind tunnel test. This is principally due to the uncertainty, especially in the region of stall, with which current predictive schemes specify the

point of boundary layer separation. If, however, for a specified range of aerofoil types, it were possible to predict the separation location to within experimental uncertainties, it would add confidence to the use of computer based analysis codes for the prediction of two-dimensional aerofoil performance at low Reynolds numbers.

In order that a predictive scheme be developed it was necessary to identify the specific low Reynolds number requirements of such a technique. To do this, the background to the low Reynolds number problem and the associated flow phenomena were examined in some detail.

1.2 Low Reynolds Number Aerofoils

Our present understanding of low Reynolds number aerofoil flow has developed over a number of years (Ref. 1). The work carried out has, in the past, been for several different applications and has only recently been brought together to give a coherent view of the problem (Ref. 5). Before discussing the contemporary concept of low Reynolds number aerofoil flow it is convenient to outline it's major historical development.

1.2.1 Historical Background

The introduction of the boundary layer concept by Ludweig Prandtl (Ref. 10) in 1904 marked the first step in the understanding of the low Reynolds number problem. This was followed by a series of tests in the mid 1930's, on aerofoils at low Reynolds numbers in the NACA variable density wind tunnel (Ref. 11). The results obtained from these test were, as a consequence of the high test turbulence levels, quite unrepresentative of the associated free flight conditions, but provided the first indication of how the performance of different aerofoil sections varied as the Reynolds number was reduced.

As with many of the low Reynolds number studies conducted at that time, the work of Schmidt (Ref.12) was inspired by model aircraft. In his prize winning paper of 1940, a low turbulence test facility was employed and the dependance of aerofoil performance on such parameters as stream turbulence, thickness/chord ratio, boundary layer tripping and leading edge radius were examined. The paper also provided the first indications of the phenomenon of hysteresis.

Between then and the early 1970's few research initiatives on this topic were reported, although, of the studies conducted, those of McCullough and Gault (Ref. 13) and Gault (Ref. 14) are of particular note. The former provided a detailed explanation of the various stalling mechanisms and the latter produced data incorporating separation bubbles which is still used to assess predictive schemes today. Further understanding of the separation bubble phenomenon came from the work carried out at Queen Mary college (Refs. 15 & 16).

The recent interest in the field has prompted a number of investigations (Ref. 1) into the specific flow phenomena associated with low Reynolds numbers. This approach has resulted in the isolation of the governing test parameters although, as yet, assessment of their effect is confined to the qualitative rather than the quantitative domain. The enhanced understanding of these phenomena has provided the basis for the development of predictive schemes specific to low Reynolds numbers. Even so, numerical modelling of such flows has not yet reached the accuracy levels of the equivalent higher Reynolds number procedures. The reason for this lies in the inability of the present aerofoil analysis schemes to identify the occurrence of, and to model, the relevant flow phenomena.

1.2.2 Present Understanding of the Overall Flowfield

The changing behaviour of the flowfield around an aerofoil as the Reynolds number is reduced below 1.5×10^6 is difficult to generalise. It is, however, possible to identify the main features of the flow for a 'standard' aerofoil at a mid-range incidence through this region. Figure 1.3 presents a series of diagrams which indicate the behaviour of

the viscous shear layer on the upper surface of the aerofoil as the Reynolds number is reduced. It is likely that for Reynolds numbers above 1.5×10^6 , the boundary layer undergoes natural transition with the subsequent turbulent boundary layer either remaining fully attached towards the trailing edge, or exhibiting a small amount of separation.

With a reduction in the freestream Reynolds number, it is possible that the location of natural transition moves aft of the laminar separation point. If this occurs, then the free shear layer would undergo transition shortly after separation, and the increased entrainment associated with the turbulent free shear layer would normally result in reattachment taking place, so forming a "laminar separation bubble". As a result of this 'bubble' transition, the subsequent attached turbulent boundary layer would probably be thicker than that produced as a result of natural transition (Ref. 17). As a consequence of this increased thickness, the layer may be more prone to trailing edge separation. The effect of such a short bubble, on the pressure distribution, would be to cause a small perturbation in the region of the bubble together with an associated slight reduction in the achieved suction peak (Ref. 18). Otherwise, the normal operating characteristics of the aerofoil are little affected.

A further reduction in Reynolds number normally results in the length of the separation bubble being increased. Initially, it is likely, the rate of increase would be small, and although a slight enhancement of the trailing edge separation may occur due to the thickening turbulent boundary layer, the overall performance of the aerofoil would be relatively unaffected. This, however, is unlikely to apply in the stall

region where the separation bubble behaviour would be more influential. Leading edge stall is related to separation bubble behaviour, in that, a reduction in Reynolds number may result in earlier bubble burst and, hence, early stall.

The rate of growth of the separation bubble would increase with any subsequent decrease in Reynolds number until the free shear layer fails to reattach and gross laminar separation results. The increase in bubble length is accompanied by an associated reduction in suction peak with the pressure distribution exhibiting the features of gross laminar separation.

Generally, the performance of an aerofoil deteriorates in accordance with the above progression, as the Reynolds number is reduced. This, however, is not always the case, as can be seen in Fig. 1.4 where, although the value of C_{lmax} for five of the aerofoils does reduce with Reynolds number, the performance of the G0 387 does not (Ref. 19). This type of behaviour is linked to the prime importance of the boundary layer and, specifically, the influence of separation and the separation bubble, on the overall flowfield. Whilst the degree of trailing edge separation is the governing factor in the lift produced by the aerofoil, it is the effect of the separation bubble which often causes anomalies between different sections and is particularly difficult to model.

Figure 1.5 presents a recent description of the structure of a short laminar separation bubble as given by Venkateswarlu and Marsden (Ref. 5). This diagram illustrates the deformation of the boundary layer velocity profile through the bubble and the area directly behind it in which a non-equilibrium boundary layer initially develops. It is interesting to

note, that the length of the laminar portion of the bubble is almost eighty percent which is in agreement with the earlier findings of Gault (Ref. 14). The influence which the non-equilibrium condition of the reattaching boundary layer has on it's subsequent development downstream is difficult to assess, although, it is likely that, in the case of a long bubble, the effect could be quite significant.

The location of transition within the free shear layer, and indeed in an attached boundary layer at low Reynolds number, may also have a considerable effect on the separation characteristic of an aerofoil. It is often the sensitivity of this location to extraneous flow factors that produces the published inconsistencies between measured data (Ref.4). Parameters such as surface finish, free stream turbulence, vibration and noise may all affect a wind tunnel test and thus the location of transition. It follows from this, that the environment in which the full scale machine operates will also be significant and that any aerofoil test should recreate the operating conditions as closely as possible. Generally, the sensitivity of the aerofoil's performance to these effects increases with a reduction in Reynolds number, with the region $Re \leq 5 \times 10^5$ being particularly affected. An example of this was given by Mueller (Ref. 20) who demonstrated that the lift of the NACA 66₃-018 aerofoil could be influenced by sound. In his experiment, he surrounded the flow with a fixed noise level at an adjustable frequency and obtained the lift coefficient variation given in Fig. 1.6 by simply varying the frequency of the sound. The obvious lift enhancement achieved in a narrow frequency range was due to transition being triggered by the noise input.

To control these effects, much effort has been devoted to the

development of low-disturbance/turbulence test environments (Ref. 1).

While the data obtained via these facilities may be relevant to high altitude applications, where turbulence levels are very low, it is unclear whether the data could be applied with as much confidence to a small low-altitude vehicle. Since the analysis of the disturbance environment is still the subject of current research programs, it is likely that the most useful design data may be obtained by comparative tests using the same facility.

1.3 Specific Aerofoil Analysis Code Requirements

The prediction of the flowfield described above is a complex problem which requires the accurate specification of several vital parameters. The predictive process is hindered by the availability of reliable empirical data to establish the accuracy of any developed scheme. It is, therefore, of fundamental importance that great care is taken when choosing the elements which make up any analysis scheme and, subsequently, when assessing its performance.

In order to define the predictive aims of a low Reynolds number aerofoil analysis scheme, it is convenient to split the previously described flowfields, encountered as the Reynolds number is reduced, into four distinct areas. These are

1. Laminar-turbulent boundary layer, natural transition, turbulent separation or fully attached flow.
2. Laminar-turbulent boundary layer, separation bubble transition, turbulent separation or attached at trailing edge.
3. Laminar-turbulent boundary layer, long separation bubble transition, turbulent separation or attached at trailing edge.
4. Laminar boundary layer, no transition, gross laminar separation.

The first category relies on the accurate specification of the location of natural transition coupled with a good prediction of any trailing edge

separation that may be present. It may be considered that the effects of extraneous flow influences would be minimal in this regime, and so adjustment of any calculative parameters to account for these would be unnecessary.

When a short separation bubble is present on the upper surface of an aerofoil, then, provided the bubble is small, the turbulent boundary layer formed behind it would exhibit the essential features of that which would result from a natural transition near the point of laminar separation. Whilst this is only strictly true for very short bubbles, transition of the boundary layer at the laminar separation point would be a good approximation to the bubble effect for most cases. It was therefore decided that, initially, modelling of short separation bubbles by fixing transition at the laminar separation point would be satisfactory for the required purpose.

A drawback of the above approach, to separation bubble modelling, arises from the inability to identify when the approximation ceases to be applicable to the considered case. This difficulty is linked to the problem which the designer faces when interpreting wind tunnel data which exhibit separation bubbles. It would, to alleviate this problem, be useful to be able to assess separation bubble effects on the turbulent boundary layer behaviour and subsequent separation characteristics. The development of the capability to calculate the boundary layer behaviour through a separation bubble was therefore envisaged as a useful addition to any forthcoming analysis scheme. It was considered that any such calculation need not necessarily be an integral part of the performance prediction scheme, but rather a subsidiary routine. This would permit the

effect of a separation bubble, on aerofoil performance, to be estimated either via the analysis scheme, or directly from an empirically obtained pressure distribution. Such a feature would enable the routine to be used as a direct aid to wind tunnel tests.

The pressure distribution associated with a long separation bubble, as previously indicated, is considerably different to that produced by a short bubble. The resultant discrepancy between the obtained pressure distribution and an inviscid solution, makes modelling of this phenomenon a difficult process. For the purposes of a low Reynolds number design procedure, it may not be necessary to model this particular flow regime since the loss of performance generally associated with it would be undesirable within any aerofoil's operating range. Identification of this region would, however, be useful to allow assessment of the rate and severity of the bubble growth dependant lift degradation. To do this, the Reynolds number at which free shear layer reattachment just fails to occur would require prediction, along with the performance of the aerofoil with a stable short separation bubble. Further to this, an indication of the rate of bubble growth, from the stable short separation bubble condition to the fully separated laminar flow regime, would be desirable to permit identification of the growth region's upper limit.

It follows from the above, that the performance of an aerofoil exhibiting gross laminar separation would require prediction to allow the performance at the lower end of the growth region to be assessed. Accurate specification of the point of laminar separation and the modelling of the laminar shear layer dominated wake would therefore be of considerable importance to any developed analysis scheme.

To predict the above phenomena, it was necessary to develop an analysis scheme which would be applicable to all the required flow regimes listed above, and be of practical use to the aerofoil designer.

1.4 Current Analysis Schemes

As previously indicated, separated flow over an aerofoil, as opposed to the fully-attached case, exhibits gross viscous effects which cannot be approximated by the inviscid calculation satisfying the classical Kutta condition. Such calculations (Ref. 21) fail in the region of stall by over-predicting the lift coefficient as a consequence of neglecting separation. It is therefore necessary, for low Reynolds numbers, to account for these viscous effects if an accurate performance prediction is to be obtained. Existing analyses of these flows via the appropriate Navier-Stokes equations are costly, and currently yield results no better than simpler contemporary codes (Ref. 1). These simpler methods (Refs. 22,23,24), commonly employ a viscid-inviscid interaction scheme in which the appropriate displacement and local separation corrections are indicated by a viscous boundary layer calculation, whilst the compatible inviscid calculation is, generally, by means of a standard panel method. The two computations are iteratively adjusted with respect to each other until some convergence criterion is satisfied.

The viscid-inviscid interaction techniques fall into two categories, i.e. direct and semi-inverse. Although the various approaches used to model the constituent parts of such schemes may vary, the overall flowfield can generally be split into three distinct regions for modelling purposes (Fig. 1.7). These are

- a) Potential Flow (inviscid) Region
- b) Boundary Layer (viscous) Region
- c) Wake (separated flow) Region

Potential Flow Region: A region existing away from the immediate locality of the aerofoil surface, which is virtually irrotational, since the shear is so low that viscous stresses impart a rotation to the fluid which may be considered irrotational. The region can, therefore, be considered to be a potential flow problem without incurring significant errors.

Boundary Layer Region: The boundary layer is the thin region of flow close to the aerofoil surface in which high shear creates vorticity and the no-slip condition at the surface is satisfied.

Wake Region: Once separation has occurred on an aerofoil, a trailing wake is formed. This wake is taken to be bounded by free shear layers which are rotational but with moderate shear. The wake itself, is a region of low vorticity and small viscous stresses.

1.4.1 Comparison of Semi-inverse and Direct Aerofoil Analysis Schemes

In both types of scheme, the inviscid part of the calculation is carried out by a numerical potential flow method, in which the aerofoil profile is represented by either source or vortex panels, or is reconfigured via a conformal mapping technique. This inviscid calculation, in each case, is of the forward type, where the aerofoil shape is input and the velocity field is the required output.

The principle difference between the semi-inverse and direct schemes, however, is to be found in the calculation of the boundary layer and the subsequent matching of this prediction to the inviscid solution. In the direct formulation, the velocity distribution produced by the inviscid

calculation is an input to the boundary layer algorithm from which the appropriate flow displacement effects are obtained. To account for these displacements, either the aerofoil profile shape is adjusted or extra terms are introduced into the inviscid calculation. The inviscid calculation is then repeated. This process continues until the change in lift coefficient between successive iterations is negligible.

In the semi-inverse formulation, a functional relationship is derived between some boundary layer parameter and a characteristic (e.g. source strength) of the potential flow method, allowing the local velocity distribution at the edge of the boundary layer to be predicted. The chosen characteristic is then adjusted with respect to the discrepancy between the two solutions, after the velocity distributions from the two component parts have been obtained. This process is then repeated until some convergence criterion is satisfied.

If flow separation exists on the considered aerofoil then, in the direct scheme of Dvorak and Maskew (Ref. 22), the separated wake is calculated inviscidly with the boundary layer algorithm providing the separation point. The wake is then calculated iteratively from an initial estimate, with the length/height ratio of the wake being an empirically derived input.

The casting of the boundary layer problem in the inverse mode allows the point of separation to be passed by the viscous part of a semi-inverse scheme. After separation, however, a higher order approximation to the Navier-Stokes equations is generally used to continue the viscous calculation (Ref. 23). The inviscid and viscous calculations are then

matched by means of a deficit calculation and the solution then continues much as in the fully-attached case.

Of the existing methods, those of Williams (Ref. 23), Dvorak and Maskew (Ref. 22) and Cebeci et al. (Ref. 24) are amongst the most successful separated flow predictors. All of these methods, however, have significant drawbacks associated with their performance at low Reynolds numbers, in that, so far, none of these schemes can predict regions of laminar separation or, to any degree of accuracy, the effects associated with laminar separation bubbles. It was considered that any developed method should, ultimately, be able to predict both of these effects.

1.5 Description of the Present Analysis Technique

The present technique forms the basis of, what is hoped will be, a useful design procedure for low Reynolds number aerofoils. When considering the structure and content of the analysis code, it was necessary to pay some attention to the practical aspects of such a technique. The developed code was therefore perceived as a practical aid to the aerofoil designer, to be used either by itself, or in conjunction with wind tunnel tests. It was felt that a method based on the approach of Dvorak and Maskew (Ref. 22) would provide the greatest degree of versatility, in terms of its constituent parts, and would also permit the effects of gross laminar separation to be accounted for in a relatively straightforward manner. Apart from the application of the full viscous-inviscid interaction technique to aerofoil performance prediction, an analysis scheme of this form would, via the separate viscous and inviscid sections, have other advantages to the designer, namely

1. The treatment of the separated flow region via the inviscid calculation would permit an assessment of the lift coefficient via relatively inexpensive flow visualization tests. This would be achieved by using the empirical separation point as a direct input to the inviscid calculation (Ref. 21) thus providing an estimate of the test section lift and, therefore, reducing instrumentation costs.
2. Application of the direct boundary layer calculation to an empirical pressure distribution would permit analysis of the boundary layer development, and, if a separation bubble were

present, assessment of the bubble's effect on the trailing edge separation characteristics.

The use of empirical separation points, in conjunction with an inviscid calculation incorporating a wake model, has been demonstrated (Ref. 21) to be an accurate aerodynamic force prediction method when the separation points were provided by measured pressure distributions. It is likely that such points, when taken from reliable flow visualization tests, would produce predictions of equivalent accuracy.

The effect of a laminar separation bubble on the separation characteristics of an aerofoil, was highlighted by the recent work of Gleyzes et al. (Ref. 17), which demonstrated the lack of generality associated with the resulting turbulent boundary layer development. If this growth could be assessed directly, from an empirical pressure distribution, then the possible benefits of boundary layer control could be more readily assessed.

Having adopted the above general approach, it was necessary to 'match' the boundary layer calculation to the inviscid solution. This could be achieved, by accounting for the displacement effect of the boundary layer, either by adjusting the aerofoil shape (Ref. 25), or by introducing an equivalent source distribution into the inviscid calculation. It was the former technique which was employed in the developed viscous-inviscid interaction procedure.

For separated flow, it was found that the progress towards calculation convergence was dominated by the separation point movement between

iterations , and, as such, the influence of the effective boundary layer displacement was small. As a result of this, it was only necessary to include viscous displacement effects when the calculation appeared to be nearing convergence. This resulted in a rapid approach to convergence followed by final small corrections, producing consistent results. Generally, convergence was assumed to have been achieved when the separation point forward movement had ceased and it's variance between each iteration was less than 0.5 percent chord.

It was found that the convergence rate was, generally, related to the extent of separation present, with larger amounts of separated flow requiring a greater number of iterations. Normally, however, when a sequence of increasing angles of attack were calculated for the same aerofoil, then the carry over of the position of separation from one incidence to the next, improved computational efficiency.

The developed method, a flow chart of which is presented in Fig. 1.8, has the capability to model either turbulent boundary layer separation towards the trailing edge or, at low Reynolds number, separations associated with the laminar boundary layer close to the leading edge.

Although a capability to model short laminar separation bubbles is not included in the main interaction scheme, a boundary layer calculation capable of predicting the behaviour of such bubbles was developed as a subsidiary routine. This calculative technique was used to predict the effect of separation bubbles, on aerofoils, from empirical pressure distributions. The main interactive scheme does, however, give an indication of long bubble formation by means of a developed long bubble

prediction technique.

Before discussing the results obtained from the predictive scheme, it is appropriate to examine it's constituent parts, and subsidiary routines, in some detail.

POTENTIAL FLOW CALCULATION

2.1 Introduction to the Basic Model

Calculation of the inviscid flow part of a viscid-inviscid interaction scheme is generally achieved by means of either a mapping technique (Ref. 24) or some form of panel method (Ref. 22). Of these two approaches, the former may be more exact, but the latter is much simpler in application and lends itself more readily to inclusion in a practical aerofoil analysis procedure.

In a panel method, the aerofoil contour is replaced by an inscribed polygon on which is placed appropriate singularity distributions. Generally, a combination of source and vortex singularities is distributed in a prescribed manner along the polygon. In the method of Leishman and Galbraith (Ref. 26), however, the aerofoil profile was replaced by panels on which were placed a linearly varying vorticity distribution (Fig 2.1) thus achieving piecewise continuity between adjoining panels. The Kutta condition was therefore independent of panel distribution since it could be applied directly at the trailing edge and not at the mid-points of the last upper and lower panels.

Each of the panels describing the polygon contains a control point at which the condition of flow tangency is applied. This is achieved by

setting the scalar product of the induced velocity with the surface normal vector to zero, and can be represented by the equation

$$\int_C \gamma_s ds + \vec{V}_\infty \cdot \vec{n} = 0 \quad (2.1)$$

The contribution from all the panels gives a linear equation with unknown vorticity values. Repeating this process for each control point yields a set of linear simultaneous equations which, in conjunction with a specified Kutta condition of zero net vorticity at the trailing edge, may be solved to yield the strength of the assumed vortex sheets. Once this strength is known, the required velocity distribution can be obtained from

$$u_e = | \gamma(s) | \quad (2.2)$$

A detailed description of the method used to obtain the influence coefficients for the above equations is contained in Appendix (1).

The distribution of the vortex panels, within the aerofoil contour, is generally such that the higher the curvature of the contour, the shorter the polygonal panels, with the maximum length of a panel being dependant on the appropriateness of the quasi-linear approximation to the continuous vortex sheet strength. Often, only published coordinate data is available to the design engineer and thus, unless some curve fit routine is applied to these data, the polygonal panel distribution is predetermined. In such cases, the method has been shown to perform well (Ref. 26) since, generally, aerofoil section coordinate data is presented in a similar form to that required by the algorithm.

This algorithm was used as the basis for the potential flow analysis within the overall aerofoil performance prediction scheme.

2.2 Separated Flow Modelling

The inviscid flow analysis method of Leishman et al. (Ref. 21), developed from the above panel method, was used to model the inviscid flowfield and associated wake. This algorithm exhibits the essential features of the method of Dvorak and Maskew (Ref. 22) but with some important numerical differences. In it, free shear layers, on which are placed panels of uniform vorticity are used to model the aerofoil wake with the aerofoil contour modelled in the above manner. The distribution of all the vortex panels is illustrated in Fig. 2.2.

The modelled wake region is assumed to be inviscid with negligible vorticity, and is taken to have a constant total pressure which is lower than that of the freestream. It is further assumed that the free shear layers have no significant thickness and can be represented as streamlines across which there exists a velocity jump. As the shape of these shear layers is an unknown, it must be calculated from some initial estimate.

Since the panels which make up the shear layers are assumed to have constant vorticity, application of the condition of flow tangency at each control point produces the equation

$$\int_C \gamma(s) ds + \gamma_n \left[\int_l C ds - \int_u C ds \right] + \vec{V}_\infty \cdot \vec{n} = 0 \quad (2.3)$$

where l and u represent the lower and upper free shear layers respectively, and γ_n is the vorticity value on the lower surface trailing edge. This value, via the applied Kutta condition, is equal and opposite to the vorticity value at the upper surface separation point. In this

case, the total influence coefficient for the whole shear layer is obtained by the simple addition of the individual panel contributions. Thus N equations of this form can be generated.

The position of upper surface separation, which dictates the subsequent wake development, is given by the viscous boundary layer calculation and is not permitted to occur at panel corner points. When separation does occur on a panel, the panel is effectively split in three and treated as given in Appendix 2. In this way, the total influence due to the vorticity distributions on the panel containing the separation point was obtained. It was found that if the separation point lay close to, and just in front of, the panel control point, wake convergence did not occur (Fig. 2.3). This appeared to be due to the proximity between the shear layer and the control point (Fig. 2.4). When this occurred, the position of the control point was adjusted so that it always lay in front of the calculated separation point. Although this alleviated the problem, the positioning of the control point, between the panel leading corner point and the location of separation, limited the relative nearness of the separation point to the front of the panel. If, therefore, the separation point lay too close to the front of a panel, it was moved onto the rear of the preceding panel. This shift represented, at worst, a 0.5% chord movement in separation point and so was felt to be, generally, well within the accuracy of the separation prediction. On the lower surface, separation was fixed to occur at the trailing edge.

The inclusion of the above value of separation vorticity produced an extra unknown into the calculation, giving $N+1$ unknowns and N equations. This problem was overcome by setting the upper surface trailing edge

vorticity value to zero and thus squaring the matrix. The influence coefficients due to γ_{sep} were placed into the blank column of the matrix.

Although, during the calculation, the separation point was given by the boundary layer analysis, the shape of the two free shear layers was not known a priori. In a previous investigation (Ref. 27), it was found that the overall flowfield was sensitive to the wake geometry and that parabolic curves, with an intersection point just downstream of the trailing edge, provided a sensible initial approximation. This approach, due to Dvorak and Maskew (Ref. 28), is outlined in Appendix 3. In it, the initial wake estimate is governed by the Wake Fineness Ratio (or Wake Factor) which is the ratio of wake length to height. From this first approximation, the velocity vector at each wake panel control point is determined and a local free shear layer correction angle given by the equation

$$\Delta\lambda_i = \sin^{-1} \left[\frac{\vec{V}_i \cdot \vec{n}_i}{|\gamma_{sep}|} \right] \quad (2.5)$$

is applied to the panel. Finally, the new wake shape is determined by adding each corrected panel to the end of the preceding one in a downstream direction. This process is repeated until the free shear layers lie on, or very close to, streamlines of the flow. The number of iterations required for solution depends on the validity of the initial estimate, although generally, three iterations suffice for moderate amounts of separation with up to six being required for very large separated regions.

As mentioned above, a Wake Factor was used to define the ratio of the wake length to height. For turbulent separation cases, the Wake Factor was taken as a constant for a given aerofoil section, and was related to the aerofoil thickness to chord ratio by using the correlation of Dvorak and Maskew (Ref. 28) (Fig. 2.5). This relation, whilst apparently not completely satisfactory, has been shown to perform well for various aerofoil shapes (Ref. 28).

For fully attached flow, the addition of the boundary layer displacement effect on the aerofoil contour, produced a finite trailing edge. Generally, this would not present any significant problem since the calculation would default to the classical Kutta condition of net zero vorticity between the upper and lower trailing edge. If, however, the boundary layer was very close to separation at the trailing edge, then a sharp discontinuity in the adjusted profile shape appeared because of the layers' excessive growth in that region. This discontinuity manifested itself in a marked pressure peak at the trailing edge (Fig. 2.6) with an accompanying general distortion of the overall distribution. In the developed analysis scheme, a small vortex panel, between 0.995 chord and the trailing edge of the upper surface, with fixed separation occurring on it was added to the polygonal panel distribution. This produced a small wake behind the aerofoil which, due to the increased number of panels concentrated at the trailing edge, stabilized the calculation without any noticeable detrimental effects on the predicted pressure distribution. This approach was used for all fully attached flow cases since it also alleviated any problems posed by similar behaviour of the lower surface boundary layer.

Unfortunately, for laminar separation, the wake shape is influenced by the distance which the free shear layer covers prior to transition and, subsequently, by the rate of wake closure. It was therefore inappropriate to consider a constant Wake Factor for this problem.

2.3 Modelling of Laminar Separation Effects

If, after separation, the free shear layer is predominantly laminar rather than turbulent; then insufficient fluid entrainment occurs for appropriate wake closure. This results in an elongated wake and the need to determine the effect on the Wake Factor. The dominant parameters, in the wake development and closure mechanism, may have been indicated by the work of Horton (Ref. 16) on the related phenomenon of the growth and bursting of laminar separation bubbles. It was indicated that the length of the laminar shear layer could be expressed in the form of a constant Reynolds number based on the boundary layer edge velocity at the point of separation, given in the form

$$\frac{l_t u_e}{\nu} = 4 \times 10^4 \quad (2.6)$$

This equation identified the velocity at separation as the governing parameter in the calculation of the length of the laminar shear layer. Further analysis of the free shear layer closure rate indicated a dependence of it on the boundary layer momentum thickness at the point of transition. Since Horton assumed that the momentum thickness at separation was the same as that at transition, it was felt that the velocity and momentum thickness at the point of separation were likely to be the main influencing factors on the wake shape resulting from laminar separation. It was therefore decided to investigate the influence of the momentum thickness Reynolds number at separation ($R_{\theta_{sep}}$), on the value of Wake Factor necessary for accurate calculation. To achieve this, a comparison of numerically and empirically obtained pressure distributions

for the GU25-5(11)8 aerofoil was made. The best numerically obtained pressure distribution, for a particular case, was determined by successive Wake Factor modifications until good agreement with the empirical distribution was evident. Thus the relevant Wake Factors could be obtained for each case. This process was repeated for a range of angles of attack and for several Reynolds numbers. As an example, Fig. 2.7 presents the results of calculations for the GU25-5(11)8 aerofoil at a Reynolds number of 1×10^5 and an incidence of 12.6 degrees. It can be observed, from this example, that of the three Wake Factors used, only one is appropriate for this particular calculation.

It was clear from the work of Dvorak and Maskew (Ref. 28) that the turbulent separation Wake Factor, which is a constant for a particular aerofoil, would provide the limiting value as the length of the laminar shear layer reduced. For this reason, it was assumed that the effect of laminar separation would be to increment the Wake Factor above the turbulent value. On the basis of this premise, a correlation between $R_{\theta_{sep}}$ and a Wake Factor increment seemed most likely. Figure 2.8 presents the calculated values of Wake Factor increment plotted against $R_{\theta_{sep}}$ along with a tentative correlation which appeared to give a good fit to the data points.

The data used to obtain the increment correlation were measured at a turbulence intensity of 0.5% (Ref. 29) which, for low Reynolds number testing, is relatively high. A correction in the form given below was therefore introduced to allow the use of the correlation at other turbulence intensity levels.

$$WFI = \frac{\text{Log}_{10} (1/\text{TANH}(TU \times 10))}{\text{Log}_{10} (1/\text{TANH}(0.05))} \times WFI_{0.5} \quad (2.7)$$

This correction was based on the turbulence factor effect on a laminar shear layer given by Roberts (Ref. 30) and can only be considered as a first attempt to account for the effects of turbulence. A discussion of the validity of the increment correlation and the results obtained from it is given in Chapter 6.

Over the range of conditions considered, the magnitude of $R_{\theta_{sep}}$ varied little with angle of attack and initial Wake Factor and so permitted the following technique to be used in the predictive scheme. This entailed estimating an initial Wake Factor, for the given condition, from which the value of $R_{\theta_{sep}}$ followed. The Wake Factor increment was then acquired from the correlation of Fig. 2.8 and used in computations for every angle of attack at the relevant free stream Reynolds number. All results for laminar separation presented in Chapter 6 were obtained by this scheme.

2.4 Inviscid Analysis with a Short Separation Bubble

In order to assess the effect of short separation bubbles, a technique was developed to simulate them via an inviscid calculation. It was known, from previous research (Ref. 18), that the presence of a leading edge laminar separation bubble caused a small reduction in peak suction obtained when compared to that resulting from natural boundary layer transition. The loss in lift and earlier stall associated with these bubbles, however, appeared to be related more to the general condition of the subsequent turbulent boundary layer than to this suction peak reduction. A model was therefore constructed in order that this hypothesis be tested.

In the analysis, it was necessary for the considered separation bubble to lie within the bounds of one of the vortex panels which described the aerofoil profile. This constraint was applied to produce a simple model which was nevertheless effective for the required purpose. The location of separation, free shear layer transition and reattachment were taken from Horton's method. If these locations spanned more than one panel then the polygonal panel distribution was adjusted in order that the applied constraint be satisfied. Once this had been completed, a vorticity distribution corresponding to a separation bubble of the correct dimensions, with a constant pressure laminar portion, was imposed on the 'bubble' panel (Fig. 2.9). Since the vorticity values on this 'bubble' could be related to the corner point vorticity values, it was possible to calculate the influence coefficients corresponding to the small perturbation area. The full analysis of this influence coefficient calculation is given in Appendix 4. The method of superposition was then

applied to increment the velocities obtained from the calculation without a bubble by the induced velocities associated with the bubble perturbation.

A typical example of the kind of result obtained by this method is given in Fig. 2.10 where the pressure distributions with and without a separation bubble are compared. The bubble shape has been included in the figure, although, it would normally not be a program output as it would be contained between the two corner points of one panel. There is clearly a reduction in the value of peak suction associated with the separation bubble, but the accompanying loss in lift is very small indeed. From such results, it was clear that an investigation of the role of the turbulent boundary layer in flows containing separation bubbles was necessary. Further results and their implications are discussed in chapter six.

BOUNDARY LAYER CALCULATION

3.1 Introduction

In order to account for the viscous effects present in the flow around any aerofoil, it is necessary to be able to assess the development and subsequent separation of its boundary layers. A number of approximate calculation techniques are in current use for both laminar and turbulent boundary layers (Ref. 31). These methods not only vary in approach, but also in the quality of prediction and the computational speed which they provide. In the initial development stages of the overall analysis code discussed herein, a detailed study of a number of available calculation techniques was carried out. It was found that the integral techniques considered were much faster than the finite-difference routines. Therefore, for the purposes of the overall analysis scheme, it was felt that any small accuracy gain which may be achieved via a finite-difference code, would be more than offset by the appreciable increase in computational time. An integral boundary layer technique was therefore adopted to provide the required viscous corrections within the viscid-inviscid interaction scheme.

The method chosen for both the laminar and turbulent boundary layer calculations was a two-parameter energy integral technique, with the equations cast in the form of Le Foll (Ref.32), as given by Assassa and

Papailiou (Ref. 33). This formulation produces no numerical difficulties as skin friction vanishes in the region of separation and so provides accurate predictions of the phenomenon. This is an important consideration when for low Reynolds numbers, both laminar and turbulent separation may be present simultaneously at different locations along the chord.

3.2 Detailed Procedure Adopted

The procedure requires the simultaneous solution of the momentum and energy integral equations, as given below (eqn's 3.1 & 3.2)⁺, over each calculative step.

$$dq = C_1 dL - \frac{C_1 M}{1 + 2C_1 M} dX \quad (3.1)$$

$$d\phi = \frac{e^X dX}{(1 + 2C_1 M) CD e^{2C_1 L}} \quad (3.2)$$

The following definitions apply

$$C_1 M = \frac{1}{H - 1} \left[1 - \frac{He C_f}{2 CD} \right] \quad (3.3)$$

$$X = \ln \left[\frac{\epsilon u_e}{\nu} e^{2C_1 L} \right] \quad (3.4)$$

$$dL = \frac{1}{H-1} \frac{dHe}{He} \quad (3.5)$$

$$\phi = \int_0^s \frac{u_e}{\nu} ds \quad (3.6)$$

⁺ The derivation of these equations is given in Appendix 5.

$$q = \ln \frac{u_e}{U_0} \quad (3.7)$$

When equations 3.1 & 3.2 are solved in the direct mode, the values of $d\phi$ and dq , corresponding to the increment in stepwise length Reynolds number and the velocity gradient respectively, are necessary inputs. The subsequent boundary layer development is then given by the change in Reynolds number based on the energy thickness, and the increment in the value of profile form parameter L . It should be noted that, although only the direct formulation is considered here, these equations also lend themselves to solution in the inverse mode, where, for a given series of properties $L(X)$, it is possible to find $q(\phi)$. In the direct mode, the functions L and X are well behaved towards separation and the parameters H and C_f , which vary very rapidly, do not appear explicitly. Closure of this system of equations requires the development of functions $M(L,X)$ and $CD(L,X)$. The development of these functions, which are different for the laminar and turbulent calculations is discussed below.

3.3 Laminar Boundary Layer

Initially the laminar boundary layer calculation was by the method due to Head (1952) (Ref. 34). This procedure was specifically developed for use with a slide rule, and whilst apparently very accurate, was, when configured for computer use, slow and required a large number of steps per calculation. The accuracy of this method came mainly from it's doubly infinite velocity profile family which was subsequently used to develop the present technique. This new algorithm, while retaining the accuracy of the original, is computationally more efficient and more appropriate to the treatment of separation and thus, separation bubbles.

During development of the overall prediction scheme, a number of approximate techniques were studied with a view to their implementation in the aerofoil performance code. The criteria governing selection were the accurate prediction of separation and related boundary layer growth. It was felt that the point of separation would have to be predicted well, firstly to allow accurate calculation of gross laminar separation effects, and secondly, to give the precise location of upper surface laminar separation bubbles. Curle (Ref. 35) indicated that the accuracy with which a method predicts separation is closely linked to its ability to model boundary layer growth correctly. The importance of which, at low Reynolds number, is manifest in the calculated transition location since this location generally depends on some momentum thickness Reynolds number correlation.

It was apparent that, of the methods considered, the technique of Head gave the best prediction of separation when compared to a number of cases.

In Table 1 three methods are compared for a variety of series and exact solutions, and it may be seen that the method of Head compares very favourably. It should be noted that, although the series solutions of Gortler were used for the purpose of comparison, it is accepted that these solutions may systematically over-predict the distance to separation by some small amount (Ref. 36). The above result was, however, confirmed by Curle (Ref. 35) who also indicated that the associated boundary layer growth due to Head's method was, as expected, more accurately predicted than via the other methods. The prediction of separation to within two percent was felt to be acceptable for the application considered herein. The apparent inaccuracy of the other methods rendered them less suitable for inclusion in the predictive scheme and so, the method of Head was adopted.

Results obtained via this method for gross laminar separation were satisfactory, but the method appeared to be computationally cumbersome. To understand the reasons for this, it is necessary to examine the method itself.

3.3.1. Method of Head

This method was developed by Head in 1952 (Ref. 34) as an aid to proposed flight experiments with distributed suction. It is based on the energy and momentum integral equations and utilises a doubly-infinite velocity profile family, along with the first compatibility condition at the surface to effect closure. The equations are given in the form

$$t^{*'} = \frac{2}{\bar{U}} \{ \ell - \Gamma (H + 2) \} \quad (3.8)$$

$$He' = \frac{1}{\bar{U} t^*} [2D^* - He \{ \ell - \Gamma (H - 1) \}] \quad (3.9)$$

where

$$t^* = \left[\frac{\theta}{c} \right]^2 \left[\frac{U_0 c}{v} \right] \quad (3.10)$$

$$\Gamma = \left[\frac{\theta^2}{v} \right] \left[\frac{du_e}{ds} \right] = t^* \bar{U}' \quad (3.11)$$

$$D^* = \int_0^{\delta/\theta} \left[\frac{\theta^2}{u_e} \right]^2 \left[\frac{\partial u}{\partial y} \right]^2 d \left[\frac{y}{\theta} \right] \quad (3.12)$$

$$\ell = \frac{\theta}{u_e} \left[\frac{\partial u}{\partial y} \right]_0 \quad (3.13)$$

$$m = \frac{\theta^2}{u_e} \left[\frac{\partial^2 u}{\partial y^2} \right] = -\Gamma \quad (3.14)$$

During calculation, the first two equations are used to provide increments in momentum thickness and energy form parameter over each step. Once the first compatibility condition (eqn. 3.14) is satisfied, use can be made of the profile parameter contour charts given in Figs. 3.1a,b,c to determine the new profile parameter values. Computationally, the use of such charts was achieved by interpolation. This process, coupled with the need to input a large data file, was a contributory factor to the inefficiency of the computer code. One further drawback arose from the stability of the calculation for certain conditions.

Head (Ref. 34) pointed out that, when the boundary layer was thin, successive values of He' tended to oscillate wildly. The solution to this problem was a reduction in station increment size under such conditions, which subsequently increased the calculation time. At separation the calculation became indeterminate and thus continuation through the point of separation would have been impossible in the direct mode.

Although the method was computationally slow, the accuracy of prediction obtained was felt to be very satisfactory. The doubly-infinite velocity profile family used to provide the parameter charts, and the inclusion of upstream influence via the energy equation were the main reasons for the success of the method. The range provided by these profiles meant that, even in regions of rapid pressure gradient change, the calculation would approximate closely to reality. It appeared that, if a new method could be developed which was well behaved at separation, still retained the accuracy given by the velocity profile family and was computationally more efficient, it would be desirable for the overall predictive scheme.

3.3.2. Development of a New Laminar Boundary Layer Calculation Technique

The boundary layer calculation method of Le Foll (Ref. 32) provided the basis for the new method. To effect closure of the system of equations (3.1-3.7) it was necessary to develop relations between the four boundary layer parameters H , He , D^* and C_f . Graphs of H v's He and He v's $2D^*$ were plotted from the velocity profile parameter charts, and polynomials fitted through the data points (Figs. 3.2 and 3.3). It was found that the average percentage error between the points and the polynomial fit was

3.1% for the H v's He relation and 1.1% for the He v's $2D^*$ relation. The data were then filtered to reduce the influence of profiles indicative of suction effects and the resulting accuracy of the two fits was increased to an acceptable error level of less than one percent thus allowing the polynomials to be implemented into the calculation.

Integration of the H v's He curve permitted the relationship between L, the ordinate of Le Foll's plane, and He to be defined. This relation was initially represented by a polynomial of degree six and is shown in Fig. 3.4. The value of the dissipation coefficient CD was forthcoming from the He v's $2D^*$ since

$$CD = \frac{\nu}{u_e \theta} 2D^* \quad (3.15)$$

Having established these relations, only skin friction remained to be included. Initially the value of l from Head's profile family was correlated, in turn, against H, He, and D^* . It was found that, although calculation was possible by any one of these relations, the results obtained were not of the quality of the original method. An interpolation procedure was therefore adopted using the values of m, l and $2D^*$ from the tabulated data to find the skin friction. Whilst the inclusion of an interpolation scheme effectively slowed the calculation, it remained significantly faster than the original method due to the reduction in input data and the inclusion of the polynomial relations. The new technique also appeared to be less sensitive to calculation stepsize allowing a significant reduction in the number of steps per calculation. Finally, the method, as indicated by the turbulent case, was well behaved in the vicinity of separation, thus providing the basis for the subsequent

extension to separated flow.

3.3.3 Comparison of New Technique with Head's Method

The new technique, once established, was compared with the original method due to Head over a number of the exact/series solutions. The results of the separation prediction for both methods are given in Table 2. The percentage difference in the distance to separation, between the new method and the exact/series solutions, was found to be 1.86% compared with 1.7% for Head's method. This result gave a significant indication of the retained accuracy of the new technique.

Comparison of boundary layer growth and parameter development was made for all the test cases and an illustration of the quality of agreement obtained is given in Fig. 3.5 where results for two of the velocity distributions are presented. In both cases, growth prediction is similar for the two schemes although some disparity is evident between the predicted form parameters, especially in the case where the calculation begins from a stagnation point. The difference in the form parameter prediction is related to the variance between the original tabulated parameter data and the developed polynomial relations which are used in the present method. It was felt that further filtering of the parameter data may have produced a better correlation but the results obtained were considered to be satisfactory for aerofoil application since, in all cases, the percentage disagreement was small.

The two methods were then compared over a number of aerofoil velocity

distributions. Initially a very crude linearly interpolated representation of velocity gradient was used without any smoothing. An example of the prediction obtained is given in Fig. 3.6 for the GA(W)-1 aerofoil at six degrees incidence. Whilst the method of Head gave a relatively smooth prediction, that due to the new technique exhibited several discontinuities. Closer examination of this result indicated that, the steplike nature of the calculation output was related to the unsmoothed representation of the velocity gradient, and that the apparent discontinuities coincided with the inviscid calculation panel corner points as shown in Fig. 3.7. The influence of pressure gradient on the method was isolated to the behaviour of the parameter m and the subsequent effect which it had on the skin friction interpolation.

Since the inclusion of this parameter was essential to the method, it was preferred to modify the velocity gradient input. The use of a spline fit was investigated and, although a smooth distribution was obtained (Fig. 3.8), the approach proved to be problematic when considered for the overall predictive scheme. A three point Lagrange interpolation scheme was therefore used to provide the pressure gradient input to the calculation. Although the distribution obtained (Fig. 3.9) was not completely smooth, it was a considerable improvement on the original. A series of tests were conducted to assess the effect on accuracy of spline fitting compared with the simpler Lagrange interpolation. It was found that the difference in predicted transition and separation locations was generally very small, and the effect on the full aerofoil calculation negligible.

Inclusion of the new technique into the overall procedure produced a

saving of some five percent in computation time and, more importantly, provided a laminar boundary layer calculation technique with possibilities of extension to separated flow problems such as separation bubbles. The nature of this calculation will be discussed in detail in chapter five.

3.4 Turbulent Boundary Layer Calculation

The method of Le Foll (Ref. 32), as given by Assassa and Papailiou (Ref. 33), was used to calculate the development of the turbulent boundary layer. This method was adopted principally for its ability to calculate separation accurately and to deal with small regions of separated flow. The former being considered important to the accuracy of the overall performance calculation, and the latter, to the extension of the method to cope with laminar separation bubbles. The system of equations 3.1 - 3.7 require, as stated previously for the laminar case, the development of a number of relations to effect closure. The method of Assassa and Papailiou utilises the velocity profile family of Coles (Ref. 37) in the more general form of Kuhn and Nielsen (Ref. 38) to provide both the skin friction and the boundary layer velocity distribution terms.

This profile can be expressed in the form

$$\frac{u_e}{U_\tau} = \left[2.5 \ln(1 + Y^+) + 5.1 - (3.39 Y^+ + 5.1)e^{-0.37Y^+} \right] + \frac{\pi}{0.4} \left[1 - \cos \left[\pi \frac{y}{\delta} \right] \right] \quad (3.16)$$

and by evaluating the above equation at the edge of the boundary layer, the skin friction coefficient can be found. In the above equation, the parameter U_τ is the friction velocity expressed, to accommodate separated flows, in the modified form

$$U_\tau = \left[\frac{\tau_w}{|\tau_w|} \right] \left[\frac{|\tau_w|}{\rho} \right]^{1/2} \quad (3.17)$$

In equation (3.16) the additional unit in the logarithmic term and the

inclusion of the extra exponential terms are used to provide a smooth transition between the turbulent flow and the wall, through a laminar sublayer. At high Reynolds numbers these terms are generally insignificant except in the wall region, but, with reduced Reynolds number, become more dominant, and eventually distort the profile. To overcome this problem, the exponential terms were scaled in accordance with the reduction in Reynolds number and thus a more realistic profile representation was obtained for both attached and separated flow cases. This treatment of the profile will be discussed in more detail in Chapter 5.

With the profile shape defined in the above manner, it was possible to develop a relation between H and He and thus, by integration of this function, a correlation between H and L (Figs. 3.10 and 3.11). The empirical relation given by Assa'ssa and Papailiou was employed to provide the value of the dissipation coefficient

$$C_D = \left[\frac{H - 1}{H} \pi_1 He + He \right] \frac{C_f}{2} \quad (3.18)$$

and so from equation (3.3) the value of M could be obtained.

Implicit in the above equation is the equilibrium parameter π_1 which is related, within the algorithm, to the Rotta-Clauser form factor G by the relation given by Nash (Ref. 33), which is expressed in the form

$$\pi_1 = 0.026874 (G^2 + 2.8G - 64.47) \quad (3.19)$$

Although this relation is only valid for equilibrium flows, tests indicate

(Ref. 34) that the accuracy of the method for non-equilibrium cases is acceptable.

In order to test the accuracy of the algorithm, once established, the calculations of Assassa and Papailiou, for the test cases of Chu and Young (Ref. 39), were duplicated (Fig. 3.12) and found to agree with the original. It should be noted, that in both these cases, separation would not have been predicted unless the influence of the fluctuation terms were included. In this method a first attempt at the inclusion of these terms was made via the value of C_1 where

$$C_1 = \frac{H - 1}{H^* - 1} = 0.85 \quad (3.20)$$

The value of C_1 is set to unity in the laminar case, thus effectively neglecting the second order terms.

The computer algorithm was tested over a number of Stanford Conference (Ref. 40) cases and was found to perform well in the majority of these. Two example comparisons are given in Fig. 3.13 and Fig. 3.14 for Weighardt's flat plate flow, and for the Bradshaw and Ferriss relaxing flow. The prediction obtained for both flows compares well with experimental data except in the prediction of skin friction for the relaxing flow. Other, more commonly used, boundary layer calculation techniques provide no better predictive capability, for this particular case (Ref. 40), and are generally not as well behaved in the vicinity of separation. It was felt, therefore, that on the basis of these and other results, the method was satisfactory for inclusion in the overall scheme.

3.5 Transition

Within the present analysis scheme, there are four main transition options available. These are

- 1) Fixed transition on the upper surface
- 2) Calculated natural transition
- 3) Transition just prior to laminar separation
- 4) Transition within a laminar separation bubble

Of these options, the first three are contained within the mainstream calculation and are straightforward in application. The fourth, however, is, at present, an interactive calculation requiring some knowledge of the program structure and output formulation. This fourth option is discussed in some detail in Chapter 5.

If transition is fixed, then the required input to the program is the chordal location. The laminar boundary layer calculation terminates at this specified point and provides the starting conditions for the subsequent turbulent calculation. At present, no modification of these starting conditions is allowed for, although it is likely that this option will be included as a subsequent enhancement.

Two different correlations are available to provide the calculated location of transition. The first, due to Michel (Ref. 41), assumes that the momentum thickness Reynolds number, at transition, is related to the surface length Reynolds number by the equation

$$R_{\theta} = 1.174 \left(1 + \frac{22400}{R_s} \right) R_s^{0.46} \quad (3.21)$$

The second method of calculating the location of transition is the e^9 method of Van Ingen (Ref. 42) and Smith and Gamberoni. This method, which is based on linear stability theory, assumes that when a small disturbance is introduced at a critical Reynolds number and is amplified by a factor e^9 , transition begins. The present calculation utilises the correlation given by Cebeci (Ref. 24) which was derived via the Faulkner-Skan equation

$$R_{\theta} = 14.9987 + 1.69602(R_s - 7256.37) |R_s - 7256.37|^{-0.56399} \quad (3.22)$$

Whilst transition from laminar to turbulent flow, at low Reynolds number, often occurs within a separated shear layer, the present analysis scheme boundary layer calculation routine is unable to model this phenomenon. If the boundary layer calculation does indicate laminar separation prior to natural transition, then the third option fixes transition to occur just prior to the separation point. For very small separation bubbles, it is likely (Ref. 17) that the growth of the boundary layer behind the separation bubble would be similar to that obtained by this simple approach.

DEVELOPMENT OF A LONG SEPARATION BUBBLE REATTACHMENT CRITERION

4.1 Introduction

The requirement for certain aerodynamic devices to operate with a low characteristic Reynolds number often results in severe performance degradation of the important lifting and control surfaces. For an aerofoil, the Reynolds number range $Rc < 1 \times 10^6$ is particularly critical due to the sensitivity of the flow to such parameters as noise, surface texture, vibration, geometric environment and freestream turbulence (Refs. 1 & 6). The problem is further compounded by the behaviour of the aerofoil boundary layer, particularly if laminar separation exists. The analytic assessment of the aerofoils performance is therefore a difficult, and often, approximate procedure. This chapter considers one aspect of this flow regime, namely, the prediction of the onset of long separation bubble formation from the unattached condition as the Reynolds number is increased.

Recent empirical data for the GU25-5(11)8 aerofoil (Ref. 29) highlights the effect of such a phenomenon. In the contour chart, presented in Fig. 4.1, it can be seen that, for an incidence of four degrees and an increasing Reynolds number, there is a tenfold increase in lift where the contours are closely spaced. This rapid change in lift coefficient is indicative of long separation bubble formation followed by

rapid contraction to a stable short bubble. This region, which is often referred to as the 'critical' region, may occur at different Reynolds numbers for different aerofoil sections and, generally, the magnitude of the associated change in lift can vary considerably and is difficult to determine analytically. Comparative tests on the above aerofoil, the GA(W)-1 aerofoil and the NACA 0015 section were recently conducted in the same facility (Ref. 43) to assess their low Reynolds number performance. It can be observed in Figs. 4.2 & 4.3 that the critical region for the GA(W)-1 aerofoil was only just reached, and was beyond the range of the facility for the NACA 0015 section. These particular examples give a good indication of the variation in critical region location to be expected between different aerofoil sections. The location of this region may be further affected by the disturbance environment of the test facility.

The explanation of this phenomenon follows from consideration of the upper surface boundary layer behaviour and, in particular, the nature of the laminar separation bubble once formed. Prior to the formation of this bubble, there exists laminar separation with no subsequent shear layer reattachment. Once, with increased Reynolds number, reattachment occurs forming a 'long bubble', it rapidly contracts with further small increases in Reynolds number. This progression continues until a short, stable laminar separation bubble is formed. With subsequent increases in Reynolds number, the short bubble may disappear if transition occurs prior to laminar boundary layer separation. An illustration of this process is provided in Figs. 4.4a & 4.4b where both boundary layer and pressure distribution behaviour are presented. The most noticeable feature of this figure is that, for the same angle of attack, there is a threefold change in the value of suction peak for a Reynolds number change of just

3.3×10^5 even when considerable turbulent separation was present at the higher Reynolds number.

It has been shown by several investigators (Refs. 1 & 18) that the pressure distribution associated with short laminar separation bubble formation is very similar to that which would occur as a result of 'standard' laminar-turbulent boundary layer flow. The preceding figure, however, highlights the quite different and more significant effect of the long bubble, where the suction peak collapse can be dramatic. This has rendered the prediction of all but the short bubble to an uncertain accuracy and, more generally, to the empirical domain. The identification of the long bubble formation region would, however, appear desirable for any low Reynolds number aerofoil analysis scheme and would undoubtedly be of practical interest to the design engineer. If the performance of an aerofoil could be predicted on either side of the region, then a technique which identified the region's lower limit and the rate of bubble contraction, would give an indication as to whether the aerofoil could operate through it's critical region without causing severe performance degradation. The ability of a flight vehicle to operate through, or on the limit of, its critical region could thus be assessed. It is proposed herein that a criterion based on the method of Horton (Ref. 16) can identify the lower Reynolds number limit of long bubble formation and indicate the subsequent collapse to the short form.

4.1.1 General Description of the Reattachment Problem

The occurrence of separated shear layer reattachment, due to increasing Reynolds number, is difficult to determine by experiment. Flow visualization on a large scale model of the GU25-5(11)8 aerofoil (Ref. 44) indicated that, prior to well defined long bubble formation, there existed a fluctuating state between fully separated flow and shear layer reattachment. Although it is likely that the extent of this fluctuating state is dependant on the turbulence environment of the test, it may also be true that this phenomenon represents the analytical near trailing edge reattachment case just prior to rapid bubble contraction. It was the modelling of the related reattachment Reynolds number which was the considered problem.

Horton (Ref. 16) developed a method for the prediction of the growth and bursting of short laminar separation bubbles which is adequate while the perturbed velocity distribution closely resembles the inviscid solution, since the latter is used in the reattachment criterion. For 'classical' short bubbles, this similarity initially exists although, as growth continues towards 'bursting', discrepancies in the two distributions become more marked and the predictive effectiveness deteriorates. As previously discussed, flows exhibiting long separation bubbles differ significantly from the normal laminar-turbulent boundary layer cases, and as such are not amenable to analysis by this method. It was felt, however, that if the equations derived by Horton provided an adequate representation of the behaviour of the free shear layer of a long bubble, then a solution of the long bubble problem may be obtained by the simple inclusion of an alternative reattachment criterion.

The progression through the critical region is such that, with increasing separation bubble length there is generally an associated collapse of the pressure distribution suction peak. The limiting value of this collapse occurs when reattachment just fails to take place. Thus, with enlarging bubble size, the pressure distribution tends towards the laminar separation configuration. It appeared possible, therefore, that a reattachment criterion based on the separated laminar flow pressure distribution may provide a plausible indicator of long bubble formation. Before discussing the proposed reattachment criterion in detail, it is pertinent to consider the treatment of the free shear layer.

4.2 Separated Shear Layer

After laminar separation from the aerofoil surface, a laminar shear layer exists for a short distance, the length of which depends on such parameters as Reynolds number and freestream turbulence, before it undergoes transition to the turbulent state. The shear layer thickens rapidly, after transition, by increased entrainment of the the surrounding fluid. If this entrainment rate is sufficiently large, then shear layer reattachment will occur, so forming a laminar separation bubble.

For the purposes of analysis it is convenient to deal with the free shear layer as two distinct regions, i.e. before and after transition.

4.2.1 Laminar Shear Layer

The original correlation utilised by Horton (Ref. 16) to relate the length of the laminar shear layer (non-dimensionalised by the momentum thickness at separation) to $R_{\theta_{sep}}$ is given in equation 4.1 below.

$$\frac{l_t}{\theta_{sep}} = \frac{4 \times 10^4}{R_{\theta_{sep}}} \quad (4.1)$$

The free laminar shear layer is an inherently unstable phenomenon and, as such, is very sensitive to the freestream disturbance environment in which it exists. The above correlation of Horton, when compared to a number of experimental investigations (Fig. 4.5), shows poor agreement with the majority of data points obtained. Although extraneous flow effects have not, in general, been empirically modelled, attempts have been made to

assess the influence of freestream turbulence (Ref. 6). Roberts (Ref. 30) proposed an improved correlation of the form

$$\frac{l_t}{\theta_{sep}} = \frac{K \text{Log}_{10} [\text{coth}(\text{TF} \times 10)]}{R\theta_{sep}} \quad (4.2)$$

where TF is the Turbulence Factor and K is a constant taking the value 2.5×10^4 . Turbulence intensity may be substituted for Turbulence Factor since, during an experiment, it is common to measure only the turbulence intensity and since, generally, the macroscale length of flow turbulence has a very small effect on the value of the Turbulence Factor.

If the relation of equation 4.2 is plotted against the empirical data (Fig. 4.6) by adjusting the data via the turbulence correction, it can be observed that, although the scatter is still quite significant, the general agreement has been noticeably improved. In the developed technique, the correlation of Roberts was used, but with the value of K adjusted to 3×10^4 . It was felt that this value gave a slightly better fit to the available empirical data.

It should be noted that, in the above figure, the data of Gault (Ref. 14) represents leading edge separation bubbles only, as he himself considered some of his mid-chord data to be suspect. The results produced by Gaster (Ref. 14) have been adjusted upward slightly since Gaster measured the length of the bubble dead air region and not the laminar shear layer. Gaster indicated that the dead air region was about forty to fifty percent of the total bubble length, whereas, the laminar shear layer would be expected to account for up to eighty percent of the bubble.

The reversed flow velocities within the laminar portion of a separation bubble are relatively small. It is therefore assumed, in Horton's method, that the associated skin friction is negligible and thus from the momentum equation $d\theta/dx = 0$. The momentum thickness at transition is, therefore, known and is equivalent to the momentum thickness at the point of laminar separation.

4.2.2 Turbulent Shear Layer

The criterion developed by Horton to indicate separated shear layer reattachment is founded on the assumption of a universal velocity profile at the point of reattachment. Although this may be an accurate assumption for short laminar separation bubbles, it is unlikely to be representative of the conditions of long bubble reattachment where the boundary layer would possibly be in a wake-like state (Ref. 44) with reattachment occurring as an intermittent phenomenon. It was felt, however, that once reattachment had been established, the reattachment profile would tend towards that given by Horton, with increasing Reynolds number. This assumption, if correct, would render the turbulent shear layer analysis of Horton valid for the present purpose. The premise of a universal velocity profile, coupled with the assumption of constant eddy viscosity permits Truckenbrodt's (Ref. 16) shape parameter equation to be reduced to the form

$$\Lambda_R = \left[\frac{\theta}{u_e} \frac{du_e}{ds} \right]_R = -0.0059 \quad (4.3)$$

The value of this pressure gradient parameter was adjusted to account for the increased dissipation in a reattaching boundary layer, by adopting an

experimental mean value of

$$\Lambda_R = \left[\frac{\theta}{u_e} \frac{du_e}{ds} \right]_R = -0.0082 \quad (4.4)$$

By assuming a linear drop of external velocity over the turbulent part of the separation bubble, the above pressure parameter reattachment criterion combined with the energy integral equation yields

$$\bar{u}_{eR}^4 = \frac{\frac{CD_m}{4He} + \frac{(1 - \bar{u}_{eR})}{l_b - l_t}}{\frac{CD_m}{4He} - \Lambda_R} \theta_{sep} \quad (4.5)$$

With the momentum thickness at the point of laminar separation known and the energy form parameter following from the mean reattachment profile, only the value of CD_m was required for solution. This value was taken to be $CD_m = 0.0182$, as used by Horton. A locus of possible reattachment points could therefore be generated by the above equation. Reattachment was deemed to occur if this locus became tangential to the reattachment line velocity distribution. A detailed derivation of Horton's method is contained in Appendix 6.

4.3 Reattachment Criterion

To develop a long bubble reattachment line it was first necessary to establish the governing parameters. The laminar separation pressure distribution prior to bubble formation may, as previously indicated, influence the point at which reattachment takes place. A parabolic pressure coefficient reattachment line based on this distribution was therefore investigated. Such a distribution was chosen, since three defining conditions were considered to be of relevance. Of these three conditions, one was supplied by the inviscid flow pressure distribution, and the remaining two, by the separated laminar flow pressure distribution. The reattachment curve developed is shown in Fig. 4.7.

The first governing parameter was provided by the value pressure coefficient at the point of laminar separation. It was assumed that this value of pressure coefficient would exist just prior to shear layer reattachment and so the free shear layer would initially have this pressure as its starting value. Similarly, any reattachment line must also begin from this point. The reattachment line pressure gradient through separation was assumed continuous with respect to the 'attached' portion of the separated flow pressure distribution. This followed from consideration of the limiting case where shear layer reattachment occurs at an infinitely short distance behind separation. The resultant pressure distribution would closely resemble the attached flow case and, therefore, exhibit virtual continuity of pressure gradient through the separation and reattachment points.

The final boundary condition required to define the reattachment line

was derived from the inviscid flow pressure distribution. Once separation is initiated on an aerofoil, the value of trailing edge pressure coefficient steadily reduces from the limiting fully attached flow value which can be predicted with some accuracy via an appropriate inviscid calculation. In an extreme case, bubble reattachment may occur at the trailing edge and so may be considered to instantaneously achieve a value of pressure coefficient close to that of the inviscid solution. For this reason, the trailing edge pressure coefficient for the inviscid flow case was taken as the last boundary condition.

The behaviour of the developed reattachment line with respect to the locus of possible reattachment points is illustrated in Fig. 4.8. Intersection or tangentiality of these two curves would indicate separated shear layer reattachment.

4.4 Results of the Reattachment Method for the GU25-5(11)8 Aerofoil

As previously demonstrated, the GU25-5(11)8 aerofoil exhibited a well defined critical region and, as such, provided an ideal test case for the developed method. To apply the reattachment criterion effectively, it was necessary to run the aerofoil analysis procedure over a number of closely spaced Reynolds numbers for each angle of attack. This was carried out for the above aerofoil and the appropriate reattachment Reynolds number established for each incidence. Pressure distribution and flow visualization data were available for this aerofoil section, thus allowing Fig. 4.9 to be generated. This figure is an idealised representation of Fig. 4.1 with the empirical lines of shear layer reattachment and stable short bubble formation highlighted. Comparison of the predicted results with the idealised shear layer reattachment line shows considerable agreement although the positions of the experimentally obtained reattachment cases are difficult to establish exactly, and so, the subjective location of the idealised line is prone to some small degree of uncertainty.

Generally, it can be observed that at lower angles of attack the calculated reattachment Reynolds numbers are more consistent with the empirical line, than at higher angles. This result may have been related to the reduction in appropriateness of the quasi-linear approximation to the continuous vortex sheet, within the panel method, as separation moved closer to the leading edge. The high curvature associated with the leading edge should normally be represented by a large number of panels, whereas, in this case only forty seven panels described the entire profile. It was felt that the calculation may have been improved if a

larger number of coordinates had been available for use. A further complication arose from the fact, as stated in Chapter 2, that the numerical difficulties encountered when the wake model ran close to the aerofoil surface resulted in a forced shifting of the separation point. This became more critical as the separation point moved in front of the maximum thickness and the wake departure angle from the aerofoil surface became more acute. The quality of definition of the pressure gradient at the point of laminar separation may also have had some influence since the pressure gradient in the proximity of separation was strongly dependant on the vortex panel distribution. Resolution may have been lost if the number or distribution of the vortex panels was unsuitable, although, since the reattachment line started and finished at well defined points, it was felt that any such effect may not have been significant.

By providing the separation and reattachment points of the shear layer, an indication of the bubble size could be obtained from the technique. The flow visualization data for the GU25-5(11)8 aerofoil (Ref. 45) was used to obtain empirical bubble lengths for certain cases. Results were obtained from the reattachment criterion for these cases and comparison made with this empirical data. It became clear, from this comparison, that the length of the bubble was predicted with some accuracy when the bubble was long; typically more than thirty percent chord. Such accuracy was not, however, evident for shorter bubbles, after significant contraction had taken place, since the assumptions on which the method was based would lose validity. A general indication was, nonetheless, given for the rate of bubble contraction to the 'classical' short form.

4.5 General Application of the Criterion

The general applicability of the method remains, as yet, unproven. The final boundary condition used to define the criterion reattachment line was somewhat speculative. The inviscid flow trailing edge pressure coefficient is an upper limit and as such is unlikely ever to be reached in practice. An added complication arises from the fact that this value was found to be influenced by the upper and lower surface panel distributions near the trailing edge. As a consequence, a certain degree of variance was introduced into the calculation. It was felt, however, that this variance was unlikely to have a significant effect on the overall result due to the stabilizing effect of the short wake calculation, discussed in chapter two, and the fact that reattachment generally occurred away from the trailing edge.

The representation of the bubble pressure distribution by Horton's method is only valid when a short separation bubble is being considered. It is therefore unrealistic to extend the method to the prediction of the pressure distribution due to a long separation bubble based on the present approach. Application of it should thus be limited to shear layer behavioural prediction. This limitation relegates the present technique to that of a bubble formation indicator. It is clear that a different approach would be required if long bubble effects were to be calculated by some viscid-inviscid interaction scheme although, if the gross laminar separation and steady short bubble performance were both known, an estimate of the long bubble effect could be made by simple interpolation through the indicated critical region.

The deterioration of the prediction for the GU25-5(11)8 aerofoil, as the separation point moved forward indicated that, for the reasons given above, the method may be more applicable to sections exhibiting mid-chord separation bubbles rather than leading edge ones.

The results obtained by the reattachment criterion are strongly dependant on the quality of prediction made by the aerofoil analysis procedure of which it is part. Since, at present, only one aerofoil section has been examined in detail, the effectiveness of, not only the developed reattachment criterion, but also the laminar Wake Factor increment correlation remain unproven. Although the relative scarcity of low Reynolds number laminar separation data poses a problem, further substantiation by means of comparison with experimentally obtained data from other aerofoil sections, and other test facilities, is required.

EXTENSION OF THE BOUNDARY LAYER CALCULATION TO SEPARATED FLOW

5.1 Introduction

At low Reynolds numbers, it is possible for laminar separation to precede transition. If this occurs, the free shear layer normally undergoes transition shortly after separation and the subsequent entrainment process is usually sufficient for shear layer reattachment to take place, so forming a separation bubble. Provided the bubble is small, the effect which it has on the aerofoil pressure distribution is small and is characterised by a small perturbation near the leading edge with an associated slight reduction in the suction peak. It is of significance, however, that with reduced Reynolds number the onset of stall may be influenced by the presence of such a bubble, although this effect is, at present, difficult to quantify. This phenomenon is likely to arise from the behaviour of the turbulent boundary layer formed behind the separation bubble since the stability of this boundary layer is fundamental to the subsequent aerofoil separation characteristics. A reattaching boundary layer of this type may exist in a non-equilibrium state for some distance beyond the point of reattachment and may also be significantly thicker than that which would occur as a result of natural transition (Ref. 17). The sluggish nature of this thickened boundary layer may induce trailing edge separation earlier than would otherwise occur. This effect would be more significant at high angles of attack where the relatively short

turbulent boundary layer would be prone to the influence of the separation bubble over most or all of its length. A development of the aerofoil analysis scheme to allow the assessment of boundary layer growth behind a separation bubble and to investigate the effect, on the separation characteristic, of such growth was therefore initiated.

Extension of the boundary layer calculation through the point of laminar separation was hampered by the existence of the well documented (Ref. 46) singularity which results in a breakdown of the direct boundary layer calculation as separation is approached. Recent investigations (Refs 17 & 47) have preferred to calculate through the point of laminar separation by solving the boundary layer equations in the inverse mode. When a solution is obtained in this manner, the velocity distribution is the calculation output with some parameter such as displacement thickness taken as an initial specified input. This approach exhibits no singular behaviour around the separation point and, as such, a smooth progression from attached to separated flow is obtained. For the calculation of separation bubble effects, the inverse formulation requires a fully viscid-inviscid interaction type approach with, generally, a Cauchy integral representation of the perturbed inviscid flow (Ref. 17). If it were possible to calculate separation bubble effects directly, then it would be possible to analyse empirical data more thoroughly via the pressure distribution obtained in a test. This, in turn, would, for example, allow the assessment of the effect of a boundary layer trip, as opposed to the separation bubble, to be made more accurately without resorting to further experiment.

The recent direct turbulent boundary layer calculation technique of

Assassa and Papailiou (Ref. 33) has been shown to behave well in the vicinity of separation and has been used successfully to calculate small regions of separated flow. The good performance of this method around the separation region was principally due to the manner in which the momentum and energy integral equations were formulated, with the chosen boundary layer variables being finite and well behaved near separation. The ability of this method to predict a reattaching boundary layer (Ref. 33), indicated its suitability for application to the turbulent portion of a separation bubble. Calculation of the laminar portion of the shear layer still posed a significant problem if the direct approach were to be employed.

The previously developed direct laminar boundary layer calculation technique, presented in chapter three, was well behaved as separation was approached. It was therefore felt that an investigation into the possible extension of the method through the point of laminar separation was warranted by the success of the above turbulent method.

5.2 Extension of the Laminar Boundary Layer Calculation

The laminar boundary layer calculation technique of chapter three relied on the velocity profile parameter data of Head (Ref. 34) to provide function relationships through which calculation closure could be achieved. Unfortunately, the velocity profile family only contained profiles indicative of attached flow. It was therefore necessary to extend the range of profiles in order that the required function relationships could be developed for separated flow.

5.2.1 Velocity Profile Development

To retain consistency between the profiles developed by Head (Ref. 34) and those to be developed for the separated flow calculation, the same basic approach was employed. In it, it was assumed that the velocity distribution within the boundary layer could be represented by the equation

$$\frac{u}{u_e} = f(\eta) = f_1(\eta) + cf_2(\eta) + df_3(\eta) \quad (5.1)$$

where $\eta = y/\delta$, $f_1(\eta)$ is the Blasius profile ($f_1''(0) = 0$), $f_2''(0) = f_3'(0) = 0$ and c and d are constants used to determine the profile shape. Formulation of the velocity profile in this form permitted the Blasius profile to be modified by varying amounts of the functions f_2 and f_3 to produce a range of velocity profiles. The functions f_2 and f_3 were determined in such a way that they satisfied two known profiles other than Blasius for each considered flow state. In the attached flow case, Head derived separation functions from two profiles given by Thwaites (Ref. 48), and high skin friction functions from the asymptotic suction

profile and a hypothetical profile having the same value of $1/U (dU/dn)_0$ but with $1/U (\partial^2 u / \partial n^2)_0 = 0$. Once, for the considered condition, the two profiles were known, it was possible to express them in the form

$$\frac{u}{u_e} = F(n) \quad (5.2)$$

$$\frac{u}{u_e} = G(n) \quad (5.3)$$

For each of these two profiles it was necessary to determine two matching approximate profiles such that

$$\frac{u}{u_e} = f_1 + c_1 f_2 + d_1 f_3 \quad (5.4)$$

$$\frac{u}{u_e} = f_1 + c_2 f_2 + d_2 f_3 \quad (5.5)$$

It is clear from the above equations and the stated boundary conditions that, if the approximate profiles were to satisfy the given profiles at the origin, then

$$F'(0) = f_1'(0) + c_1 f_2'(0) \quad (5.6)$$

$$F''(0) = d_1 f_3''(0) \quad (5.7)$$

$$G'(0) = f_1'(0) + c_2 f_2'(0) \quad (5.8)$$

$$G''(0) = d_2 f_3''(0) \quad (5.9)$$

Further, if the constants c and d were assigned arbitrary values, then the

system of equations to be solved contained only two unknowns; i.e. f_2 and f_3 , and

$$-F(n) = f_1(n) + c_1 f_2(n) + d_1 f_3(n) \quad (5.10)$$

$$G(n) = f_1(n) + c_2 f_2(n) + d_2 f_3(n) \quad (5.11)$$

These equations could thus be solved for numerous values of n , thereby providing the values of f_2 and f_3 through the velocity profile.

To develop the attached flow profiles, Head (Ref. 34) assigned the value of unity to c and d for the asymptotic suction profile and was able to determine the values of these constants corresponding to the separation profiles by specifying

$$[f_2'(0)]_1 = [f_2'(0)]_2 \quad (5.12)$$

$$[f_3''(0)]_1 = [f_3''(0)]_2 \quad (5.13)$$

where the subscript $_1$ refers to the separation profiles and $_2$ to the profiles with high skin friction. In this way, Head established that $c = -0.493$ for the two separation profiles, thus allowing the two sets of functions f_2 and f_3 to be developed.

When considering the problem of separated flow, it was necessary to have two separated flow profiles to develop the required functions and to thus extend the velocity profile family. Empirical data for separated laminar flows was not readily available and, until recently, prone to

severe measurement errors.

The hypothetical separated flow profiles of Stewartson (Ref. 49), derived from solutions of the Faulkner Skan equation, provided ideal examples for the present purpose since the profiles were well defined and their derivatives easily obtainable. Two of these profiles were therefore used to develop the required functions. The specific profiles were those characterised by $\beta = -0.025$ and $\beta = -0.05$, both of which are presented in Fig. 5.1. The necessity for the pair of profiles to have the same value of $1/u_e (\partial u/\partial n)_0$ presented a problem since, for the above mentioned profiles, this was not the case. As a result, two different values of the constant c were obtained for the separated flow profiles. By averaging these values, the constant c was calculated to be $c = -0.8226$. The error associated with this averaging process was found to be less than two percent. The method used to obtain this value of c was completely consistent with that of Head and the original constraints were employed, such that

$$[f_2'(0)]_1 = [f_2'(0)]_2 = [f_2'(0)]_3 \quad (5.14)$$

$$[f_3''(0)]_1 = [f_3''(0)]_2 = [f_3''(0)]_3 \quad (5.15)$$

where the subscript $_3$ refers to the Stewartson profiles. The percentage error involved with the adoption of a single c value for the Stewartson profiles was felt to be acceptable and the functions f_2 and f_3 were therefore obtained in the manner described above. These functions along with those developed by Head, for the high skin friction and separation profiles, are presented in Fig. 5.2. The development of these functions

from the high skin friction case, through separation, into the separated flow region appears, from the figure, to follow a progression with the most striking change occurring after separation as would be expected (Ref. 46).

Having established these functions, it was possible to obtain intermediate profiles by interpolation between the different function values. Head (Ref. 34) assumed a linear interpolation between the high skin friction values and the separation profile values such that for an intermediate value c_{in} and for $n = n_1$, the value of the function f_2 could be obtained from

$$f_2 = [f_2(n_1)]_1 - \left[[f_2(n_1)]_1 - [f_2(n_1)]_2 \right] \frac{0.493 + c_{in}}{1.493} \quad (5.16)$$

A similar scheme was used to obtain intermediate values of f_3 . This process of interpolation was then repeated for each value of n until a full profile could be defined.

In the present method, it was desired to achieve continuity with the attached flow profiles of Head. The marked change in function values, between the separation profiles and the Stewartson profiles, indicated that, generally, simple extrapolation of the above technique would not allow the required separated flow function values to be achieved. An interpolated curve was therefore used, between the separation profile function values and the Stewartson profile function values, with the same initial slope as the linear interpolation line used by Head, to provide the intermediate values of the functions f_2 and f_3 .

An example of the variation of these function values with c is given in Fig. 5.3 for f_2 at three values of n . From this figure, it is clear that, generally, there is a sharp change in the value of f_2 associated with the separation region. Similar behaviour of the function f_3 was apparent and was considered to be entirely consistent with the classically held view (Ref. 46) of a dramatic change in the boundary layer as the separation point is passed.

Using the above interpolation scheme, it was possible to build up a series of profiles for each value of c by varying the value of d . It was found, in accordance with the findings of Head for attached flow, that there was a limited range of d , for each value of c , from which physically realistic profiles were obtained.

In order that only physically acceptable profiles were used, a computer program was constructed to generate and filter possible profiles before any function relationships were developed from them. In the filtering process, the profile would only have been acceptable if $u/U < 1$ at all points on the profile, and if $H > 0$. Typically, up to two thousand profiles were calculated for every ten values of d . In Fig. 5.4 a range of profiles, corresponding to the variation in c between the Stewartson profile average value and the separation profile value, are presented for one value of d . Profile generation beyond the Stewartson profile value of c was also attempted, but this only produced a limited number of physically acceptable profiles.

Once a large number of separated flow profiles had been generated, it was necessary to determine the boundary layer parameters θ , δ^* and ϵ .

This was achieved by integration of the profile velocity distributions by means of the Trapezoidal rule. In this way, the boundary layer parameters for approximately five thousand profiles were obtained. Calculation of the dissipation integral required that the value of

$$\int_0^1 \frac{1}{u_e} \left[\frac{\partial u}{\partial n} \right]^2 dn$$

be known. To obtain this value, it was first necessary to differentiate the functions f_2 and f_3 for each of the three sets of profiles. The two 'attached' cases had been previously calculated by Head (Ref. 34), leaving only the Stewartson profile functions which were differentiated graphically.

The calculated function derivatives for all three cases are presented in Fig. 5.5. Intermediate values of the function derivatives corresponding to each of the developed profiles could then be obtained by a similar interpolation scheme to the one used for the functions themselves. It was felt that, since the curve used was defined by essentially similar boundary conditions in both cases, the interpolated derivatives would be representative of the intermediate profiles to which they corresponded. An example of the variation of the derivative of f_2 with the variation in c , is given in Fig. 5.6 for three values of n .

Once the function derivatives had been determined for each value of n , the value of the above integral could be calculated, since

$$\frac{1}{u_e} \frac{\partial u}{\partial \eta} = f_1' + cf_2' + df_3' \quad (5.17)$$

Fig. 5.7 illustrates the profile derivatives calculated, in the above manner, for one value of d .

When all the boundary layer quantities had been established, it was possible, by taking θ as the characteristic length, to derive the appropriate values of H , H_e and D^* corresponding to each profile. In order that the original contour charts of Head could be extended to establish whether continuity between the attached and separated flow profiles had been preserved, the parameters l and m were also calculated. In Fig. 5.8 the developed profiles, which all lay in the region $m > 0$ and $l < 0$, are presented along with the original contours developed by Head for $m > 0$. Each parameter chart displayed the required continuity between the new separated flow profiles and those developed by Head.

The parameter charts provide a graphic illustration of the behaviour of the boundary layer as the separation point is passed. In general, the parameter m increases, prior to separation, until, at separation, the value drops sharply to approximately zero with the relaxation of the adverse pressure gradient. According to the charts, this behaviour would result in a dramatic change in the value of H and, to some extent, H_e around the separation point. This result is in agreement with previous observations on laminar separation (Ref. 46).

The growth of the form parameter, suggests that the maximum growth rate of this term occurs just after the separation point. The general behaviour of the energy form parameter is more difficult to determine,

since the position of its minimum value is dependant on the magnitude of m throughout the calculation. It must be noted, however, that the data of Head contained values derived from profiles with suction and, as such, it would be unlikely that the minimum value of H_e would be achieved prior to separation. It would appear, therefore, that the minimum value of H_e would occur near to, but just after, separation and corresponds to the result obtained by Assassa and Papailiou (Ref. 33) for turbulent flow.

It can be observed, in the final chart presented in Fig. 5.8, that the dissipation integral, in the separated region, becomes strongly dependant on the value of the pressure gradient parameter m , and that there exists a value of m above which, increased dissipation would occur, and below which the value of the dissipation integral decreases. The explanation of the decrease in dissipation integral as the value of m decreases may come from the associated relaxation of the pressure gradient. Since dissipation within the boundary layer is dependant on the rate of deceleration of the flow, the near constant pressure apparent after laminar separation may be responsible for the behaviour of the dissipation integral as indicated by the chart.

The range of parameter values presented for the separated flow region was limited by the fact that the solutions became non-unique for $H \geq 10$. If the parameter charts had been plotted fully, then they would have shown multivalued parameters corresponding to one set of l and m values. The implication of this result is that, assuming the calculation could have passed the separation point, the method of Head would have been unable to calculate the boundary layer development if any significant amount of separated flow had been present. The current technique, however, utilises

parameter relations which are single valued and, as such, the method is unaffected by this particular result.

5.2.2 Derived Function Relationships

To incorporate the separated flow profile parameters into the new technique, it was necessary to develop a similar series of functional relationships as those required for solution of the attached flow problem. Initially, two plots were made to establish the behaviour of the parameters with respect to each other. In Fig. 5.9, where the values of form parameter H are plotted against the energy form parameter H_e , it can be observed that the graph exhibits the essential features of that developed by Assassa and Papailiou (Ref. 33) for turbulent flow. The most significant feature is the increased scatter in the immediate post separation region. The same phenomenon is also apparent in Fig. 5.10 where the dissipation parameter D^* is related to the form parameter. This scatter, however, is somewhat misleading, since the unrealistic points provided by the profiles exhibiting high values of m contribute significantly to the randomness shown.

It was possible, on the basis of these two graphs, to extend the functional relationships derived for attached flow to accommodate separated flow. To do this, the new data points were filtered and a cubic spline was fitted to the result. These spline-fits, for the two relations, along with the points used to define them, are presented in Figs. 5.11 and 5.12. The behaviour shown by the dissipation integral around the separation point is consistent with that observed from the contour charts,

in that, the rate of decrease in its value with H reduces near separation and the subsequent behaviour is much as that observed for the lower values of m .

The skin friction relation for attached flow employed a rather complex interpolation routine which, in the interests of computational efficiency, was avoided for the separated flow region. To do this, the variation of the skin friction with changes in form parameter was studied with a view to developing an appropriate relationship. A plot of the relationship between the parameter l and the form parameter is presented in Fig. 5.13 where it can clearly be seen that the scatter around the post separation region is significant. By first specifying the value of H at separation and then by filtering the available data, it was possible to produce an acceptable spline-fitted representation of the relationship. It should also be noted from Fig. 5.13, that the value of l changes very little with H after separation. This would indicate, as has been shown by recent experiment and numerical analyses (Refs. 17 & 47.), that the magnitude of skin friction after separation remains small provided the flow is laminar.

As in the attached flow calculation, it was necessary to integrate the H versus H_e relation to produce the required H versus L curve, since

$$L = \int \frac{1}{H - 1} \frac{dH_e}{H_e} + C \quad (5.18)$$

The constant of integration was taken such that $L = 0$ when the H versus H_e curve exhibited a minimum. Once the relation had been developed, the full H versus L curve for attached and separated flow was represented by a simple spline-fit (Fig. 5.14).

5.3 Application of the Method to Laminar Separation Problems

The above separated flow development was encouraged by the need to account for laminar separation bubbles effects and so, it was felt that the test cases used to establish the effectiveness of the calculation should be indicative of these effects. Of the test cases considered, two are presented here. In both cases, the pressure distribution was a prescribed input to the calculation which, in turn, provided the boundary layer parameter development as output.

The first case was to some extent unrealistic in that, up to separation, the pressure distribution for the GA(W)-1 aerofoil at twenty degrees was used with the post-separation pressure assumed constant. It was considered, however, that this distribution would be a reasonable approximation to the real flow within a separation bubble. The calculated boundary layer development for this distribution (Fig. 5.15) appeared to be satisfactory with the discontinuity in pressure gradient, at separation, being manifest in the behaviour of the momentum thickness. Otherwise, smooth predictions of the boundary layer parameter development were obtained and no difficulty was experienced when passing through the separation point.

The above calculation was then repeated with an unmodified inviscid pressure distribution (Fig. 5.16) after the separation point. On reaching separation, the calculation failed to indicate any subsequent increase in form parameter. This was expected since, during the development of the velocity profile family, it was only possible to establish acceptable profiles for a limited range of the pressure gradient parameter m . A

further calculation was conducted to establish the degree of relaxation required to allow the separation point to be passed. The resultant pressure distribution obtained exhibited no significant alteration, but the predicted development of the boundary layer was unlikely to be representative of the actual flow within a separation bubble as the post-separation growth of the form parameter was almost negligible. Several more tests were carried out to ascertain whether the pressure distribution after separation would always require relaxation to permit a solution to be obtained. In general, it was found that the velocity distribution only required relaxation in very severe pressure gradients.

The calculated velocity distribution of Gleyzes et al (Ref. 17), for an enlarged leading edge at $Re = 2.2 \times 10^6$ was used as the input velocity distribution to establish the predictive accuracy of the new method. For comparative purposes, the location of transition was specified to coincide with the original inverse calculation of Gleyzes et al although, the correlation of Roberts (Ref. 30) indicated that transition would occur within one percent of this value. The prediction of form parameter development obtained from the direct scheme is compared with the inverse solution in Fig. 5.17. It is clear from the figure that, although some disagreement is apparent, the two predictions are of the same general form. The irregular nature of the direct prediction was found to be related to the quality of the spline-fit representation of the input velocity distribution.

In all the calculations, where a physically acceptable result was achieved, no stability difficulties were experienced when passing through the point of laminar separation. Some difficulty, however, was

encountered just after separation, when the value of the parameter L became very small. It was found that, in this region, calculation stepsize became very important and that, if this was inappropriate, negative values of L would result. This problem arose from the requirement for the accurate specification of all the functions in this region, especially around the minimum in the H versus L curve. Although some mismatch in these functions was apparent, calculation breakdown could be avoided by an appropriate stepsize being chosen. A systematic reduction in stepsize, based on L , was, therefore, implemented in the calculation which reduced the effect of any such functional mismatch.

5.4 Extension of the Turbulent Boundary Layer Calculation

To calculate the turbulent free shear layer, the method of Assassa and Papailiou (Ref. 33) was employed. It was, however, necessary to investigate the validity of the parameter correlations, since these had been developed for much higher Reynolds numbers than those of the present study. In particular, the effect of the extra terms in the Kuhn-Nielsen (Ref. 38) representation of the Coles (Ref. 37) velocity profile family, which were used to derive the above parameter relations, required a detailed examination.

The iterative calculation scheme for the velocity profile calculation used during the analysis of the turbulent boundary layer, became unstable as the displacement thickness Reynolds number was reduced below about 10 000. This phenomenon appeared to be due to the increasing significance of the exponential terms in the velocity profile representation. Several tests were conducted to examine the behaviour of the profile shape as the Reynolds number was reduced, the results of which are presented in Fig. 5.18 for $H = 8.0$. The behaviour of the profile in the wall region appeared to be strongly dependant on the displacement thickness Reynolds number. The distortion associated with the lower Reynolds numbers resulted in profile shapes, unlike those obtained via experiment (Ref. 33), being produced. A similar comparison (Fig. 5.19) again illustrates the problem, but this time for a form parameter indicative of attached flow, where it may be observed that, at lower Reynolds numbers, the wall region velocity gradients are considerably lower than those normally associated with turbulent flow (Ref. 39).

The turbulent boundary layer velocity profile is, by nature, a composite profile and, as such, was amenable to examination in its constituent parts. The previous analysis was therefore repeated, but this time, with the contribution due to the extra exponential terms removed. Figure 5.20 shows a much closer comparison between the profiles at different Reynolds numbers as a result of the removal of these terms. The contributions to the profile shape, for the highest and lowest Reynolds number, from the extra exponential terms, are shown in Fig. 5.21. It may be observed that the effect of these terms at the highest Reynolds number is confined to the wall region, whereas in the case of the lowest Reynolds number, the effect is more pronounced all through the boundary layer. Since the original reasons for the inclusion of these terms was to provide a smooth transition between the turbulent flow and the wall, through a laminar sublayer (Ref. 38), their influence on the outer region of the overall profile calculation should be small. It was therefore decided to scale these exponential terms to provide, at low Reynolds numbers, a similar effect to that observed at the highest Reynolds number. This was achieved by, first, correlating the required scale factor against the value of displacement thickness Reynolds number, and then incorporating the obtained correlation into the iterative profile calculation. The developed correlation is presented in Fig. 5.22 and was represented, within the calculation, by polynomial. The velocity profiles produced via this scaling technique, for the various Reynolds numbers, are shown in Fig. 5.23. and appear to be more physically acceptable than those previously obtained.

The similarity between the low and high Reynolds number velocity profiles produced by this method rendered the relations derived by Assassa

and Papailiou (Ref. 33) valid for the present calculation although they were recalculated in order that any inherent Reynolds number dependence, of the basic profile representation, be accounted for. The calculated relations of H versus H_e and H versus L , for attached and separated flow, are presented in Figs 5.24 and 5.25.

As in the attached flow calculation, closure was obtained via the Nash π - G (re) relation, where the expression was used to relate the absolute values of π and G . All other relations are as presented in chapter three.

5.5 Comparative Studies

The inverse calculation of Gleyzes et al, for the enlarged leading edge case, provided a test case for the developed full boundary layer technique. As in the laminar separation case, the pressure distribution calculated via the inverse scheme was used as the input to the direct boundary layer calculation scheme. This pressure distribution was represented by spline-fit through a number of discrete points. The results of the direct calculation are compared with the inverse solution in Fig 5.26.

It is clear from the figure that the direct calculation predicted slightly higher values of momentum thickness growth, associated with the turbulent part of the separation bubble, than the calculation of Gleyzes et al (Ref. 17). The associated rate of decrease from the peak value of form parameter was also somewhat slower in the direct calculation. It is of significance, however, that the general form of the two predictions was very similar and that no difficulty was encountered at separation or reattachment in the direct case.

The discrepancies between the direct and inverse solutions may have arisen from two sources, the first of which was the quality of the spline fit representation of the pressure distribution. It was found that the boundary layer parameter prediction obtained, in the separation bubble, was influenced by the specification of the pressure distribution. This was particularly pertinent to the transition location where the value of form parameter was especially sensitive and would often increase after transition, contrary to experimental observation (Ref. 17), if the adverse

pressure gradient was insufficient.

The second reason for disparity between the inverse and direct boundary layer calculations comes from the empiricism present in the two methods. It is true, as has been demonstrated for attached flow (Ref. 40), that the empiricism and closure hypothesis employed in a specific turbulent boundary layer calculation technique, may produce results unique to that particular method. For separated flow, such effects are likely to strongly influence the obtained result which may be further affected by the non-equilibrium nature of the flow.

A comparison was also made with the predictions of Davis et al (Ref. 47) for the NACA 66₃-018 aerofoil originally tested by Gault (Ref. 14). As in the previous test, the velocity distribution output from the inverse calculation, which was in close agreement with the measured data, was used as the input to the direct scheme. In this case, however, it was found that the direct laminar boundary layer calculation did not predict laminar separation at the same location as the inverse scheme. This result is in agreement with the findings of Gault (Ref. 14) who also carried out a boundary layer calculation for this aerofoil and found that the predicted separation point lay well behind the measured location. As a result of the previous success of the prediction scheme used by Gault, it was concluded that the empirical data should be treated with some caution.

To obtain a valid comparison, it was, therefore, necessary to increase the magnitude of the adverse pressure gradient just prior to the separation point in order that the predicted direct and inverse separation

points should be consistent. The adjusted pressure distribution, along with the original inverse prediction, is presented in Fig. 5.27. The laminar portion of the adjusted distribution was taken to have a constant pressure.

The results of the direct calculation compared with the inverse solution are presented in Fig. 5.28. It was considered that the results from the direct calculation, although somewhat artificial, were similar in form to the inverse solution with the greatest discrepancy occurring over the adjusted laminar portion of the bubble. The disagreement between the two attached laminar boundary layer skin friction predictions was significant. This may have been due to an over-prediction by the inverse code which, when compared to empirical data (Ref. 47), has been shown produce higher than expected values of skin friction.

Considerable agreement was obtained between the predicted momentum thicknesses. The variation of form parameter was also of a similar form to the inverse solution but, due to the adapted input velocity distribution, did not achieve the required growth rate in the laminar portion. The behaviour of the form parameter around transition was again found to be very sensitive to the velocity distribution and, in this case, appeared to be discontinuous.

In the above calculations, no difficulty was experienced when passing through the separation or reattachment points. Some difficulty was, however, experienced just after laminar separation due to the function behaviour in this region. As a result, a small discontinuity is present in the predictions. It is likely that this problem would be alleviated by

careful matching of the spline-fit relationships in this area.

5.6 Separation Bubble Calculations Based on Horton's Method

The simple method derived by Horton (Ref. 16) to predict the growth and bursting of laminar separation bubbles has been demonstrated (Refs. 16 & 30) to provide a velocity distribution, over a separation bubble, similar to that obtained by experiment. An investigation was therefore conducted to assess the effect which such a distribution would have on the subsequent turbulent boundary layer growth as predicted by the direct calculation scheme.

A number of cases, where separation bubble effects appeared to be predominant, were considered with the calculated attached boundary layer growth and separation points used to construct the separation bubble pressure distribution. A typical result is presented in Fig. 5.29, for the NACA 4415 aerofoil at 14.5 degrees incidence and a Reynolds number of one million. From the figure it may be observed that the calculated boundary layer growth associated with the bubble was less than that which would result from a natural transition. This result was confirmed for all the other cases. The calculations of Gleyzes et al (Ref. 17) for short separation bubbles, in some cases, produced results of a similar nature. Generally, however, significant boundary layer growth, above that of natural transition, would be expected from a separation bubble (Ref. 17).

The reason from the lack of boundary layer growth, in the turbulent portion of the separation bubble, may lie in the specification of the velocity distribution at the transition location. It is clear, from the figure, that the form parameter distribution exhibited a sharp peak around the transition location, rather than the smooth curve associated with

inverse calculations (Ref. 47). This peak resulted in a rapid reduction in form parameter just after transition and, since the maximum rate of momentum thickness growth was experienced at high values of form parameter, a reducing rate of boundary layer growth.

To investigate the dependence of the result on the specification of the velocity distribution around the transition location, a slight relaxation of the adverse pressure gradient was introduced just after transition. The results of this calculation are presented in Fig. 5.30 and show an increase in the boundary layer growth over the previous calculation. It was therefore concluded that the specification of the velocity distribution around the transition location was of prime importance to the accuracy of the developed direct calculation scheme.

RESULTS OF THE PREDICTIVE SCHEME

6.1 Introduction

To assess the analytic capability of the overall predictive technique (Ref. 50), a number of comparisons with wind tunnel data were made. These data were obtained for a variety of test facilities and cover the Reynolds number range 5×10^4 - 6×10^6 . The input coordinate data to the program was as published (Refs. 51,52) except for the NACA four and five digit sections which were computer generated from standard functions (Ref. 53). The relative dearth of data at very low Reynolds number has, at present, limited the study of laminar separation to two aerofoil sections. For turbulent trailing edge separations, however, there is no such shortage of data and so several aerofoils exhibiting such effects have been considered. In the cases where experimentally obtained pressure data were available, comparison has been made with the computed distributions.

6.2 GU25-5(11)8

The GU25-5(11)8 aerofoil (Fig. 6.1) was developed as one of a family of sections specifically for man-powered flight and, to date, remains the only one to have been wind tunnel tested (Ref. 54). The aerofoil has been used for a number of applications, most notably as the canard wing of several microlight aircraft. Recently, some very low Reynolds number wind tunnel tests were conducted (Ref. 29) to assess its low Reynolds number performance. It was found, that the aerofoil exhibited gross laminar separation, at all positive angles of attack, below $R_c=1 \times 10^5$, and that the loss in lift associated with this condition was substantial. Comparisons between the lift characteristics above and below $R_c=1 \times 10^5$, along with predicted values for the lower Reynolds number case, are presented in Fig. 6.2.

Throughout the angle of attack range, there were several discontinuities in the calculated and empirical lift curves. The former was due to the susceptibility of the pressure distribution to the separation point when such a large region of separated flow exists, and the latter to the practical difficulties in obtaining data at such low Reynolds numbers. At low angles of attack, it is clear that the technique over-predicted the value of lift coefficient. This is echoed in Fig. 6.3 where it may be observed that the suction peaks associated with the two lowest angles of attack are also over-predicted. The reason for this is not clear, although the Wake Factor correlation, which is only tentative, may have had a significant influence. At each angle of attack, however, the level of the constant pressure region shows good agreement, with only small differences in the measured and calculated suction peak pressure

coefficient values at the higher incidences. It is suggested, that the variance in the calculated values, however, lies within the experimental tolerance.

It should be noted that there is no indication of maximum lift being achieved within the range of incidence considered. This was not unexpected, since the aerofoil exhibited laminar separation at all angles of attack. It was considered that the empirical data obtained around the measured turn over point (25°) would be highly three-dimensional and, as such, not amenable to analysis by the present scheme.

In Fig. 6.4 the calculated and empirical pressure coefficient distributions at 12.6 degrees are presented for three Reynolds numbers. At $R_c=1 \times 10^5$ there is poor agreement in the location of separation. This may have arisen from the constraint of using given wind tunnel model coordinates, which limited the input polygon to less than fifty panels, thus reducing the achievable accuracy of the inviscid calculation and the subsequent separation point determination.

A limitation of the present approach is highlighted in the pressure coefficient distribution for $R_c=1.5 \times 10^5$. Here the measured pressure coefficients in the separated region increased towards the trailing edge. This is typical of a wake which, after transition, closes rapidly towards the trailing edge. The pressure distribution produced by such a wake resembles that of a long separation bubble (Ref. 18), albeit no re-attachment occurs on the aerofoil. The evident recovery is enhanced with increasing Reynolds number, until a long separation bubble is formed. Such a condition cannot be effectively modelled by a constant pressure

wake, but, in the present method, a warning of when this condition is likely to exist is given by the long bubble reattachment criterion (Ref. 44) described in Chapter four.

6.3 Wortmann FX63-137

The Wortmann FX63-137 aerofoil section (Fig. 6.5) has recently attracted considerable interest for application to R.P.V's (Ref. 1). Experiment has shown that this section exhibits gross laminar separation below a Reynolds number of 70000 (Ref. 51), and so provides a suitable test case for the developed laminar separation prediction scheme.

In Fig. 6.6 the calculated lift curve, for a Reynolds number of 60000, is compared with that obtained by experiment in the Stuttgart 0.37m x 0.6m wind tunnel (Ref. 51) which has a turbulence intensity of 0.08%. It may be observed from the figure that, although a general over-prediction was obtained, the agreement between the two curves was significant. Some discrepancies are, however, apparent at either end of the lift curve.

The maximum angle of attack encompassed by the calculation was 12.0 degrees, where the section exhibited separated flow over ninety three percent of the upper surface. For angles above this, the proximity of the separation point to the leading edge resulted in a lack of calculation convergence associated with the interaction between the upper free shear layer and the aerofoil surface. It is likely that, to a lesser extent, the predictions obtained for the last two incidences were similarly affected.

At the lowest angle of attack (-3.0 degrees), the calculation significantly under-predicted the value of lift coefficient. Further analysis of this case indicated that, at this angle, the aerofoil exhibited approximately fifty percent separation on the upper surface and

seventy five percent on the lower surface. Since the present technique can only model separation from one surface, the discrepancy, between calculation and experiment, may have been due to the failure to account for the considerable lower surface separation present in this case.

This section, originally developed for general aviation purposes, has been extensively used in wind energy generation and more recently for low-speed microlight applications. The aerofoil, which is a 17% thick section with the maximum thickness lying at approximately 40% chord, exhibits some supercritical features such as a relatively blunt nose and a cusped lower surface near the trailing edge. The aerofoil profile is presented in Fig. 6.7.

The experimental data for the GA(W)-1 aerofoil which were obtained in the NASA Low Turbulence Pressure Tunnel (Ref. 52) (LTPT) have been used on a number of occasions (Refs. 8,28) for assessing the accuracy of predictive schemes. The stall exhibited by this section is, for medium Reynolds numbers, a classic trailing edge type stall with the separation point moving relatively slowly from the trailing edge to the leading edge on the upper surface. This behaviour is ideal for analysis by most predictive schemes, since the unusual viscous effects, often present when rapid separation point movement occurs or when significant separation bubble effects are present, do not require to be accounted for.

Since the present technique is only capable of modelling upper surface separations, negative angles of attack were calculated by inverting the aerofoil profile and then calculating for positive incidences.

In Fig. 6.8 comparison is made, between the lift and pitching moment coefficients, for three Reynolds numbers. At $R_c=2 \times 10^6$, the general trend of the lift curve is predicted, albeit there are some deviations, notably

at 8 and 12 degrees. The anomaly at 8 degrees arises from the position of upper surface separation being almost coincident with the trailing edge. The associated rapid thickening of the boundary layer produces an abnormal discontinuity in the profile shape which, in turn, results in an uncharacteristic orientation of the trailing edge wake. To alleviate this problem, the growth of the boundary layer at the trailing edge was restricted if separation was predicted after 95% chord. Even with this restriction, however, some deviation still existed, as is apparent from the figure. A similar effect is evident at the highest Reynolds number for an incidence of 10 degrees.

To account for viscous effects between iterations, the aerofoil contour was adjusted via a suitable displacement of the panel corner points. This made the modelling of rapid boundary layer growth, within a panel, a most difficult procedure. It was particularly relevant to the panel containing the separation point, and manifested itself via the calculated value of C_L at 12 degrees incidence ($Rc=2000000$) where it may be observed that a marked over-prediction was obtained. It was found that, generally, the smoothness of the prediction obtained was influenced by this effect.

For all three Reynolds numbers considered, the pitching moment coefficients for negative incidences, were under-predicted. Although there was no apparent reason for this discrepancy, the calculated lift was slightly higher than that measured. This indicated that too much lower surface separation was predicted resulting in a reduced pitching moment. This may have been due to the failure of the technique to accurately model the cusped upper trailing edge exhibited by the inverted profile.

When relatively large areas of separated flow exist over an aerofoil, the constant pressure region aft of the separation point can have a significant influence on the value of pitching moment coefficient when it is obtained via an integrated pressure distribution. This would appear to be the case in Fig. 6.8 for $R_c=6 \times 10^6$, where the calculated value in the region of stall was larger than the measurements.

The predicted value of maximum lift was good for the lowest Reynolds number considered but was slightly poorer for the other two cases. The least satisfactory prediction was obtained at $R_c=4 \times 10^6$ where, after stall, a progressive under-prediction of the value of lift coefficient occurred. In this case, the difference between the two maximum lift values was about 3% and the stall angle was in error by 0.5 degrees.

Fig. 6.9 presents selected comparisons of calculated and empirical pressure distributions at the highest Reynolds number. Generally, the values of peak suction are in agreement except at 12.04 degrees where the separation point was near the trailing edge and the pressure distribution was therefore subject to the above mentioned trailing edge effects. The pressure distributions for 16.04 and 20.05 degrees show some discrepancy between measured and calculated separation points. The predicted movement of the separation point, through the angle of attack range, was found to be influenced by the polygonal panel distribution and, more particularly, the relative position of separation within a panel. In each of the two cases, however, the apparent separation point on the measured distribution was within one panel length of the predicted position.

The current modelling of the wake by a constant Wake Factor would

appear to be reasonably satisfactory for the turbulent separation cases considered, since, for the four distributions presented, there is good agreement between the predicted and measured profiles.

6.5 NACA 4412 and NACA 4415

These two aerofoil sections (Fig. 6.10) are typical of many in general use and, as such, provide good test cases for predictive codes. The wind tunnel tests, which provided the empirical data, were conducted in the NASA Low-turbulence tunnel facility (Ref. 51) and at Reynolds numbers from 1×10^6 to 3×10^6 .

In Fig. 6.11 lift coefficient characteristics are presented at three Reynolds numbers for the NACA 4412 section. In all three cases, the empirical and predicted lift curve slopes are in good agreement. The initiation of separation, however, as for the GA(W)-1 aerofoil, is accompanied by a discontinuity in the predicted curve. This condition only exists for approximately one degree in the incidence range. The prediction of maximum lift is within 3.5% of the experimentally obtained value for all three Reynolds numbers although, for $R_c = 2 \times 10^6$ and $R_c = 3 \times 10^6$, stall is predicted one degree earlier than experiment would indicate. The reasons for the difference in stall angle are not clear but may be due simply to the inability of the present technique to model the relevant flow phenomena accurately.

The maximum lift and stalling characteristics of the NACA 4415 aerofoil have proved difficult to predict, albeit the corresponding lift curve slopes (Fig. 6.12) show good agreement. At the lowest Reynolds number, however, there was a significant over-prediction of both maximum lift and the stall angle. It was considered that this case may have indicated the presence of a laminar separation bubble and so the current inability to account for these and their subsequent effect on the

turbulent boundary layer growth, influenced the predictive accuracy. The magnitude, however, of the disparity between prediction and experiment was rather large and may have been due to the inherent weaknesses of the constant Wake Factor assumption as demonstrated by Dvorak and Maskew (Ref. 28).

One effect, however, of a separation bubble can be to cause earlier turbulent boundary layer separation and thus enhance the stall. An increased Reynolds number would tend to reduce the influence of a bubble on the maximum lift. This appeared to be the case here, since the agreement improved at the two higher Reynolds numbers. To investigate this phenomenon, an approximate calculation including a separation bubble was conducted to assess the shift in separation point and associated lift loss resulting from such a bubble. Figure 6.13 presents the pressure coefficient distributions obtained for the NACA 4415 aerofoil at 14.5 degrees for a Reynolds number of 1×10^6 with and without a separation bubble. The distribution incorporating a separation bubble was obtained by calculating, using a relaxed Horton type pressure distribution, the bubble dimensions and the movement of the turbulent separation point associated with the increased boundary layer growth. The bubble dimensions along with the new separation point were then input to the inviscid bubble calculation and a pressure distribution thus obtained. This was then compared to an inviscid calculation with the original input separation point. It is clear that, although some decrease in the lift is apparent, the magnitude of this decrease is insufficient to account for the disparity between the measured and predicted lift coefficient.

Although there were some irregularities in the lift curves around the

stall, the maximum lift was within 4% of the empirical value in both cases. The jagged nature of these predictions around stall may have been linked to the treatment of the boundary layer growth on the separation panel and the subsequent effect which this had on the level of the constant pressure region.

The NACA 23012 aerofoil (Fig. 6.14) is a twelve percent thick section which has been used, amongst other things, for rotary wing applications. The test data used for comparative purposes were obtained via two different facilities (Ref. 51) and highlight the kind of disagreement often experienced between different wind tunnels. The two tunnels used for comparison were the NASA Low Turbulence Tunnel and the IAG Stuttgart Laminar Wind Tunnel.

Fig. 6.15 presents comparisons between the lift curve prediction obtained from the analysis scheme and empirical data from the two facilities. It is clear from the figure that the disagreement between the results obtained from the two tunnels is quite significant, especially at the lowest Reynolds number. The level of correspondence between the two facilities, generally, improves with increasing Reynolds number as may be expected since the influence of extraneous flow phenomena tends to reduce with increasing Reynolds number (Ref. 6).

At a Reynolds number of 1×10^6 , the predicted lift curve is considerably different from both measured data sets. Whilst the predicted maximum lift shows good agreement with the NASA data, the lift coefficient at the lower angles of attack, when a fully attached flow state exists, is under-predicted. It is interesting that the prediction agrees more closely with the NASA data than with the Stuttgart data for most incidences. This is a particularly good example of the reasons for extreme care being taken when analysing and collecting empirical data since, in this case, the prediction obtained is poor compared with one

data set, but significantly better when compared with the other.

The mid-range angle of attack prediction for $Re=1.5 \times 10^6$, for which a relatively large number of consecutive angles of incidence were calculated, is of an irregular nature. The reason for this is not clear, although the position of the separation point near the trailing edge may have influenced the obtained results. For this Reynolds number, the lift prediction up to and at stall is, however, good.

The lift curve predicted for $Re=2.0 \times 10^6$ shows good agreement with the data obtained via the Stuttgart facility for low to medium range incidences. Once, however, significant separation is apparent, the quality and smoothness of the prediction deteriorates and the maximum lift coefficient is under-predicted. The jagged nature of the lift curve around stall was, again, found to be related to the position of separation and the associated growth of the boundary layer within a polygonal panel.

Of the four Reynolds numbers considered, the calculation at $Re=3 \times 10^6$ exhibited the greatest agreement with the two empirical data sources over the full angle of attack range. The predicted lift curve was relatively smooth and, in general, was within three percent of the measured values of lift coefficient. The stall prediction, although slightly low, was of the same form as the two empirical curves. It is interesting to note that, at the highest Reynolds number, when separation bubble and extraneous flow effects are least, the best prediction was obtained. This was also the case for the majority of other aerofoils considered.

Figure 6.16 presents comparisons, between the empirical data and

prediction, of the drag coefficient for the two lowest Reynolds numbers. It is clear, from this figure, that the variation between the two facilities is again significant, especially at the lowest Reynolds number. The prediction obtained, for both cases, was rather irregular in nature, although some agreement with the measured data was apparent. The method used to calculate the drag coefficient was a simple pressure and skin friction integration scheme and, as such, was prone to significant error in the region of the suction peak. For this reason, the drag calculation output must be treated with some care, and should only be considered as points through which a best-fit line may be drawn.

The predicted separation characteristics, for the Gottingen797 aerofoil (Fig. 6.17), are compared with those obtained experimentally at Cranfield Institute of Technology (Ref. 55) in Fig. 6.18. The measured separation front exhibited a monotonic variation whilst the predicted values progressed in a steplike manner. There was, however, no associated stepping effect on the lift curve (Fig. 6.18), although, some degree of discontinuity was apparent and was undoubtedly linked to the behaviour of the boundary layer on the separation panel. At all angles of attack, the prediction of separation was within 5% chord of the experimental location and the general trend of the two separation characteristics was similar.

The difference in maximum lift values was about 6%, and this occurred at the point of greatest disagreement in the separation characteristics. The overall agreement may have been improved by a more appropriate panel distribution since, the panel distribution used produced some discontinuities in the panel method output near the leading edge. Figure 6.19 demonstrates this effect for an angle of attack of 8 degrees where the prediction around the suction peak is rather jagged. It is likely, however, the quality of prediction was most strongly influenced by the accuracy of the separation point. It is clear, from the figure, that, for this particular case, separation is predicted prematurely. This resulted in a reduced suction peak and an over-prediction of the constant pressure region.

CHAPTER 7

CONCLUSIONS

The increased understanding of the mechanisms governing low Reynolds number aerofoil performance has, to some extent, produced a requirement for appropriate analysis techniques. In the present study, a two-dimensional aerofoil performance analysis procedure for low Reynolds number incompressible flow has been developed. This predictive scheme exhibits a number of unique features, including a long laminar separation bubble reattachment criterion, and has been demonstrated capable of accounting for both laminar and turbulent separations with some success. Further to this, a subsidiary direct boundary layer calculation scheme, capable of considering laminar separation bubbles, has also been developed.

For laminar separation, a tentative Wake Factor Increment correlation has been developed to account for the effect on wake closure of the free laminar shear layer. This correlation has been shown to work well for two aerofoil sections tested in different facilities but requires further investigation to establish its general applicability. As yet, this incrementation technique has only been used for very low Reynolds number cases where laminar separation exists at all incidences. It may also, however, be useful for analysis of the post stall behaviour of aerofoils at higher Reynolds numbers.

It has also been demonstrated that the constant pressure wake model

utilised by the technique may be inappropriate to some laminar separation cases where pressure recovery is apparent within the separated region. The low Reynolds number range of the method is also limited by the inability to model large regions of simultaneous upper and lower surface separation.

A long separation bubble reattachment criterion based on the method of Horton has been developed. This criterion has been shown to accurately indicate the Reynolds number at which free shear layer reattachment takes place on the GU25-5(11)8 aerofoil for a range of incidence. It is likely, based on the current result, that the method may be more applicable to sections exhibiting mid-chord separation bubbles rather than leading edge ones. This is because the technique relies on the accuracy of the laminar separation prediction which deteriorates close to the leading edge. It is clear, however, that further examination and testing of the criterion is required once more empirical data become available.

The aerofoil analysis procedure has been shown to accurately predict turbulent separations on several aerofoil sections, when compared with empirical data sources. The corresponding lift and pitching moment calculations displayed good agreement with those obtained by experiment. The quality of the drag prediction was, however, less satisfactory and requires further development before it may be used with as much confidence. For the considered turbulent separation cases, transition was fixed to occur at the point of laminar separation if no natural transition was indicated. Although laminar separation bubble effects were not included within the analysis procedure, the results obtained indicate that their effect, for the considered cases, was adequately modelled by this

approach above $R_c = 1 \times 10^6$.

A direct boundary layer calculation routine has been developed whereby, for a prescribed pressure distribution, the growth of the boundary layer through a laminar separation bubble may be assessed. This technique, which has been compared with inverse calculations and found to exhibit general agreement, encountered no difficulty when passing through separation and reattachment points. It is envisaged that the method may also be utilised in conjunction with empirical pressure distributions to directly assess the effects of separation bubble formation on test sections.

Ultimately, it would be desirable to include this, or some other, boundary layer calculation scheme, capable of accounting for laminar separation bubbles, within the overall analysis technique. This may be achieved, for the present direct scheme, by the development of a suitable viscid-inviscid matching scheme possibly utilising the developed inviscid separation bubble method. It is clear, however, that, for Reynolds numbers less than 1×10^6 , future development should concentrate on the prediction of separation bubble effects.

Appendix 1. Calculation of Vortex Panel Influence Coefficients

To obtain the influence coefficients C for the basic panel method, the following approach was adopted.

For a given panel, the vorticity at any point on that panel may be expressed in the form

$$\gamma_s = \gamma_j + \left[\frac{\gamma_{j+1} - \gamma_j}{L_j} \right] S_j \quad (a1.1)$$

or rearranging,

$$\gamma_s = \frac{\gamma_j}{L_j} \left[L_j - S_j \right] + \gamma_{j+1} \frac{S_j}{L_j} \quad (a1.2)$$

Given that the induced velocity normal to the surface at the ith control point is

$$\vec{v}_{nij} = \frac{1}{2\pi} \int_0^{L_j} \frac{\gamma_s}{|r_{ij}|^2} (\vec{r}_{nij} \cdot \vec{n}_i) ds_j \quad (a1.3)$$

then by substituting equn. (a1.2) for γ_s the induced velocity may be expressed in the form

$$\vec{v}_{nij} = \int_0^{L_j} \frac{\gamma_j(L_j - S_j)(\vec{r}_{nij} \cdot \vec{n}_i)}{L_j |r_{ij}|^2} ds_j + \int_0^{L_j} \frac{S_j \gamma_{j+1} (\vec{r}_{nij} \cdot \vec{n}_i)}{L_j |r_{ij}|^2} ds_j \quad (a1.4)$$

The above equation may be reduced to the form

$$\vec{v}_{nij} = A_{ij} \cdot \gamma_j + B_{ij} \cdot \gamma_{j+1} \quad (a1.5)$$

It may be observed from the figure A1 that the following definitions apply

$$\vec{r}_{ij} = \left[(x_i - x_p), (y_i - y_p) \right] \quad (\text{al.6})$$

$$\vec{r}_{nij} = \left[(y_p - y_i), (x_i - x_p) \right] \quad (\text{al.7})$$

$$|r_{ij}|^2 = (x_i - x_p)^2 + (y_i - y_p)^2 \quad (\text{al.8})$$

The values of x_p and y_p may be obtained, if the j panel end points are known, from the following equations.

$$x_p = x_j + S_j \cos\theta_j = x_j + \left[\frac{x_{j+1} - x_j}{L_j} \right] S_j \quad (\text{al.9})$$

$$y_p = y_j + S_j \sin\theta_j = y_j + \left[\frac{y_{j+1} - y_j}{L_j} \right] S_j \quad (\text{al.10})$$

By combining the system of equations (al.5 - al.10), it is possible to obtain the values of the coefficients A_{ij} and B_{ij} .

The influence coefficient C_{ij} for the vorticity γ_j then follows from the equation

$$C_{ij} = A_{ij} + B_{ij-1} \quad (\text{al.11})$$

where $2 \leq j \leq n-1$, $C_{i1} = A_{i1}$, $C_{in} = B_{in-1}$ and $1 \leq i \leq n-1$.

Appendix 2. Calculation of the Separation Panel Influence Coefficients

The vorticity distribution present on the separation panel is show in Fig. A2. It is clear from the figure that there are two distinct regions present and, as such, these may be considered separately. The vorticity distribution in each region is given by

$$\text{Region 1: } \gamma_{(i)} = \gamma_j - \frac{\gamma_j}{L_j} S_j \quad (\text{a2.1})$$

$$\text{Region 2: } \gamma_{(ii)} = \gamma_{j+1} + \left[\frac{\gamma_{j+1} - \gamma_{sep}}{L_j - L_s} \right] (S_j - L_j) \quad (\text{a.2.2})$$

Since the velocity at j due to the vorticity distribution may be calculated from

$$\vec{v}_{jj} = \int_0^{L_j} \frac{\gamma_s}{2\pi|r|} dS_j \quad (\text{a2.3})$$

where $r = S_j - S_c$ (a2.4)

the induced velocity due to Region 1 may be expressed as

$$\vec{v}_{jj(i)} = \int_0^{L_s} \frac{\left[\gamma_j - \left[\frac{\gamma_j}{L_s} \right] S_j \right]}{2\pi |S_j - S_c|} dS_j \quad (\text{a2.5})$$

By integrating the above equation, it is possible to express the induced velocity due to vorticity region 1 (V_{jj}) in the form

$$\vec{v}_{jj(i)} = \frac{\gamma_j}{2\pi} \left[\ln \left| \frac{L_s - S_c}{S_c} \right| - 1 - \frac{S_c}{L_s} \ln \left| \frac{L_s - S_c}{S_c} \right| \right] \quad (a2.6)$$

Similarly for Region 2

$$\vec{v}_{jj(ii)} = \frac{1}{2\pi} \int_{L_s}^{L_j} \left[\frac{\gamma_{j+1}}{|S_j - S_c|} + \frac{(\gamma_{j+1} - \gamma_{sep})(S_j - L_j)}{(L_j - L_s) |S_j - S_c|} \right] dS_j \quad (a2.7)$$

which on integration gives

$$\vec{v}_{jj(ii)} = \frac{1}{2\pi} \left[\gamma_{j+1} \ln \left| \frac{L_j - S_c}{L_s - S_c} \right| + \left[\frac{\gamma_{j+1} - \gamma_{sep}}{L_j - L_s} \right] \left[(L_j - L_s) + (S_c - L_j) \ln \left| \frac{L_j - S_c}{L_s - S_c} \right| \right] \right] \quad (a2.8)$$

The total induced velocity on the separation panel, due to the separation panel can thus be found from

$$\vec{v}_{jjT} = \vec{v}_{jj(i)} + \vec{v}_{jj(ii)} \quad (a2.9)$$

and may be expressed in the form

$$\vec{v}_{jjT} = A_{jj} \gamma_j + B_{jj} \gamma_{j+1} + C_{jj} \gamma_{sep} \quad (a2.10)$$

where

$$A_{jj} = \frac{1}{2\pi} \left[\ln \left| \frac{L_s}{S_c} - 1 \right| \left[\left[1 - \frac{S_c}{L_s} \right] - 1 \right] \right] \quad (a2.11)$$

$$B_{jj} = \frac{1}{2\pi} \left[\ln \left| \frac{L_j - S_c}{L_s - S_c} \right| \left[\left[\frac{S_c - L_s}{L_j - L_s} \right] + 1 \right] \right] \quad (a2.12)$$

$$C_{jj} = -\frac{1}{2\pi} \left[\ln \left| \frac{L_j - S_c}{L_s - S_c} \right| \left[\left[\frac{S_c - L_s}{L_j - L_s} \right] + 1 \right] \right] \quad (a2.13)$$

Appendix 3. Inviscid Wake Calculation

The shape of the initial wake estimate is calculated using the method of Dvorak and Maskew (Ref. 28) in the following way

STAGE 1: Calculation of free shear layer intersection point.

In order that the free shear layer intersection point may be calculated, it is first necessary to establish the wake height. By considering Fig. A3, it may be observed that the angle β is given by

$$\beta = \left[\frac{y_{sep} - y_n}{x_n - x_{sep}} \right] \quad (a3.1)$$

and the length h_1 by

$$h_1 = [(y_{sep} - y_n)^2 + (x_{sep} - x_n)^2]^{1/2} \quad (a3.2)$$

The wake height may, therefore, be obtained by

$$WH = h_1 \sin(\alpha + \beta) \quad (a3.3)$$

where α is the angle of incidence.

Once the wake height has been determined, the wake length (WL) may be calculated from

$$WL = WF \times WH$$

(a3.4)

since the Wake Factor (WF) is a specified program input.

The mean wake direction angle (ζ), which bisects the upper and lower curves, may now be calculated from

$$\zeta = (F_1 + F_2) / 2.0 \quad (a3.5)$$

where, as shown in Fig. A3, F_1 and F_2 are the angles at which the vortex sheets leave the aerofoil. The mid-point of the separated region is the calculated from

$$x_m = (x_{sep} + x_n) / 2.0 \quad (a3.6)$$

and

$$y_m = (y_{sep} + y_n) / 2.0 \quad (a3.7)$$

thus allowing the wake intersection point to be determined

$$x_{int} = WL \cos \zeta + x_m \quad (a3.8)$$

$$y_{int} = WL \sin \zeta + y_m \quad (a3.9)$$

STAGE 2: Determination of the parabolic curves.

Once the shear layer intersection point has been established, it is then necessary to determine the shape of the shear layers. Since the initial estimate consists of two parabolic curves, three boundary conditions are

used to define each curve. Considering the upper shear layer, then

$$y_{sep} = ax_{sep}^2 + bx_{sep} + c \quad (a3.10)$$

$$y_{int} = ax_{int}^2 + bx_{int} + c \quad (a3.11)$$

and

$$\tan F_1 = 2ax_{sep} + b \quad (a3.12)$$

The above three equations may be solved simultaneously for a,b and c thus yielding the initial shape of the upper free shear layer.

STAGE 3: Panelisation

The curves used to define the initial wake estimate are always almost parallel to the x axis. For this reason, it is possible to divide up, for example, the upper parabolic curve by use of the equation

$$x_{step} = (x_{int} - x_{sep}) / N_w \quad (a3.13)$$

where N_w is the required number of vortex panels. The x and y values of the panel corner points may then be found from the solution of equations a3.10 - a3.12.

The wake shape is then determined iteratively in the manner described in Chapter 2.

Appendix 4. Calculation of the 'Bubble Panel' Influence Coefficients

To calculate the influence coefficients due to the panel containing the imposed 'bubble' vorticity distribution, it is convenient to divide the panel into four sub-panels, as shown in Fig. A4.

Once the panel has been split in this manner, the influence coefficients for each sub-panel are obtained by the method outlined in Appendix 1. Thus, from equation a1.4 for sub-panel 1, the A and B influence coefficients may be expressed as

$$A_{ib} = \int_0^{L_r} \frac{\gamma_b (L_r - S_b) (\vec{r}_{nib} \cdot \vec{n}_i)}{L_r |r_{ib}|^2} dS_b \quad (a4.1)$$

$$B_{ib} = \int_0^{L_r} \frac{S_b \gamma_r (\vec{r}_{nib} \cdot \vec{n}_i)}{L_r |r_{ib}|^2} dS_b \quad (a4.2)$$

In this way, the influence coefficients for each sub-panel may be evaluated. The total induced velocity due to the separation bubble panel is therefore

$$\vec{V}_{ib} = A_{ib_1} \gamma_b + B_{ib_1} \gamma_r + A_{ib_2} \gamma_r + B_{ib_2} \gamma_t + A_{ib_3} \gamma_t + B_{ib_3} \gamma_s + A_{ib_4} \gamma_s + B_{ib_4} \gamma_{b+1} \quad (a4.3)$$

$$\vec{V}_{ib} = A_{ib_1} \gamma_b + B_{ib_1} \gamma_r + A_{ib_2} \gamma_r + B_{ib_2} \gamma_t + A_{ib_3} \gamma_t + B_{ib_3} \gamma_s + A_{ib_4} \gamma_s + B_{ib_4} \gamma_{b+1} \quad (a4.3)$$

where the number subscripts denote the sub-panels indicated in Fig. A4. To obtain the C influence coefficient of equation a1.11, it is necessary to express the above equation in the form

$$\vec{V}_{ib} = A_{ib} \gamma_b + B_{ib} \gamma_{b+1} \quad (a4.4)$$

Since the original panel vorticity distribution is linear, it is possible to express the vorticity at all points on the panel in terms of the corner point values i.e.

$$\gamma_r = \gamma_b + \left[\frac{\gamma_{b+1} - \gamma_b}{L_b} \right] L_r \quad (a4.5)$$

$$\gamma_t = \gamma_b + \left[\frac{\gamma_{b+1} - \gamma_b}{L_b} \right] L_s \quad (a4.6)$$

$$\gamma_s = \gamma_b + \left[\frac{\gamma_{b+1} - \gamma_b}{L_b} \right] L_s \quad (a4.7)$$

Thus combining equations a4.3-a4.7 the A and B influence coefficients are of the form

$$A_{ib} = A_{ib_1} + B_{ib_1} + A_{ib_2} + B_{ib_2} + A_{ib_3} + B_{ib_3} + A_{ib_4} - Dmat / L_b \quad (a4.8)$$

$$B_{ib} = B_{ib_4} + B_{ib_1} \frac{L_r}{L_b} + A_{ib_2} \frac{L_r}{L_b} + B_{ib_2} \frac{L_s}{L_b} + A_{ib_3} \frac{L_s}{L_b} + B_{ib_3} \frac{L_s}{L_b} + A_{ib_4} \frac{L_s}{L_b} \quad (a.4.9)$$

where

$$Dmat = B_{ib_1} L_r + A_{ib_2} L_r + B_{ib_2} L_s + A_{ib_3} L_s + B_{ib_3} L_s + A_{ib_4} L_s \quad (a4.10)$$

The C influence coefficients may then be obtained by the method outlined in Appendix 1.

Appendix 5. Derivation of the Equations of Le Foll from the Standard Form

For two-dimensional incompressible flow the momentum integral and energy integral equations may be written

$$d(\theta u_e^2) + \delta^* u_e du_e = Cf \frac{u_e^2}{2} ds + d \left[\int_0^\delta (\overline{u'^2} - \overline{v'^2}) dy \right] \quad (a5.1)$$

$$d \left[\frac{u_e^3}{2} \right] = \frac{CD}{2} u_e^3 ds + d \left[\int_0^\delta \frac{\overline{u'^2} + \overline{v'^2} + \overline{w'^2}}{2} dy \right] \quad (a5.2)$$

By defining

$$\theta^* = \theta - \int_0^\delta \frac{\overline{u'^2} - \overline{v'^2}}{u_e^2} dy \quad (a5.3)$$

$$\epsilon^* = \epsilon - \int_0^\delta \frac{u}{u_e} \left[\frac{\overline{u'^2} + \overline{v'^2} + \overline{w'^2}}{u_e^2} \right] dy \quad (a5.4)$$

equations a5.1 and a5.2 may be reduced to

$$2u_e du_e \theta^* + u_e^2 d\theta^* + \delta^* u_e du_e = Cf \frac{u_e^2}{2} ds \quad (a5.5)$$

$$3u_e^2 du_e \epsilon^* + u_e^3 d\epsilon^* = CD u_e^3 ds \quad (a5.6)$$

respectively. These two equations can then be combined to give

$$2 \frac{du_e}{u_e} \theta^* + d\theta^* + \frac{du_e}{u_e} \delta^* = \frac{Cf}{2CD} \left[3 \frac{du_e}{u_e} \epsilon^* + d\epsilon^* \right] \quad (a5.7)$$

which when divided by $\delta^* - \theta^*$ produces

$$\frac{du_e}{u_e} + \frac{1}{H^* - 1} 3 \frac{du_e}{u_e} + \frac{d\theta^*}{\delta^* - \theta^*} = \frac{C_1}{H^* - 1} \frac{He^* Cf}{2CD} \frac{dE}{E} \quad (a5.8)$$

where the deficit of kinetic energy E is given by

$$E = \rho \epsilon^* \frac{u_e^3}{2} \quad (a5.9)$$

and so

$$\frac{dE}{E} = \left[3 \frac{du_e}{u_e} + \frac{d\epsilon^*}{\epsilon^*} \right] \quad (a5.10)$$

and $H^* = \delta^*/\theta^*$, $He^* = \epsilon^*/\theta^*$.

Rearranging equation a5.8 and adding $\frac{d\epsilon^*}{\epsilon^*(H^* - 1)}$ to either side it

is possible to get

$$\frac{1}{H^* - 1} \left[1 - \frac{He^* Cf}{2CD} \right] \frac{dE}{E} + \frac{du_e}{u_e} = \left[\frac{d\epsilon^*}{\epsilon^*} - \frac{d\theta^*}{\theta^*} \right] \frac{1}{H^* - 1} \quad (a5.11)$$

Now, as indicated in chapter 3, the differential of the parameter L is defined as

$$dL = \frac{1}{H^* - 1} \frac{dHe}{He} \quad (a5.12)$$

which, when the influence of the fluctuation terms is introduced via C_1 , may be expressed as

$$C_1 dL = \frac{1}{H^* - 1} \left[\frac{d\epsilon^*}{\epsilon^*} - \frac{d\theta^*}{\theta^*} \right] \quad (a5.13)$$

Further, if the following definitions are applied

$$M = \frac{1}{H - 1} \left[1 - \frac{\text{HeCf}}{2CD} \right] \quad (\text{a5.14})$$

$$C_1 M = \frac{1}{H^* - 1} \left[1 - \frac{\text{He}^* \text{Cf}}{2CD} \right] \quad (\text{a5.15})$$

where the constant C_1 is again used as a first approximation to the effect of the fluctuation terms then, by considering equations a5.13 and a5.15, equation a5.11 may be expressed as

$$C_1 dL = \frac{du_e}{u_e} + C_1 M \frac{dE}{E} \quad (\text{a5.16})$$

To develop the equations of Chapter 3, it is necessary to introduce the following definitions

$$q = \ln \frac{u_e}{U_0} \quad (\text{a5.17})$$

$$\phi = \int_0^s \frac{u_e ds}{v} \quad (\text{a5.18})$$

$$X = \left[\frac{\epsilon u_e}{v} \quad e^{2C_1 L} \right] \quad (\text{a5.19})$$

The differential of equation a5.19 may then be expressed as

$$dX = \frac{d\epsilon}{\epsilon} + \frac{du_e}{u_e} + 2C_1 dL \quad (\text{a5.20})$$

which, from equation a5.16 becomes

$$dX = \frac{d\epsilon}{\epsilon} + 3 \frac{du_e}{u_e} + 2C_1M \frac{dE}{E} \quad (\text{a5.21})$$

By including the relation of equation a5.10 and rearranging, it is possible to get

$$\frac{dE}{E} = \frac{dX}{1 + 2C_1M} \quad (\text{a5.22})$$

Combining this equation with equation a5.16 gives

$$dq = C_1 dL - \frac{C_1 M}{1 + 2C_1 M} dX \quad (\text{a5.23})$$

since

$$dq = \frac{du_e}{u_e} \quad (\text{a5.24})$$

Equation a5.23 is the first of the two governing equations of the boundary layer calculation technique.

To develop the second equation, it is necessary to again consider the energy integral equation as given in equation a5.6. By rearranging this equation it is possible to obtain

$$CD u_e ds = \epsilon^* u_e \left[\frac{3du_e}{u_e} + \frac{d\epsilon^*}{\epsilon^*} \right] \quad (\text{a5.25})$$

which, from equation a5.10, is equivalent to

$$CD u_e ds = \epsilon^* u_e \frac{dE}{E} \quad (\text{a5.26})$$

By rearranging equation a5.26 and dividing each side by the kinematic viscosity ν , the following equation may be obtained.

$$\frac{u_e ds}{\nu} = \frac{dE}{E} \left[\frac{\epsilon^* u_e}{\nu CD} \right] \quad (\text{a5.27})$$

which is equivalent to

$$\frac{u_e ds}{\nu} = \frac{dE}{E} \left[\frac{\frac{\epsilon^* u_e}{\nu} e^{2C_1 L}}{CD e^{2C_1 L}} \right] \quad (\text{a5.28})$$

From equation a5.18

$$d\phi = \frac{u_e ds}{\nu} \quad (\text{a5.29})$$

and from equation a5.20

$$e^X = \left[\frac{\epsilon u_e}{\nu} e^{2C_1 L} \right] \quad (\text{a5.30})$$

The above two relations, along with equation a5.10, permit equation a5.28 to be expressed as

$$d\phi = \frac{e^X dX}{(1 + 2C_1 M) C D e^{2C_1 L}} \quad (\text{a5.31})$$

which is the second governing equation of the boundary layer method.

Appendix 6. Horton's Separation Bubble Growth Prediction Method

To derive the method for the growth and bursting of laminar separation bubbles it is first necessary to consider the momentum and energy integral equations in the form

$$\frac{d\theta}{ds} + (H + 2) \frac{\theta}{u_e} \frac{du_e}{ds} = \frac{C_f}{2} \quad (\text{a6.1})$$

$$\frac{d\epsilon}{ds} + 3 \frac{\epsilon}{u_e} \frac{du_e}{ds} = CD \quad (\text{a6.2})$$

From these equations, it is possible to develop the required equations by splitting the separated shear layer into two sections i.e. laminar and turbulent.

LAMINAR PART

From experiment, Horton observed that the laminar portion of a separation bubble had a virtually constant pressure and so from equation a6.1

$$\theta_t = \theta_s \quad (\text{a6.3})$$

where the subscripts t and s refer to transition and separation respectively.

By examination of available experimental data, Horton found that the length of the laminar shear layer was given approximately by

$$\frac{l_t}{\theta_s} = \frac{4 \times 10^4}{R_{\theta s}} \quad (\text{a6.4})$$

TURBULENT PART

By introducing the energy form parameter and combining equations a6.1 and a6.2 it is possible to obtain

$$\theta \frac{dHe}{ds} = (H - 1) He \frac{\theta}{u_e} \frac{du_e}{ds} + CD - \frac{1}{2} He Cf \quad (a6.5)$$

By now considering the behaviour of this equation at reattachment where, by definition, the skin friction is zero, then

$$He (H - 1) \frac{\theta}{u_e} \frac{du_e}{ds} = \theta \frac{dHe}{ds} - CD \quad (a6.6)$$

Since, for high values of H, He is almost independent of H and dHe/dx passes through a minimum near reattachment, it is possible to reduce equation a6.6 to the form

$$\frac{\theta}{u_e} \frac{du_e}{ds} = - \frac{CD}{He (H - 1)} \quad (a6.7)$$

By introducing the concept of universal velocity and shear stress profiles at the point of reattachment, it follows that the term

$$\left[\frac{\theta}{u_e} \frac{du_e}{ds} \right]_R$$

is a function of Reynolds number only.

Horton then obtained a universal velocity profile by consideration of empirical data, for which $H = 3.5$ and $He = 1.51$. By considering this profile with the assumption of constant eddy viscosity Horton obtained

$$\left[\frac{\theta}{u_e} \frac{du_e}{ds} \right]_R = -0.0059 \quad (\text{a6.8})$$

This value, however was derived for an attached boundary layer and as such may be expected to be too small since the entrainment rate and dissipation coefficient would be higher for a reattaching layer. To alleviate this problem, Horton adopted a mean experimental value of

$$\Lambda_R = \left[\frac{\theta}{u_e} \frac{du_e}{ds} \right]_R = -0.0082 \quad (\text{a6.9})$$

which was used in the subsequent development of the reattachment criterion.

Now integrating equation a6.2 between transition and reattachment

$$\left[He \theta u_e^3 \right]_T^R = \int_T^R CD u_e ds \quad (\text{a6.10})$$

By adopting a mean value of $He = 1.50$ for the turbulent shear layer and by introducing the following non-dimensionalised terms

$$\bar{u}_e = \frac{u_e}{u_{es}} = \frac{u_e}{u_{et}}, \quad \bar{\theta} = \frac{\theta}{\theta_s} = \frac{\theta}{\theta_t}, \quad \bar{s} = \frac{s}{\theta_s} \quad (\text{a6.11})$$

it is possible to obtain

$$\bar{\theta}_R \bar{u}_{eR}^3 = \frac{1}{He_m} \int_{\bar{s}_T}^{\bar{s}_R} CD \bar{u}_e (\bar{s}) d\bar{s} \quad (\text{a6.12})$$

where

$$\bar{u}_e = \frac{u_{eR}}{u_{eT}} = \frac{u_{eR}}{u_{eS}} \quad (\text{a6.13})$$

The contribution of the right-hand side of this equation is not usually large, thus allowing a constant overall dissipation coefficient cd_m to be adopted.

Assuming a linear external velocity distribution over the turbulent part of the bubble it is possible to get, in non-dimensional form,

$$\left[\frac{d\bar{u}_e}{d\bar{s}} \right] = - \frac{(1 - \bar{u}_{eR})}{\bar{l}_2} \quad (\text{a6.14})$$

where $\bar{l}_2 = l_2/\theta_s$. This equation may be combined with the non-dimensional form of equation a6.9 to give

$$\bar{\theta}_R = -\Lambda_R \frac{\bar{u}_{eR} \bar{l}_2}{(1 - \bar{u}_{eR})} \quad (\text{a6.15})$$

The linear external velocity may be expressed as

$$\bar{u}_e = 1 - (1 - \bar{u}_{eR}) \left[\frac{\bar{s} - \bar{l}_1}{\bar{l}_2} \right] \quad (\text{a6.16})$$

which upon substitution into equation a6.12 gives

$$\theta_R = \frac{1}{\bar{u}_{eR}^3} + \frac{CD_m/He_m}{\bar{u}_{eR}^3} \int_{l_t}^{\bar{l}_t + \bar{l}_2} \left[1 - (1 - u_e) \left[\frac{s - l_t}{\bar{l}_2} \right] \right] dx \quad (\text{a6.17})$$

On integration the above equation yields

$$\bar{\theta} = \frac{1}{\bar{u}_{eR}^3} + \frac{CD_m}{4He_m} \frac{\bar{l}_2 (1 - \bar{u}_{eR}^4)}{\bar{u}_{eR}^3 (1 - \bar{u}_{eR})} \quad (a6.18)$$

which when combined with equation a6.15 produces the required equation

$$\bar{u}_{eR}^4 = \frac{\frac{CD_m}{4He_m} + \frac{(1 - \bar{u}_{eR})}{\bar{l}_2}}{\frac{CD_m}{4He_m} - \Lambda_R} \quad (a6.19)$$

REFERENCES

1. Mueller, T.J., 'Low Reynolds Number Vehicles', AGARDograph No. 288, (February 1985).
2. Galbraith, R.A.McD., Coton, F.N., Saliveros, E., Kokkodis, G., 'Aerofoil Scale Effects and the Relevance to Wind Turbines', Ninth Annual Wind Energy Conference, Edinburgh, (1987)
3. Lissaman, P.B.S., 'Low Reynolds Number Airfoils', Annual Review of Fluid Mechanics, Vol.15, pp.223-239, (1983).
4. Marchman, J. F., 'Aerodynamic Testing at Low Reynolds Numbers', Journal of Aircraft, Volume 24, No. 2, February (1987).
5. Carmichael, B.H., 'Low Reynolds Number Airfoil Survey', Vol. I, NACA CR 165803, November (1981).
6. Mueller, T.J., Pohlen, L.J., Conigliaro, P.E., Jansen, B.T., 'The Influence of Freestream Disturbances on Low Reynolds Number Aerofoil Experiments', Experiments in Fluids, Vol.1, pp.3-14, (Springer-Verlag 1983).
7. McMasters, J.H., Henderson, M.L., 'Low-Speed Single Element Airfoil Synthesis', Technical Soaring, Vol. 6, No. 2, pp.1-21, (1979).

8. Blascovich, J.D., 'A Comparison of Separated Flow Airfoil Analysis Methods', Journal of Aircraft, Vol. 22, No. 3, (1984).
9. Liebeck, R.H., 'Design of Subsonic Airfoils for High Lift', Journal of Aircraft, Vol 15,
- 10 Schlichting, H., 'An Account of the Scientific Life of Ludweig Prandtl', - Memorial Lecture, AGARD C.P. 168, (1975).
11. Jacobs, E.N., Sherman, A., 'Airfoil Section Characteristics as Affected by Variations of the Reynolds Number', NACA Technical Report No. 586, (1937).
12. Schmitz, F.W., 'Aerodynamics of the Model Airplane, Part I, Airfoil Measurements', NASA-TM-X-60976, Nov. 1967, pp. 201 (originally published in Germany 1941)
13. McCullough, G.B., Gault, D.E., 'Examples of Three Representative Types of Airfoil-Section Stall at Low-Speed', NACA TN 2502, (1951).
14. Gault, D.E., 'An Experimental Investigation of Regions of Separated Laminar Flow', NACA TN 3505, (1955).
15. Gaster, M., 'The structure and Behaviour of Laminar Separation Bubbles', A.R.C. R & M. No. 3595, (1969).

16. Horton, H.P., 'A Semi-Empirical Theory for the Growth and Bursting of Laminar Separation Bubbles', ARC. C.P. No. 1073, (1969)
17. Gleyzes, C., Cousteix, J., Bonnet, J.L., 'A Calculation Method of Leading Edge Separation Bubbles', Numerical and Physical Aspects of Aerodynamic Flows, Vol. II, (1984).
18. Ward, J.M., 'Behaviour and Effects of Laminar Separation Bubbles on Aerofoils in Incompressible Flow', Journal of the Royal Aero. Society, Vol. 67, pp783-790, (1963).
19. Goldstein, S., 'Modern Developments in Fluid Dynamics', Volume II, University Press, Oxford, 1938
20. Mueller, T.J., Batill, S.M., 'Experimental Studies of Separation on a Two-Dimensional Airfoil at Low Reynolds Numbers', AIAA Journal, Vol. 20, No. 4, April (1982).
21. Leishman J.G., Galbraith, R.A.McD., Hanna, J., 'Modelling of Trailing Edge Separation on Arbitrary Two-Dimensional Aerofoils in Incompressible Flow Using an Inviscid Flow Algorithm', Glasgow University Aero. Report No. 8202 (1982)
22. Maskew, B., Dvorak, F.A., 'Investigation of Separation Models for the Prediction of C_L max', American Helicopter Society Paper 77-33-01, (May 1977)

23. Williams, B.R., 'The Calculation of Flow about Aerofoils at Low Reynolds Number with Application to Remotely Piloted Vehicles', International Conference on Aerodynamics at Low Reynolds Numbers ($10^4 < \text{Re} < 10^6$), London, (1986)
24. Cebeci, T., Wang, G.S., Chang, K.C., Choi, J., 'Recent Developments in the Calculation of Flow Over Low Reynolds No. Aerofoils', International Conference on Aerodynamics At Low Reynolds Numbers ($10^4 < \text{Re} < 10^6$), London, October (1986).
25. Preston, J.H., 'The calculation of lift taking account of the boundary layer', A.R.C. R&M No. 2725, (1953)
26. Leishman, J.G., Galbraith, R.A.McD., 'An Algorithm for the Calculation of the Potential Flow about an Arbitrary Two-Dimensional Aerofoil', Glasgow University Aero. Report No. 8102 (1981)
27. Hanna, J., 'Modelling of Trailing Edge Separation of an Aerofoil by Inviscid Flow Calculations', Glasgow Univ. Final Year Project Report, Glasgow, (1982)
28. Maskew, B., Dvorak, F.A., 'The Prediction of C_{Lmax} Using a Separated Flow Model', Journal of the American Helicopter Society, (1978)
29. Galbraith, R.A.McD., 'The Aerodynamic Characteristics of a GU25-5(11)8 Aerofoil for Low Reynolds Numbers', Glasgow University Report No. 8410 (1984)

30. Roberts, W.B., 'Calculation of Laminar Separation Bubbles and Their Effect on Airfoil Performance', AIAA Journal, Vol. 18, No. 1, (JAN 1980)
31. Schlichting, H., 'Boundary Layer Theory', 7th Edition, McGraw Hill Book Company, New York, (1979)
32. Le Foll, J., 'A Theory of Representation of the Properties of Boundary Layers on a Plane', Proc. Seminar on Advanced Problems in Turbomachinery, V.K.I., (1965)
33. Assassa, G.M., Papailiou, K.D., 'An Integral Method for Calculating Turbulent Boundary Layer with Separation', Transactions of the ASME, Vol. 100, pp.110-116 (1979)
34. Head, M.R., 'An Approximate Method for Calculating the Laminar Boundary Layer in Two-Dimensional Incompressible Flow', ARC. R & M No. 3123, (1959)
35. Curle, N., 'The Laminar Boundary Layer Equations', Oxford Clarendon Press, Oxford, (1962)
36. Curle, N., Skan, S.W., 'Approximate Methods for Predicting Separation Properties of Laminar Boundary Layers', Aeronautical Quarterly, (1957).

37. Coles, D., 'The Law of the Wake in the Turbulent Boundary Layer',
C.I.T. Report, (1955)
38. Kuhn, G.D., Neilsen, J.N., 'Prediction of Turbulent Separated
Boundary Layers', AIAA Journal, Vol. 12, No. 7, pp.881-882, (1974)
39. Chu, J., Young, A.D., 'Measurements in Two-Dimensional Turbulent
Boundary Layers', AGARD C.P. No 168, (1975).
40. Galbraith, R.A.McD., 'The prediction of Turbulent Boundary Layers',
Glasgow University Aero. Report No. 7702, (1977)
41. Cebeci, T., Smith, A.M.O., 'Analysis of Turbulent Boundary Layers',
Applied Mathematics and Mechanics, Vol. 15, Academic Press, London,
(1974)
42. Van Ingen, J.L., 'On The Calculation of Laminar Separation Bubbles In
Two-Dimensional Incompressible Flow', AGARD C.P. 168, (1975)
43. Kokkodis, G., 'Low Reynolds Number Performance of a NACA 0015 and
GA(W)-1 Aerofoils', M.Sc. Thesis, Glasgow University, (1987)
44. Coton, F.N., Galbraith, R.A.McD., 'A Simple Method For The Prediction
of Separation Bubble Formation on Aerofoils at Low Reynolds Number',
International Conference on Aerodynamics at Low Reynolds Numbers
($10^4 < Re < 10^6$), London, (1986)

45. Spalding, D. Private communication to authors. Glasgow University Final Year Project, (1985).
46. Brown, S.N., Stewartson, K., 'Laminar Separation', Annual Review of Fluid Mechanics, Vol. 1, Palo Alto, Calif., Annual Review Inc., (1969)
47. Davis, R.L. et al., 'ALESEP: A Computer Program for the Analysis of Airfoil Leading Edge Separation Bubbles', NASA-CR-172310, (1984)
48. Thwaites, B., 'The Development of Laminar Boundary Layers under Conditions of Continuous Suction', (part II), A.R.C. 12,699 (1949)
49. Stewartson, K., 'Further Solutions of the Falkner-Skan Equation', Proc. Cambr. Phil. Soc., Vol. 50, (1954)
50. Coton, F.N., Galbraith, R.A.McD., 'A Direct Viscid-Inviscid Interaction Scheme for the Prediction of Two-Dimensional Aerofoil Performance in Incompressible Flow', Glasgow University Aero. Report No. 8701 (1987)
51. Miley, S.J., 'A Catalog of Low Reynolds Number Airfoil Data for Wind Turbine Applications', Aerospace Engineering Dept., Texas A & M University, (1982)
52. McGhee, R.J., Beasley, W.D., 'Low-Speed Aerodynamic Characteristics of a 17-Percent-Thick Airfoil Section Designed for General Aviation Applications', NASA TN D-7428, (1973)

53. Ladson, C.L., Brooks Jr., C.W., 'Development of a Computer Program to Obtain Ordinates for NACA 4-Digit, 4-Digit Modified, 5-Digit, and 16-Series Airfoils', NASA TM X-3284, (1975)

54. Kelling, F.H., 'Experimental Investigation of a High-Lift Low-Drag Aerofoil', Glasgow University Report No. 6802, (1968)

55. Render, P.M., 'The Experimental and Theoretical Aerodynamic Characteristics of Aerofoil Sections Suitable for Remotely Piloted Vehicles', CoA Report No. 8419, (1984)

Velocity Distribution U/U ₀	Calculation Technique			Exact/ Series
	Thwaites	Stratford	Head	
$(1 + x)^1$	0.147	0.150	0.158	0.159
$(1 + x)^2$	0.069	0.071	0.076	0.078
$(1 - x)^2$	0.061	0.063	0.067	0.067
$(1 - x)^{0.5}$	0.209	0.218	0.220	0.223
cos(x)	0.370	0.387	0.395	0.410
sin(x)	1.786	1.827	1.880	1.902
1 - x	0.116	0.120	0.125	0.120
1 - x ²	0.259	0.271	0.276	0.271
1 - x ³	0.363	0.381	0.400	0.401
1 - x ⁴	0.440	0.462	0.472	0.462

TABLE 1 : Comparison of separation predictions of the methods of Head, Stratford and Thwaites for a number of series/exact cases.

Velocity Distribution U/U ₀	Calculation Technique		Series/ Exact
	Head	Present Method	
$(1 + x)^{-1}$	0.158	0.160	0.159
$(1 + x)^{-2}$	0.076	0.074	0.078
$(1 - x)^2$	0.067	0.067	0.067
$(1 - x)^{0.5}$	0.220	0.224	0.223
cos(x)	0.395	0.407	0.410
sin(x)	1.880	1.896	1.902
1 - x	0.125	0.124	0.120
1 - x ²	0.276	0.280	0.271
1 - x ³	0.400	0.398	0.401
1 - x ⁴	0.472	0.476	0.462

TABLE 2 : Comparison of the separation predictions obtained via the present method with that of Head for a number of series/exact cases.

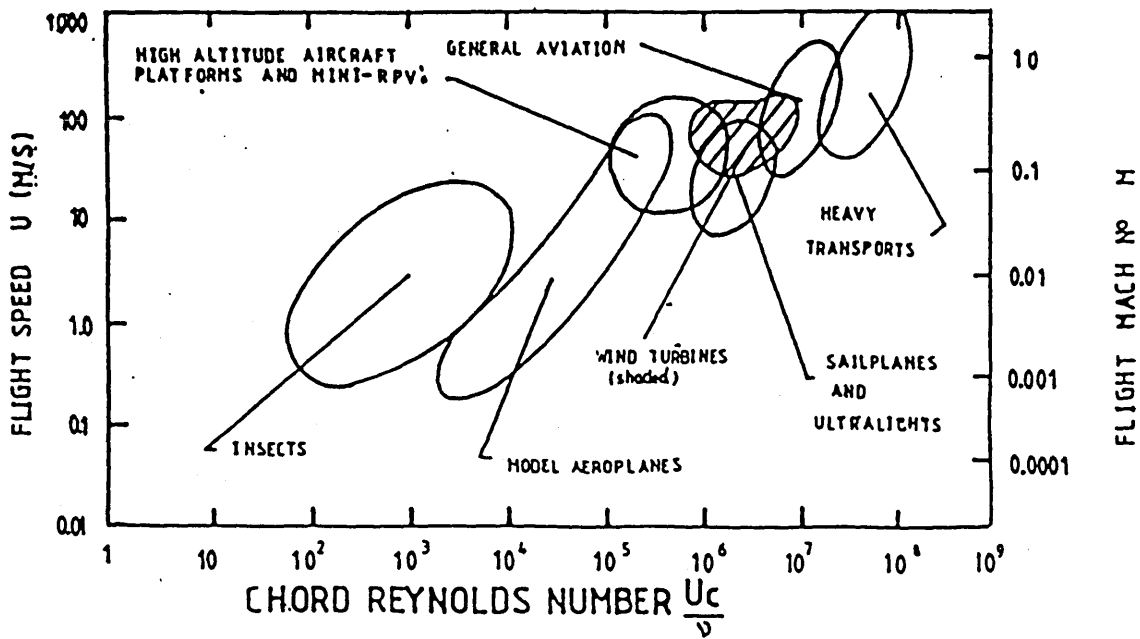


Fig. 1.1 Chord Reynolds Number vs flight velocity for a variety of natural and man-made objects. (Adapted from Ref. 1.)

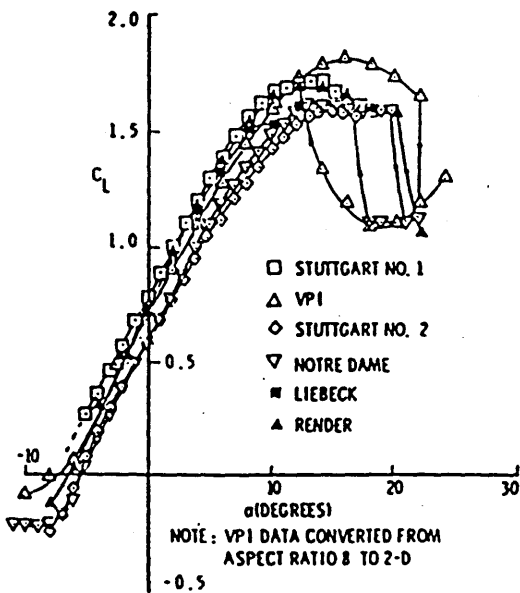


Fig. 1.2 Comparison of experimentally obtained lift curves for the FX63-137 aerofoil. (Taken from Ref. 4.)

Decreasing
Reynolds
Number

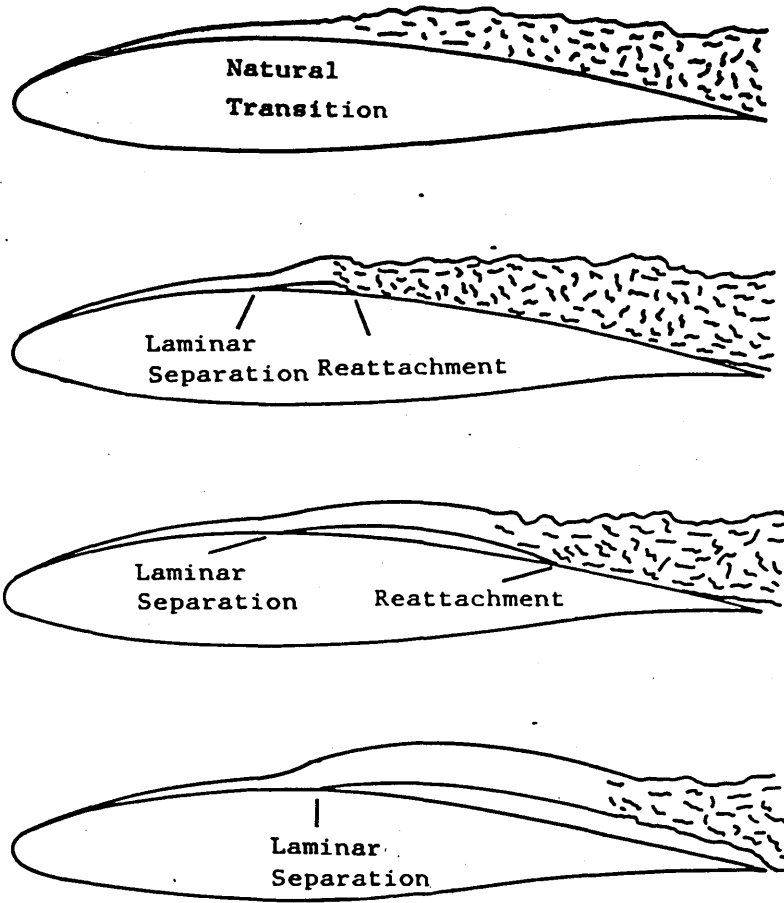


Fig. 1.3 Upper surface boundary layer behaviour with
reducing Reynolds number.

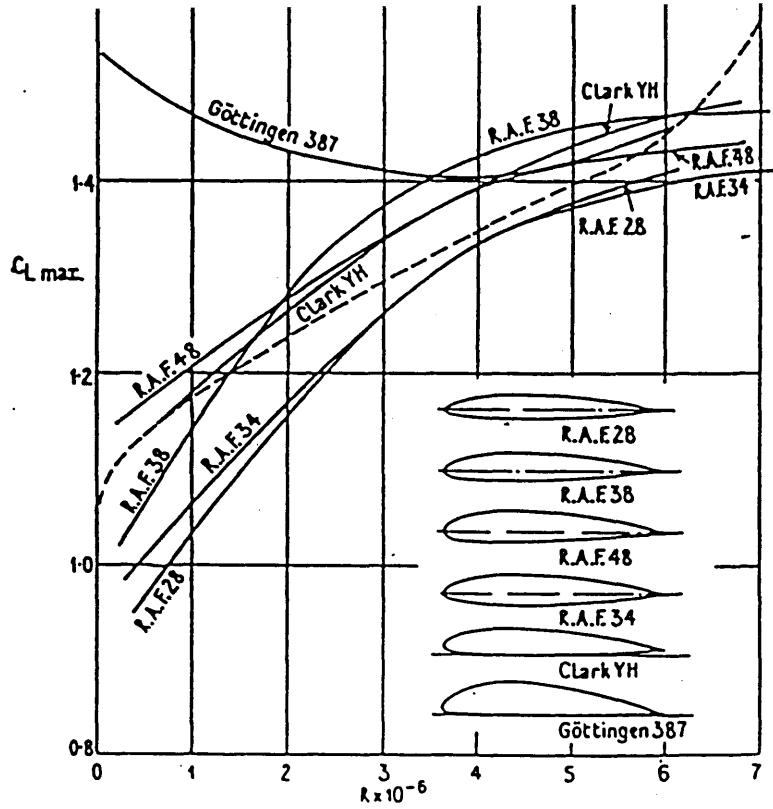


Fig. 1.4 Variation of C_{Lmax} with Reynolds number for six aerofoil sections. (Taken from Ref. 2.)

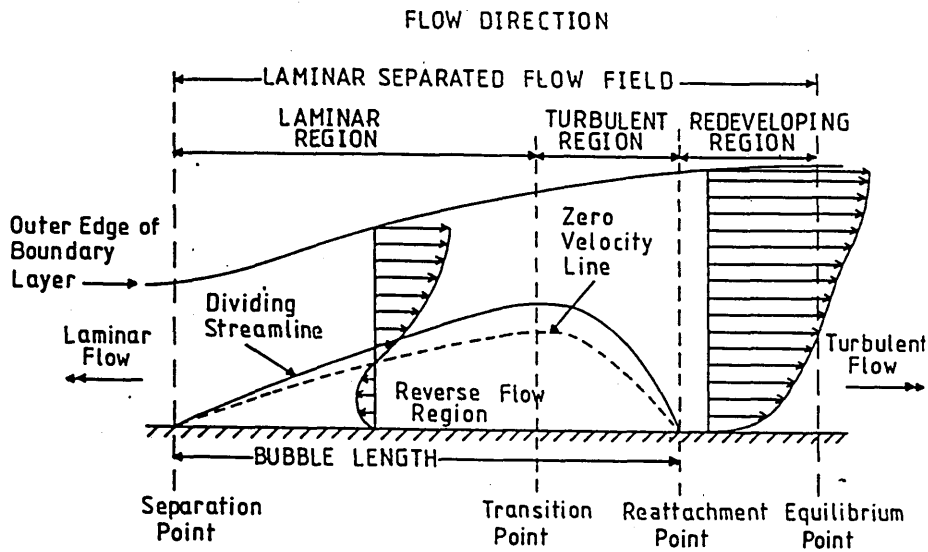


Fig. 1.5 Structure of a laminar separation bubble (Adapted from Ref. 5.).

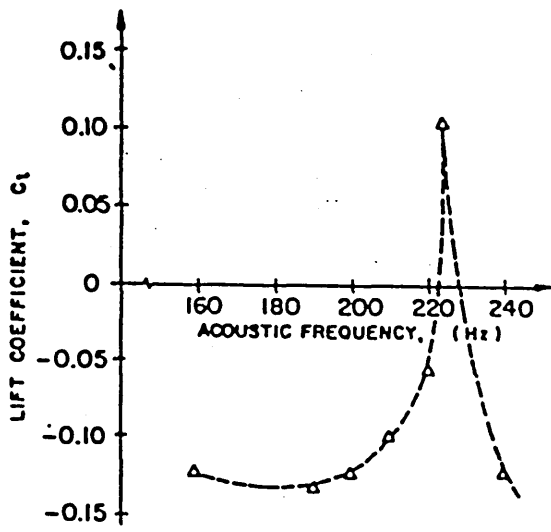


Fig. 1.6 Lift coefficient vs acoustic frequency for one degree of incidence at $Re=130000$ for the NACA 66,-018 aerofoil. (Taken from Ref. 20.)

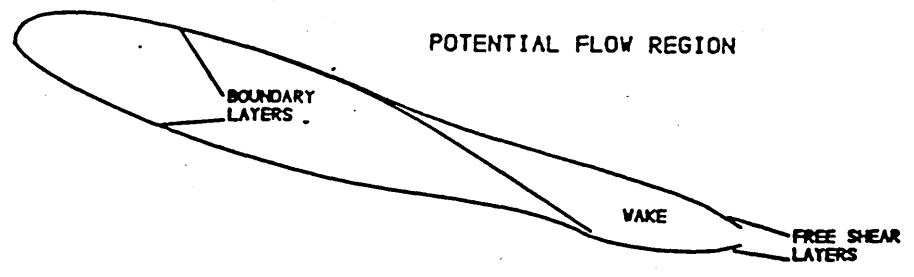


Fig. 1.7 Regions of flow for modelling purposes.

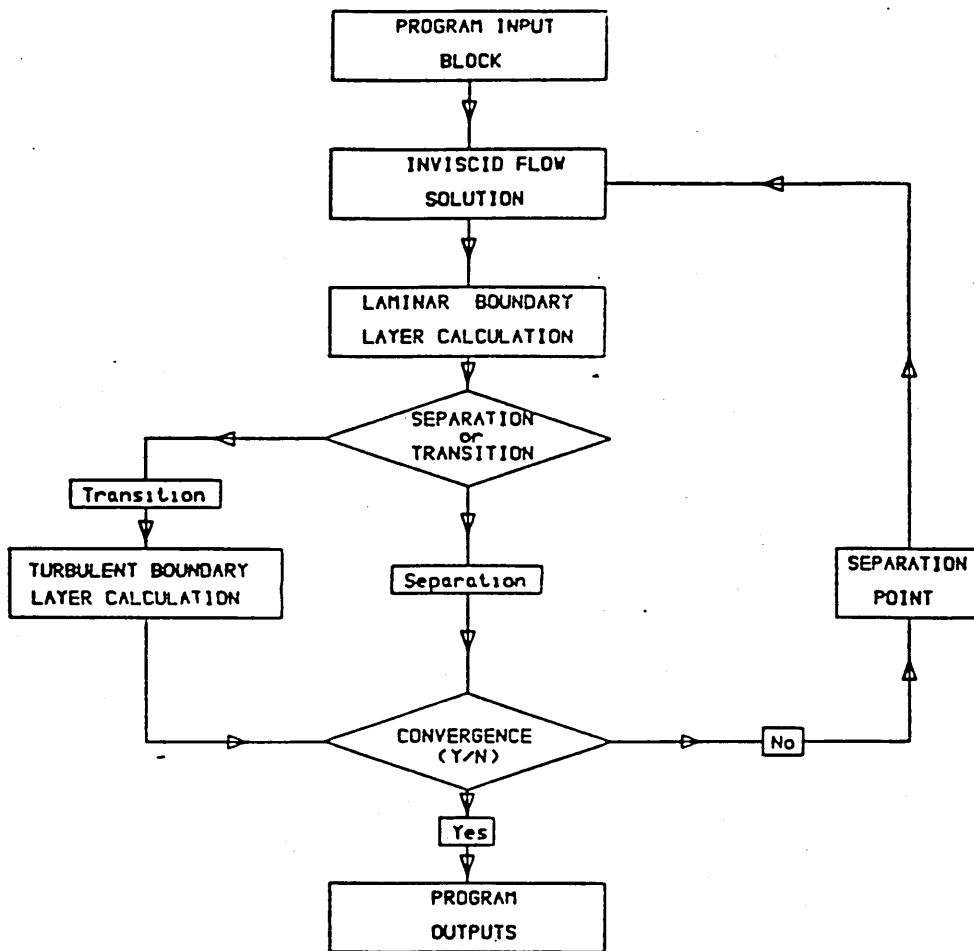


Fig. 1.8 Analysis program flow chart.

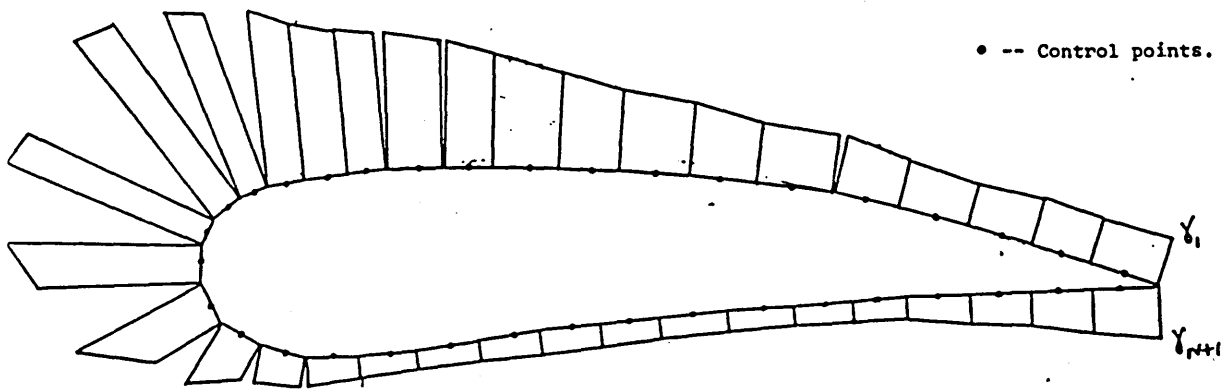


Fig. 2.1 Aerofoil Vortex Panel Distribution for Fully Attached Flow

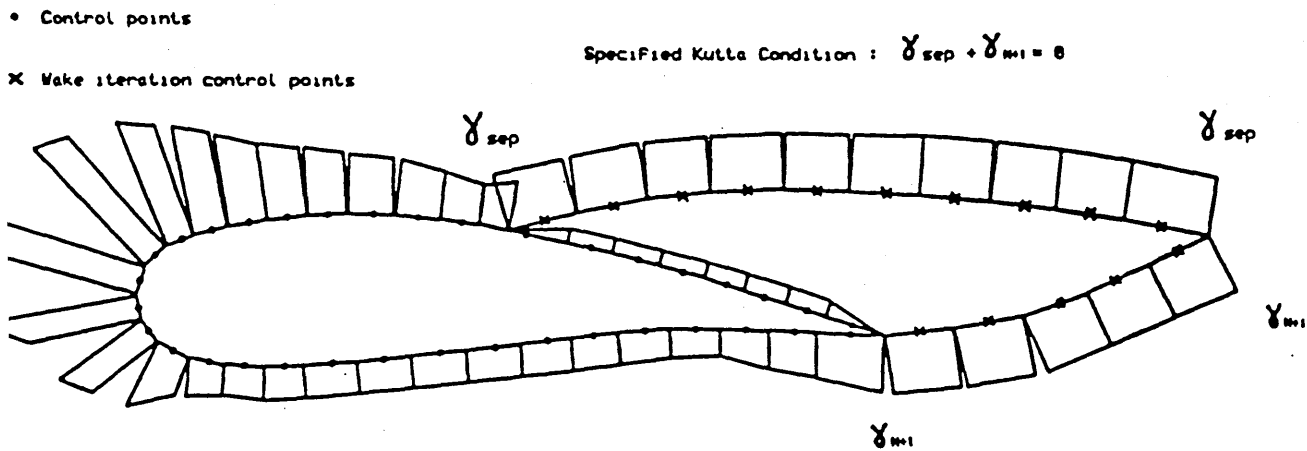


Fig. 2.2 Aerofoil Vortex Panel Distribution for Separated Flow

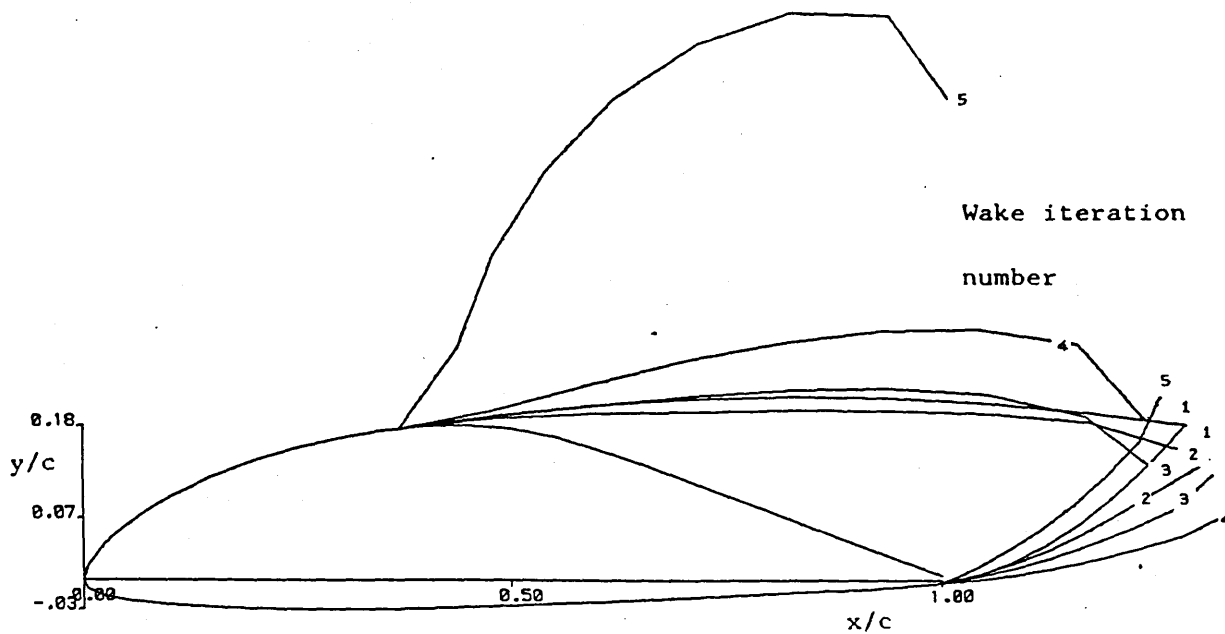


Fig. 2.3 Shear Layer Development During Divergent
Wake Calculation

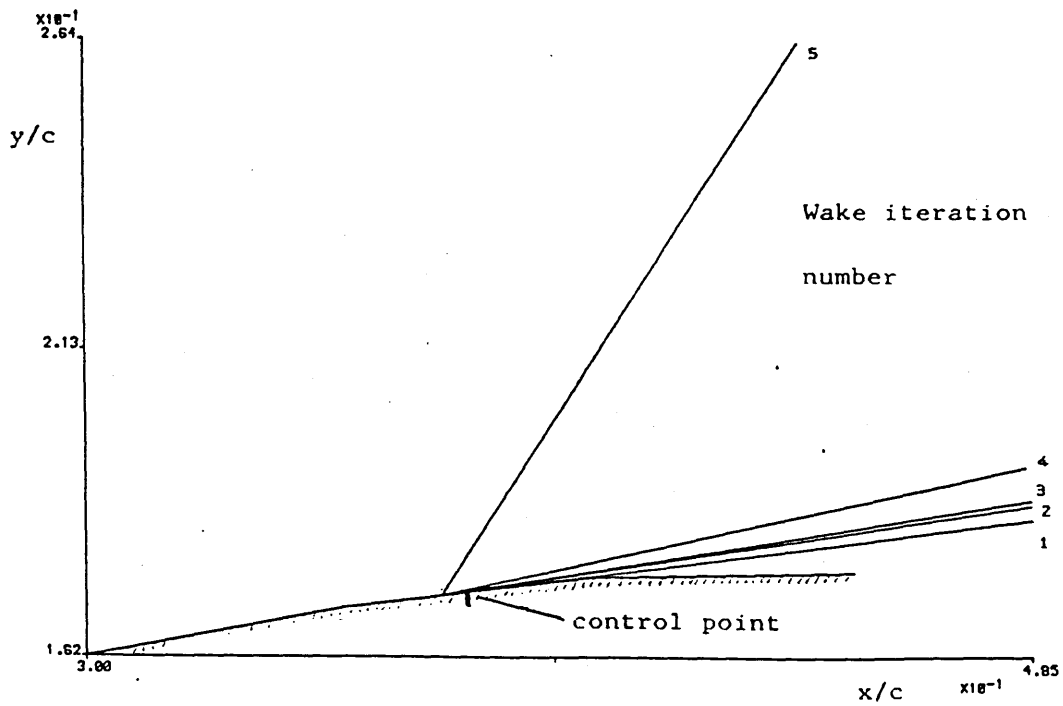


Fig. 2.4 Proximity of Shear Layer To Upper Separation
Panel Control Point During Divergent Calculation

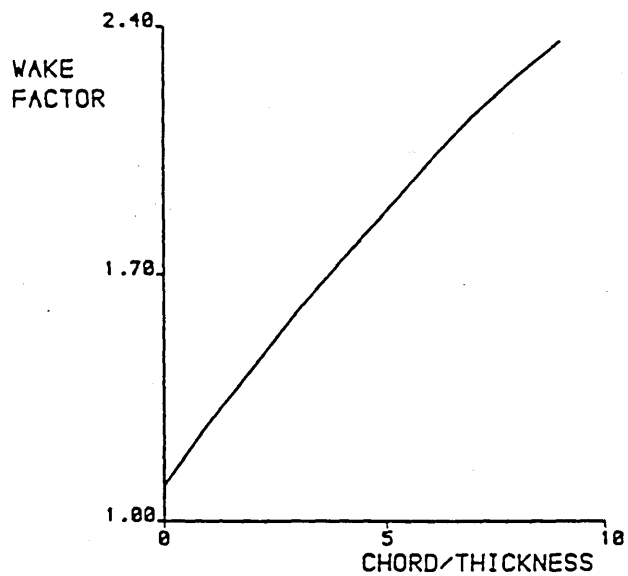


Fig. 2.5 Wake Factor Correlation due to Dvorak and Maskew

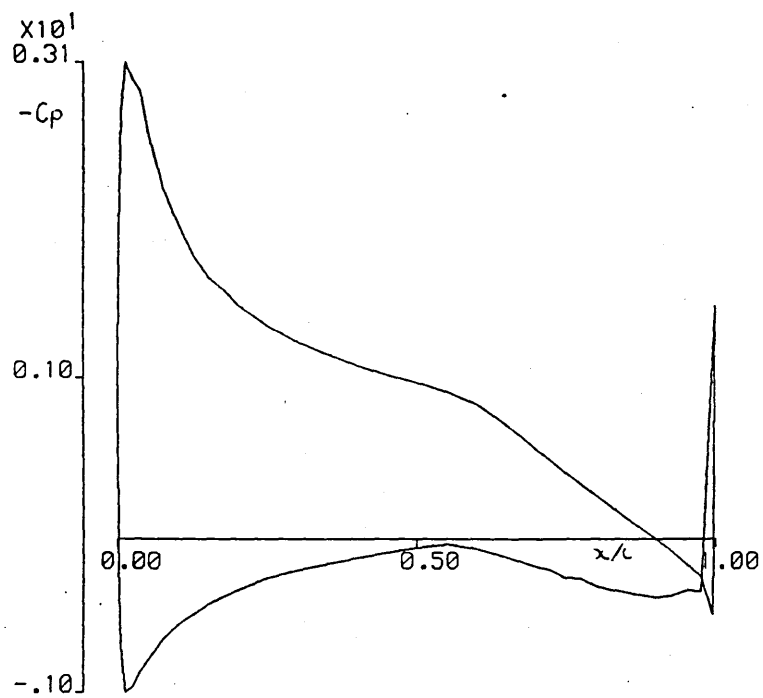


Fig. 2.6 Pressure Distribution Resulting from Distorted Trailing Edge

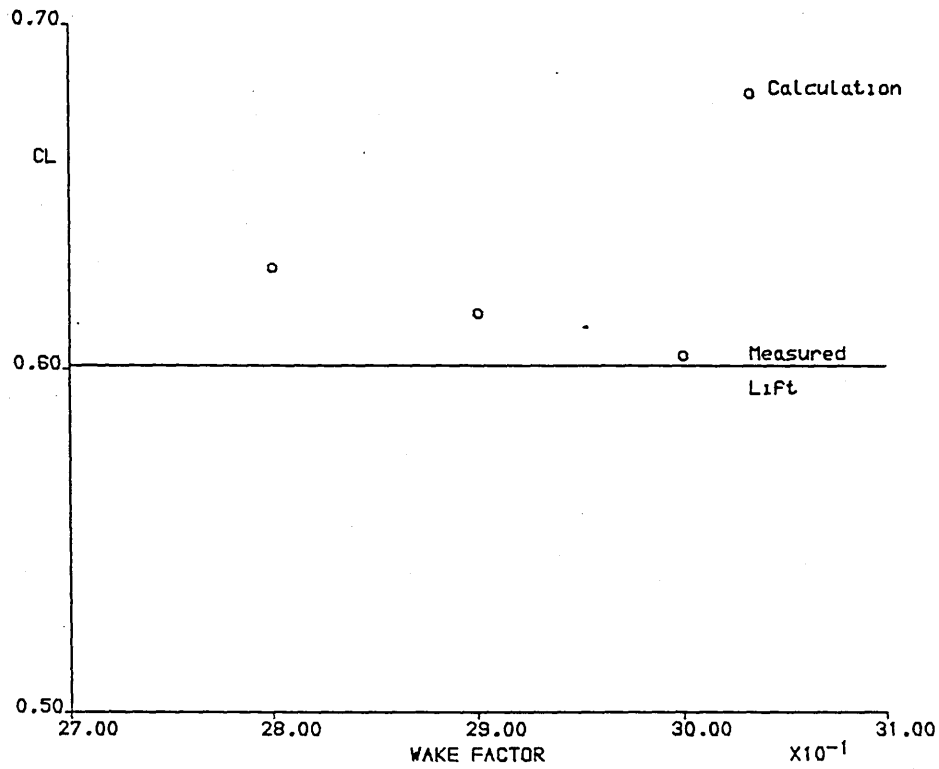


Fig.2.7 Effect of Wake Factor on Lift Calculation of the GU25-5(11)8 Aerofoil at 12.6 degs.
 $R_c = 100000$

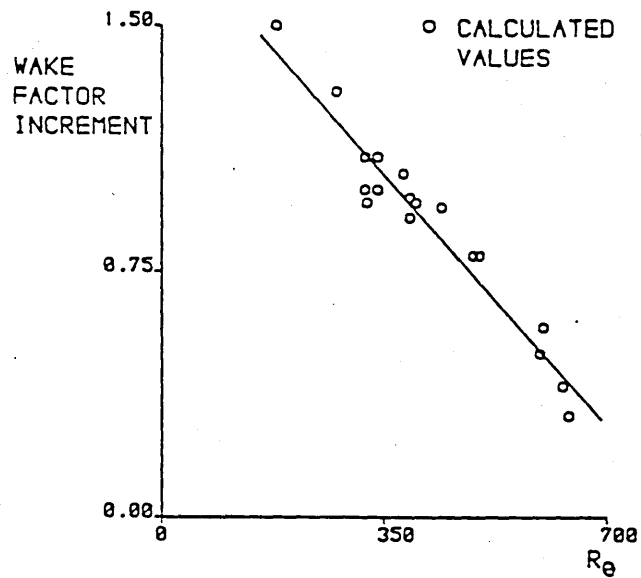


Fig. 2.8 Developed Wake Factor Increment Correlation

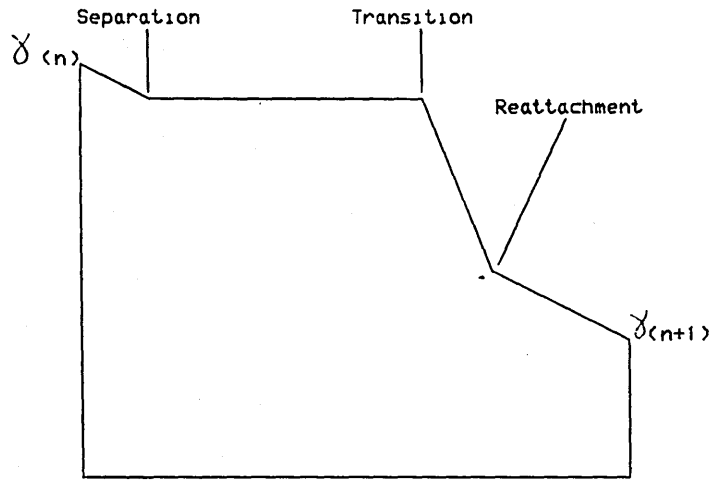


Fig. 2.9 Vorticity Distribution Imposed on
'Bubble' Panel

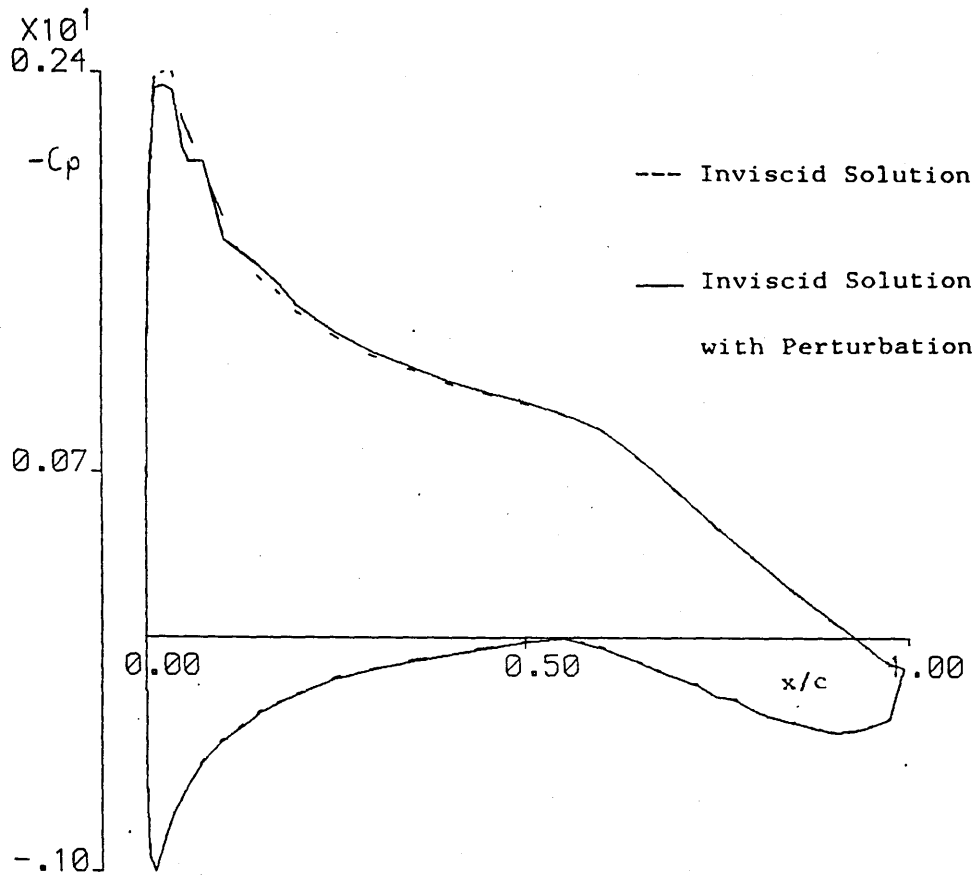
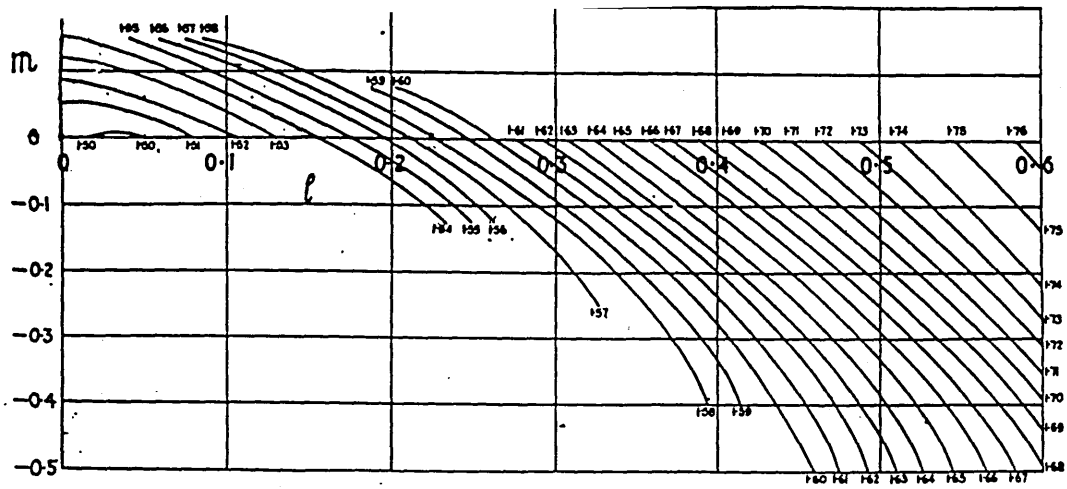
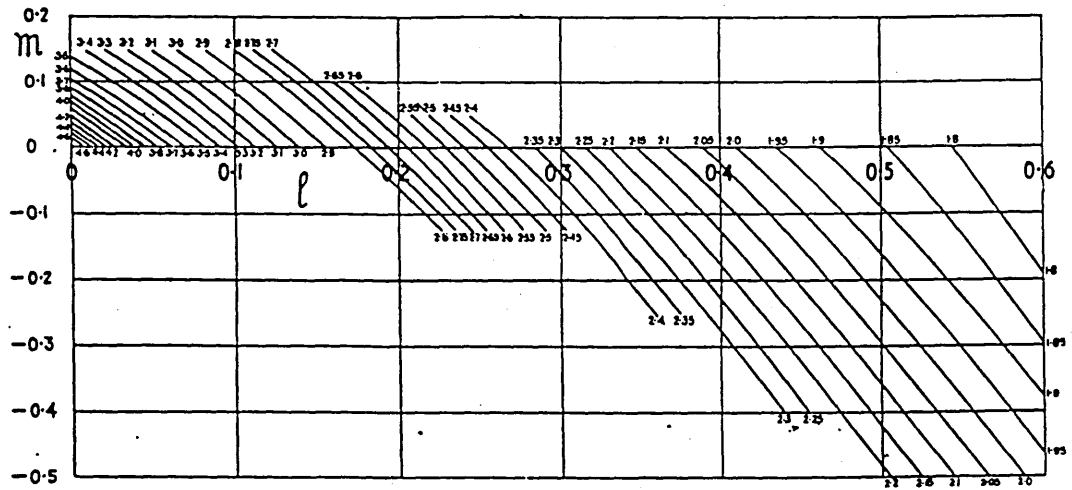


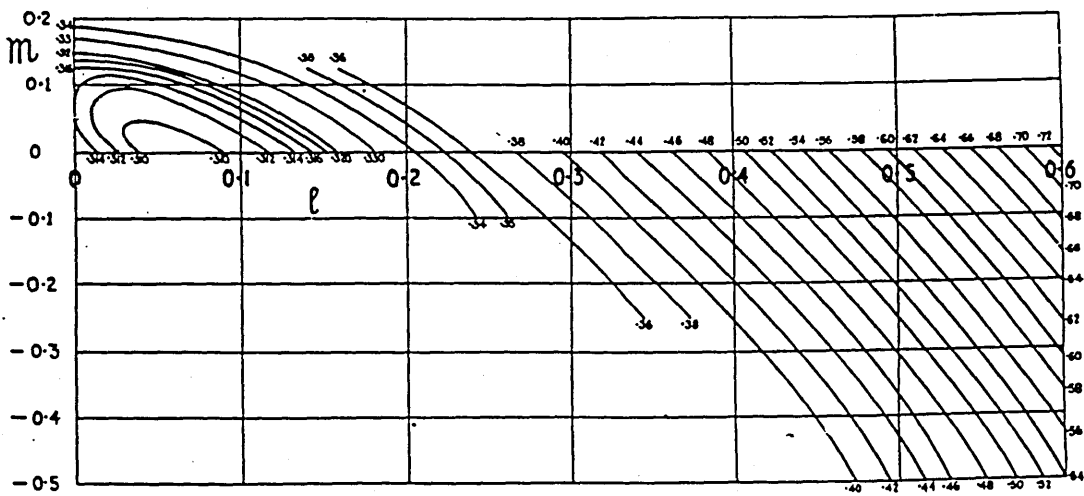
Fig. 2.10 Pressure Distribution With and Without Bubble



Contours of He versus l and m



Contours of H versus l and m



Contours of $2D^*$ versus l and m

Fig. 3.1 Boundary layer parameter charts developed by Head.

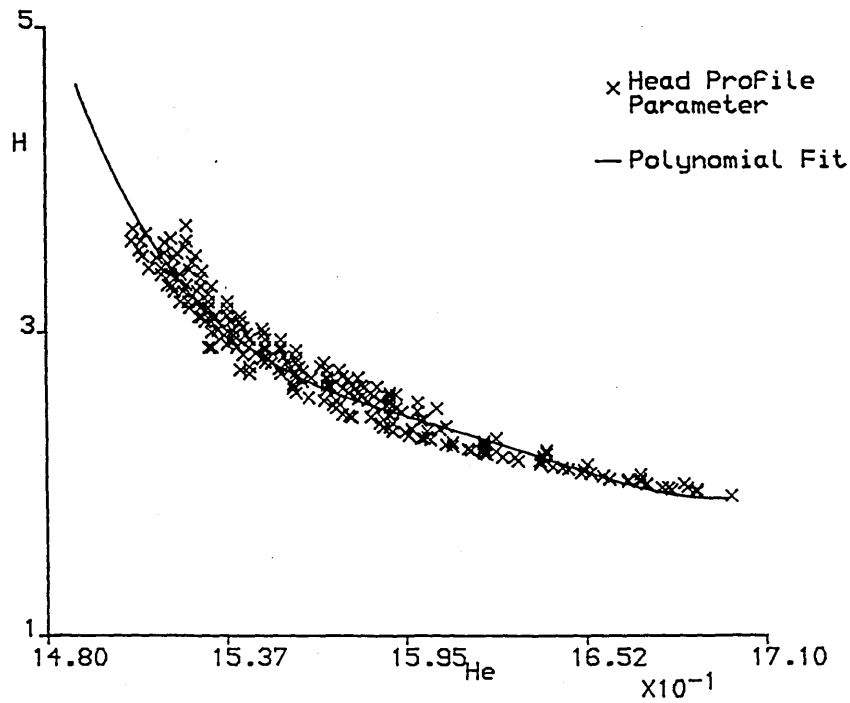


Fig. 3.2 Relation between H and He developed from the profile parameter data of Head.

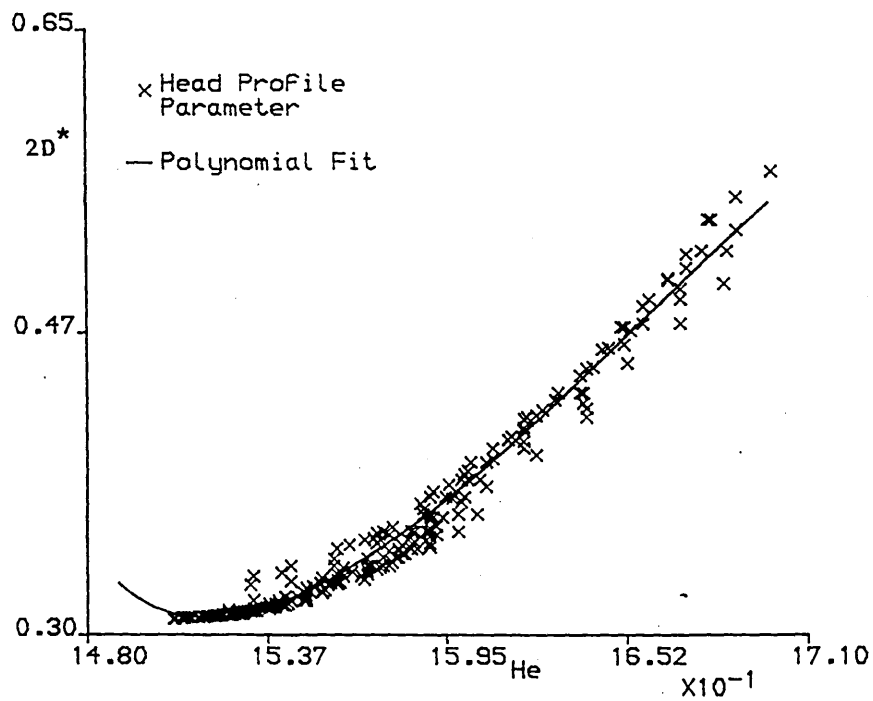


Fig. 3.3 Relation between $2D^*$ and He developed from the profile parameter data of Head.

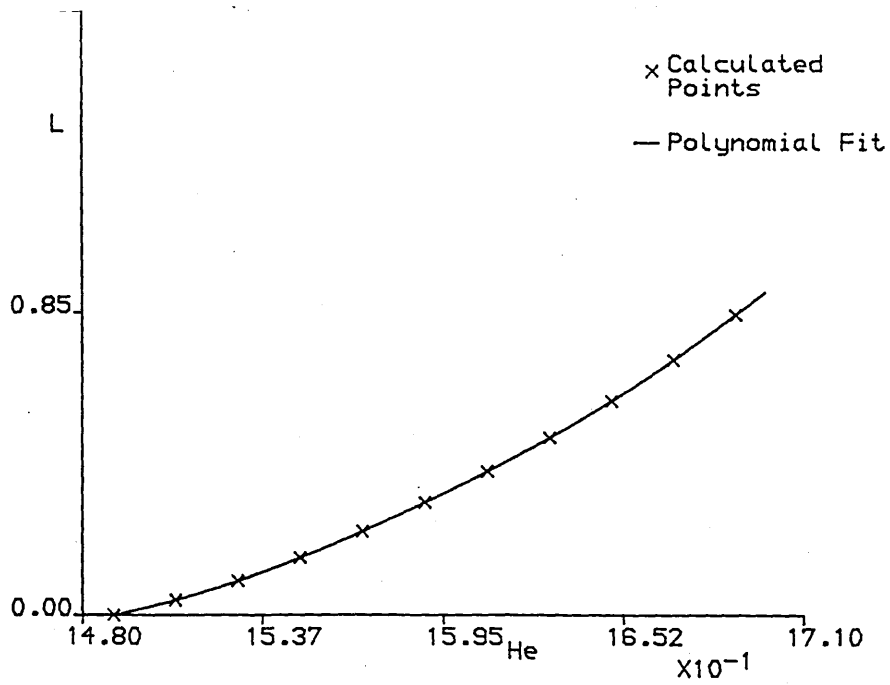


Fig. 3.4 Calculated relationship between He and L.

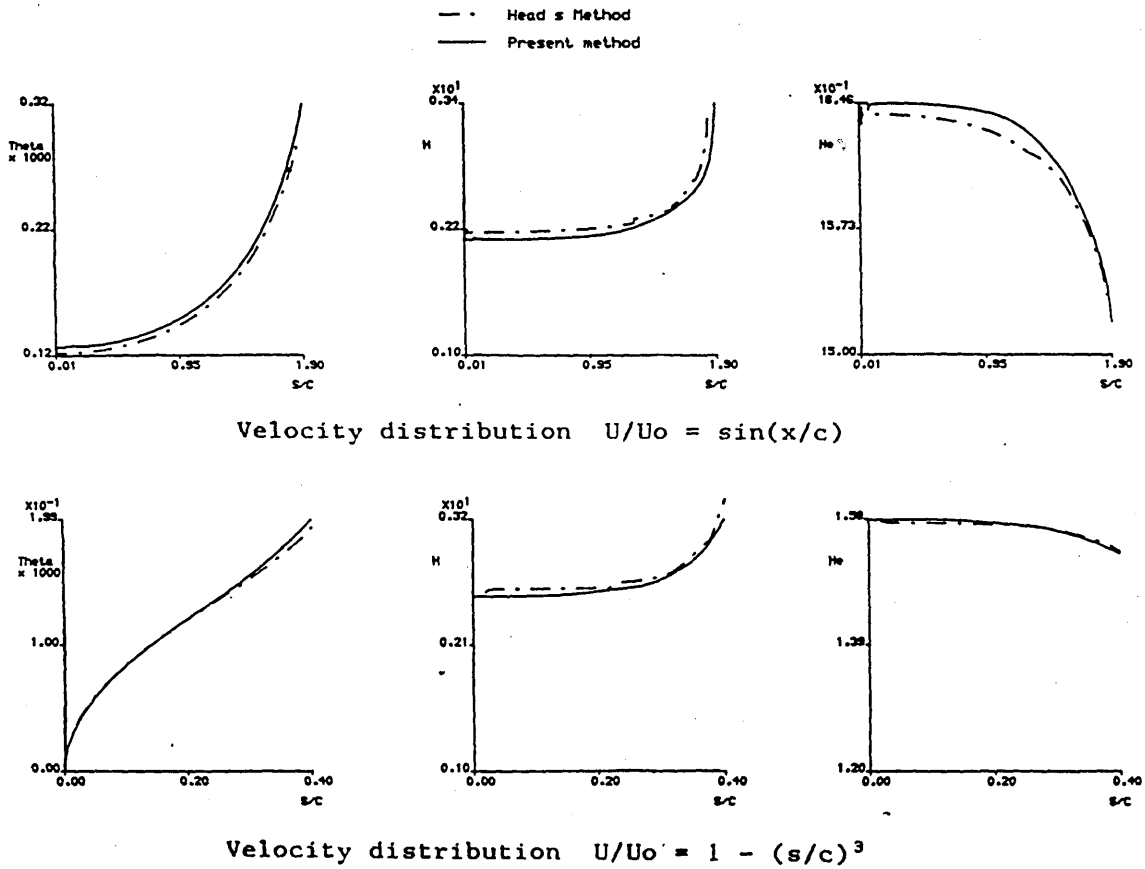


Fig. 3.5 Comparison between the predictions of the new method and that of Head.

— PRESENT METHOD
 - - - METHOD OF HEAD

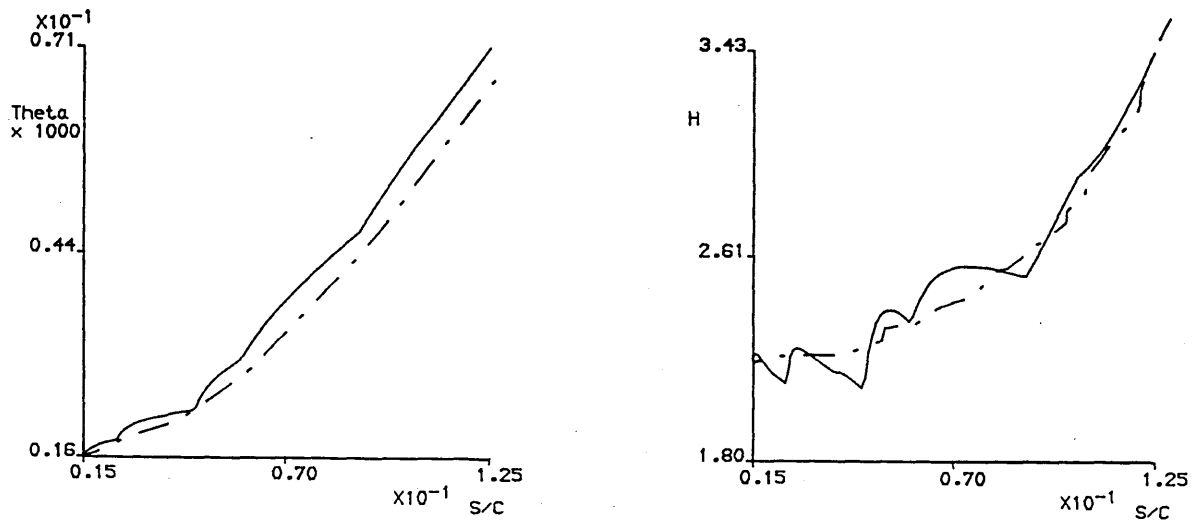


Fig. 3.6 Comparison between the prediction of the new method and that of Head for the GA(W)-1 aerofoil at 6.0 degrees.

PANEL CORNER
 POINTS

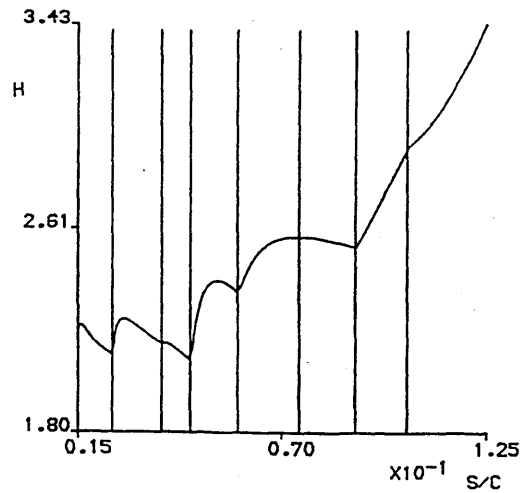


Fig. 3.7 Calculated development of H with inviscid panel corner points highlighted.

— PRESENT METHOD

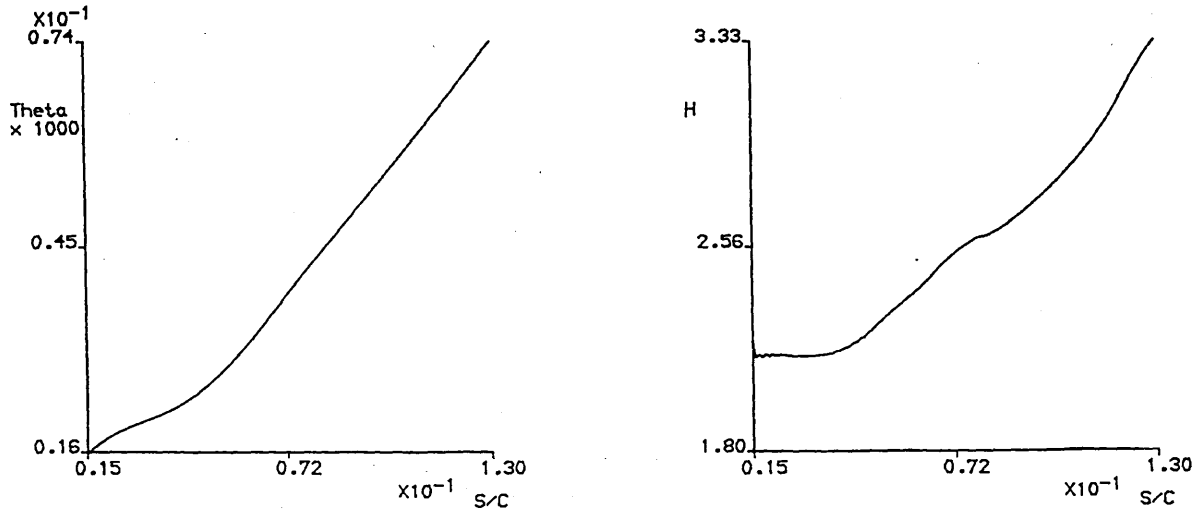


Fig. 3.8 Prediction obtained from new method with spline-fit representation of input velocity distribution.

— LAGRANGE INTERPOLATION
- - - LINEAR INTERPOLATION

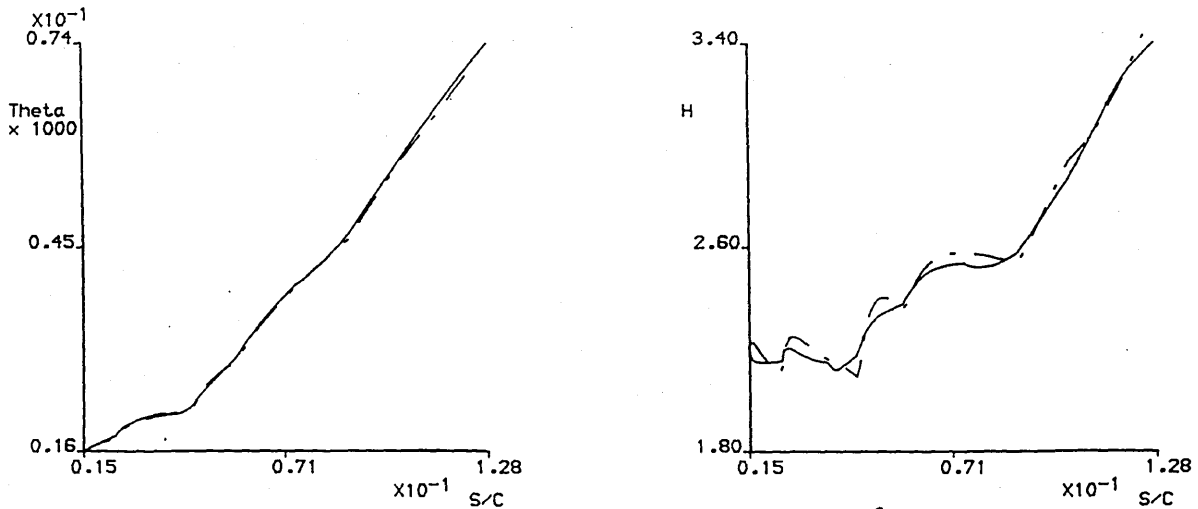


Fig. 3.9 Comparison between results obtained for a linearly interpolated and Lagrange interpolated velocity distribution input.

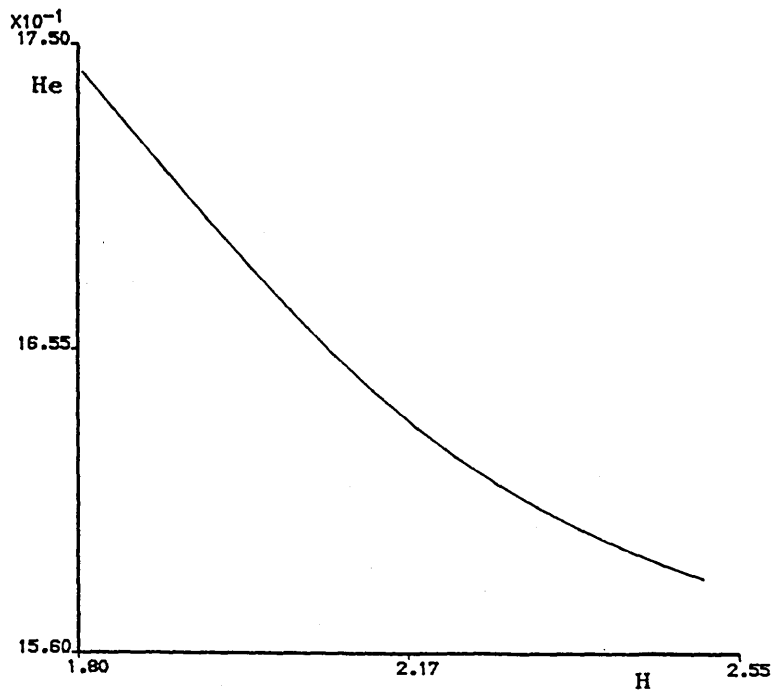


Fig. 3.10 Relationship between H and He for turbulent flow.

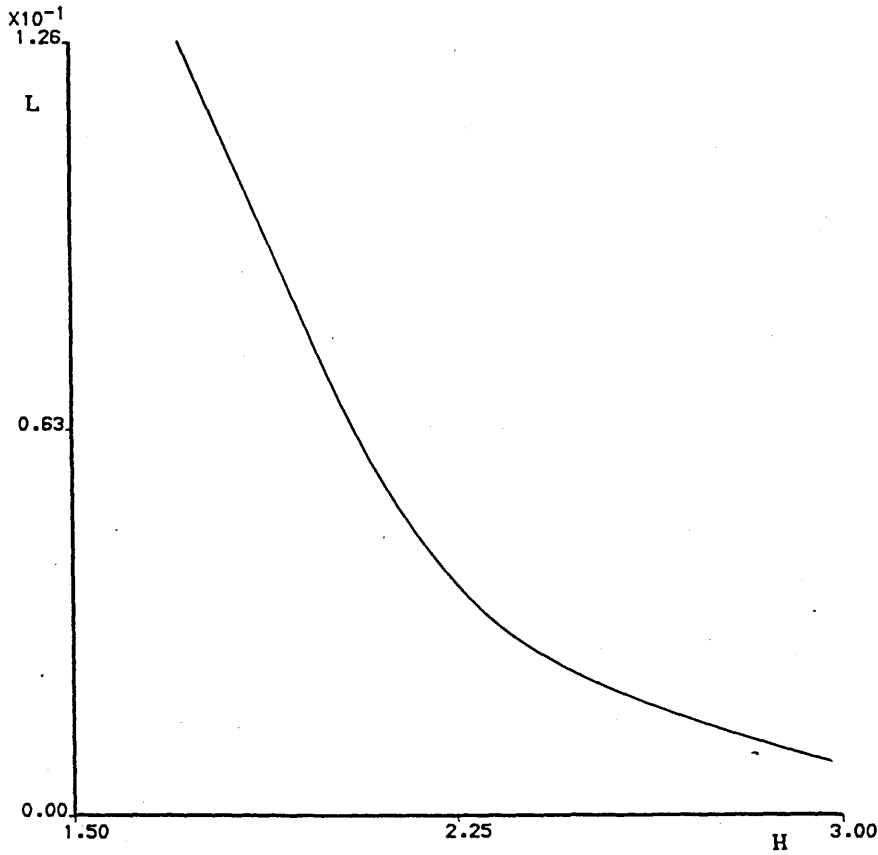
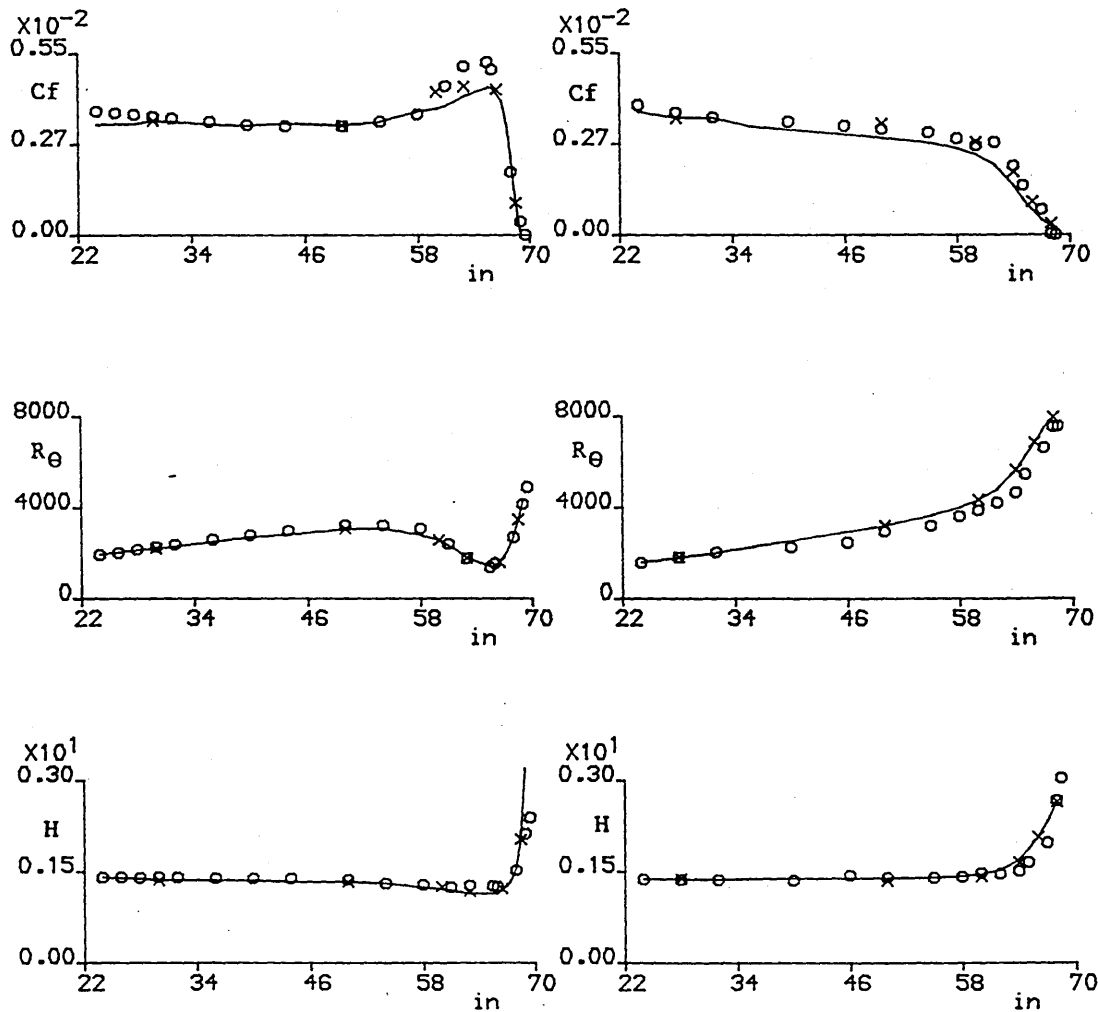


Fig. 3.11 Relationship between H and L for turbulent flow.

o Measured data
 x Assassa & Papailiou
 — Present Calculation



SERIES I

SERIES II

Fig. 3.12 Comparison between the present method and the calculations of Assassa and Papailiou for the cases of Chu and Young.

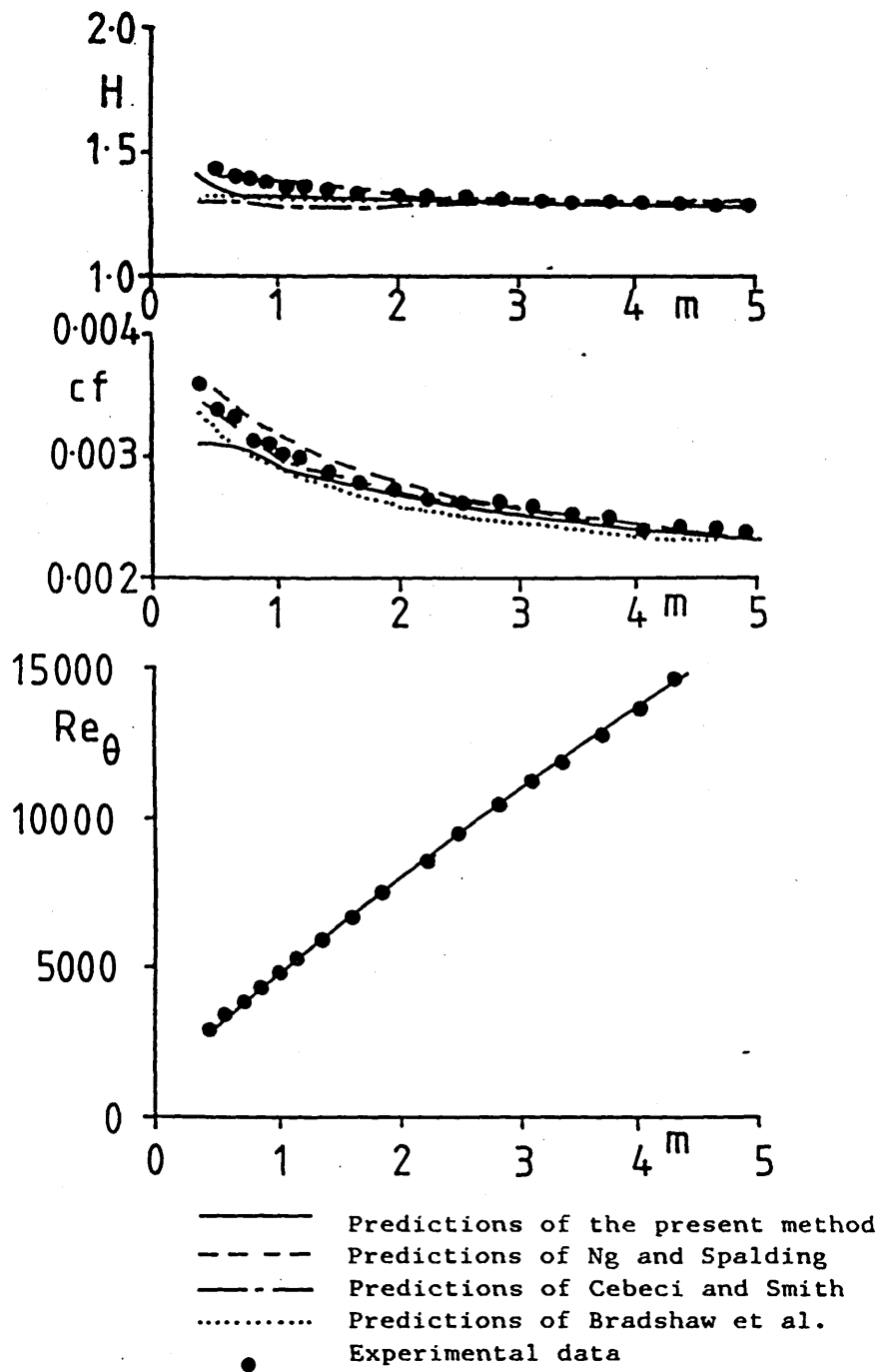


Fig. 3.13 Comparison of the predictions of the present method with those of Ref. 40. for the data of Wieghardt.

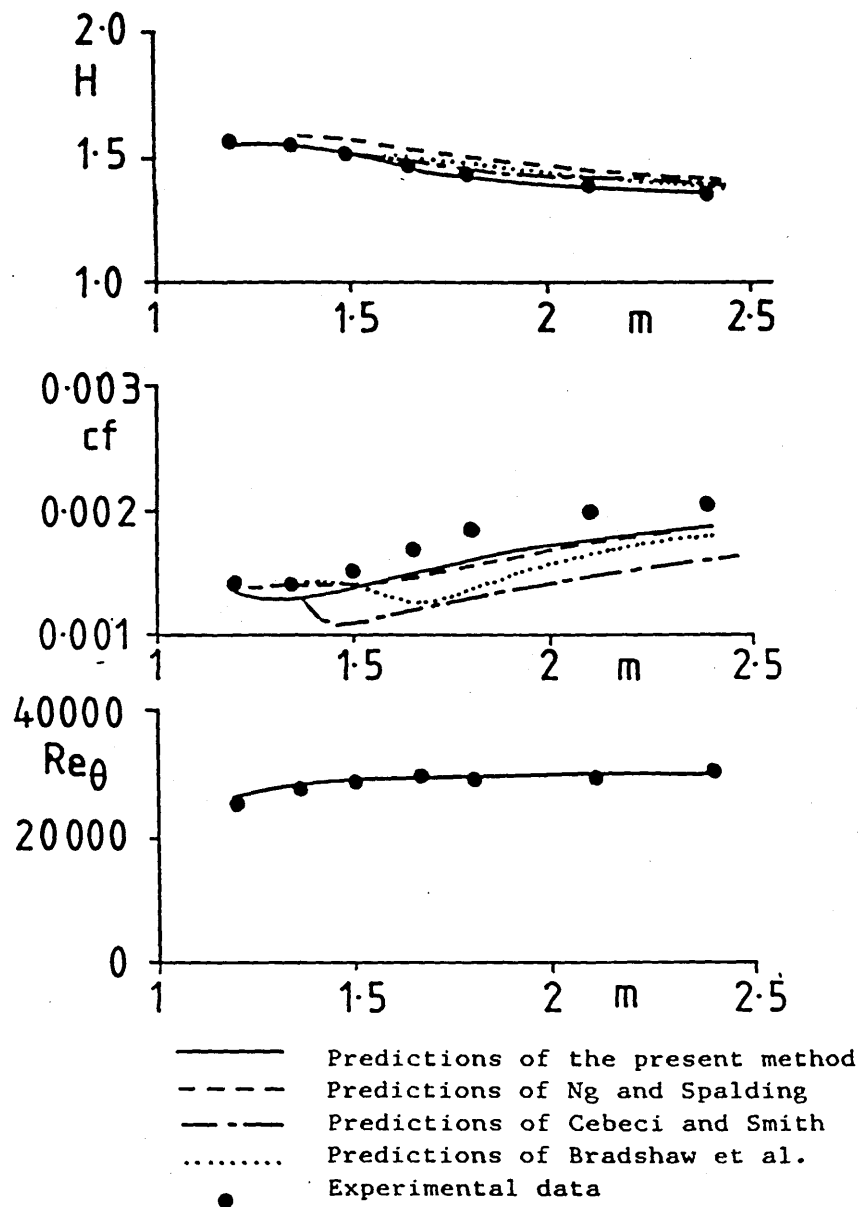


Fig. 3.14 Comparison of the predictions of the present method with those of Ref. 40. for the relaxing flow of Bradshaw and Ferriss.

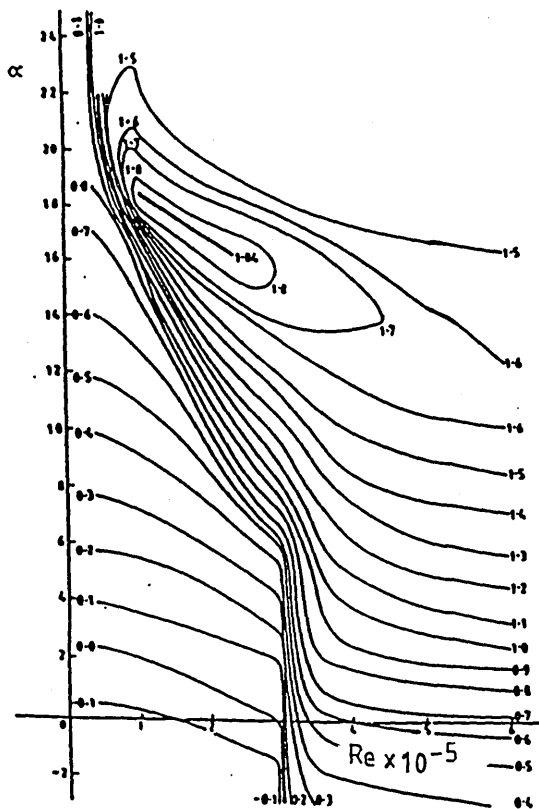


Fig. 4.1 Lift coefficient contours for the GU25-5(11)8 aerofoil with incidence and Reynolds Number. (Taken from Ref. 29.)

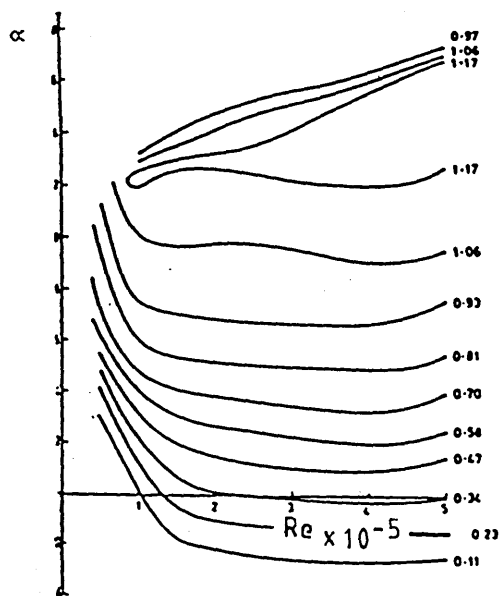


Fig. 4.2 Lift coefficient contours for the GA(W)-1 aerofoil with incidence and Reynolds number. (Taken from Ref. 43.)

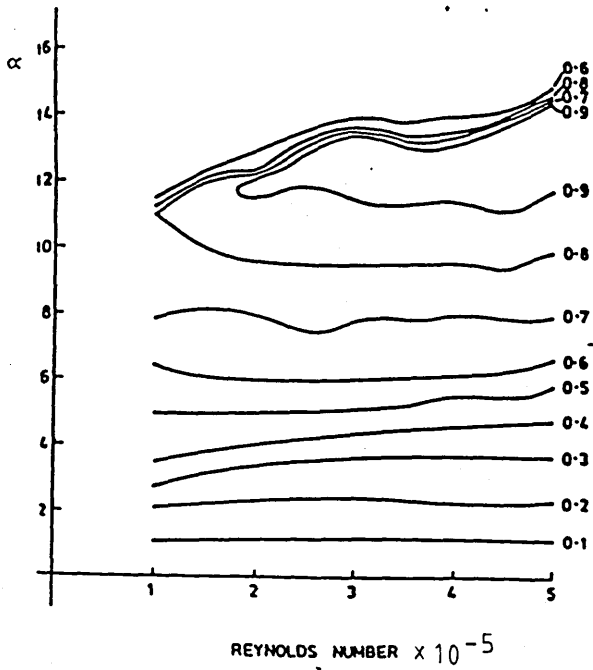


Fig. 4.3 Lift coefficient contours for the NACA 0015 aerofoil with incidence and Reynolds number. (Taken from Ref. 43.)

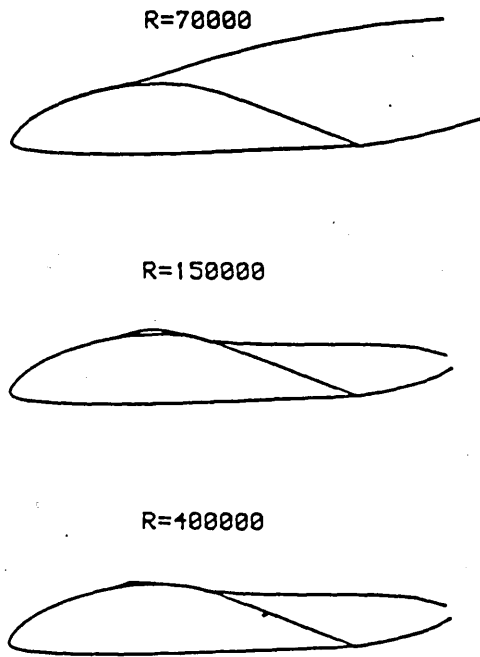


Fig. 4.4a Boundary Layer Behaviour

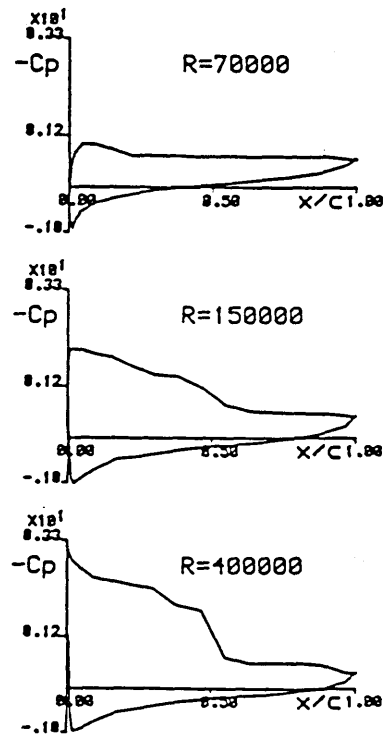


Fig. 4.4b Pressure Distribution Behaviour

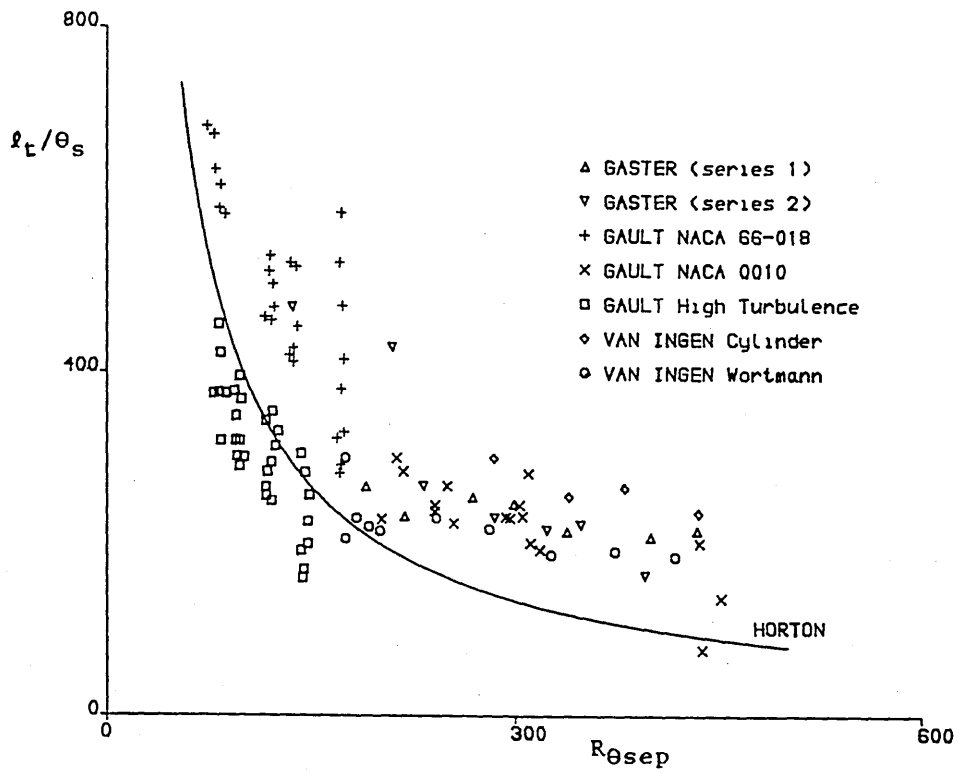


Fig. 4.5 Non-dimensional Laminar Shear Layer Length
 Versus $R_{\theta_{sep}}$

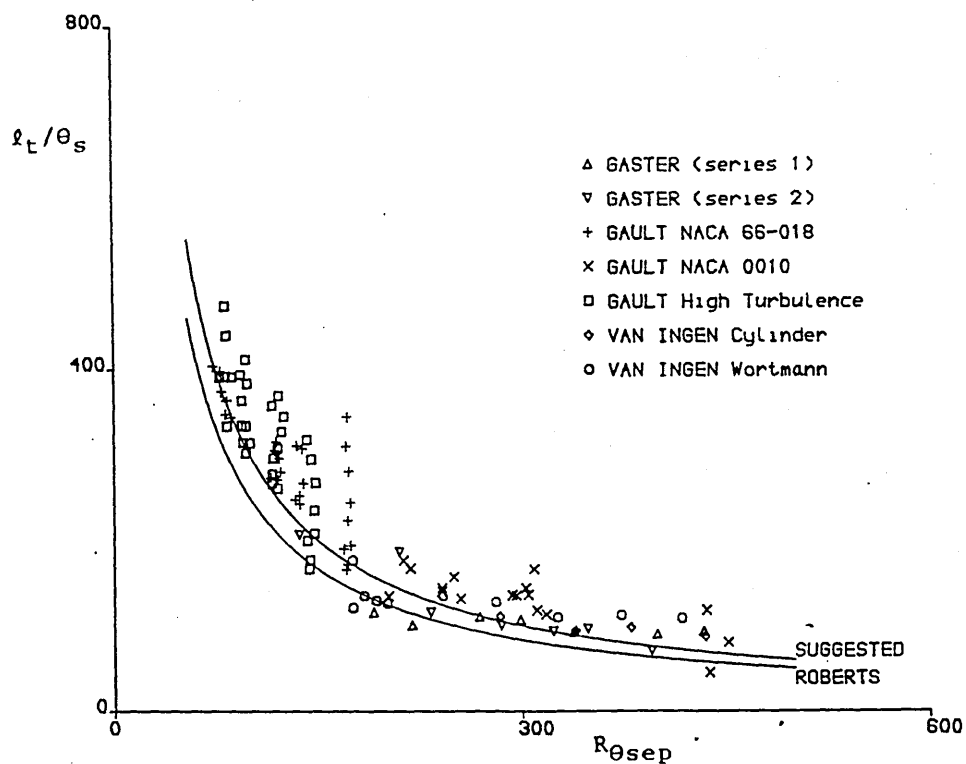


Fig. 4.6 Non-dimensional Laminar Shear Layer Length
 Versus $R_{\theta_{sep}}$ (Turbulence Correction Applied)

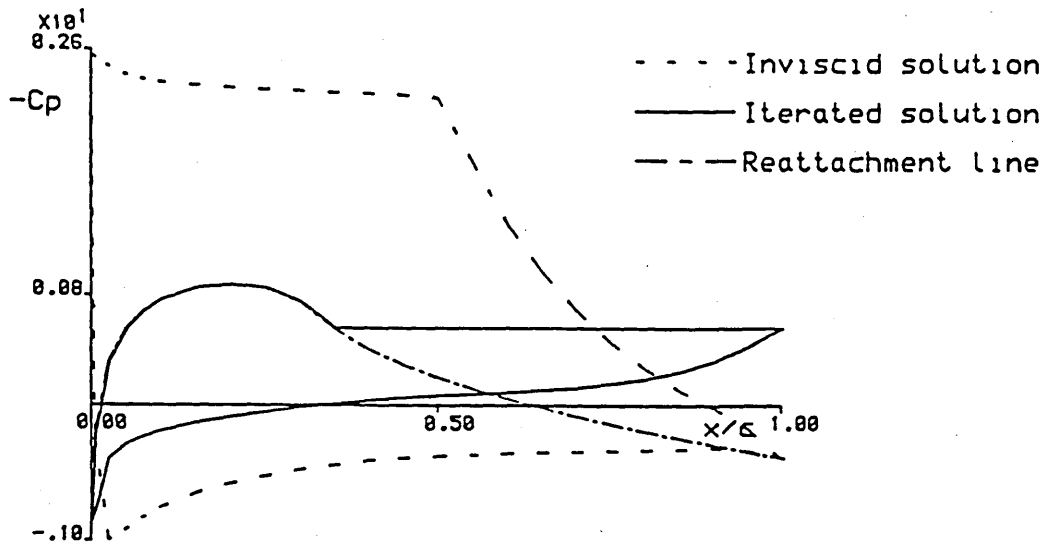


Fig. 4.7 Development of Long Bubble Reattachment Line

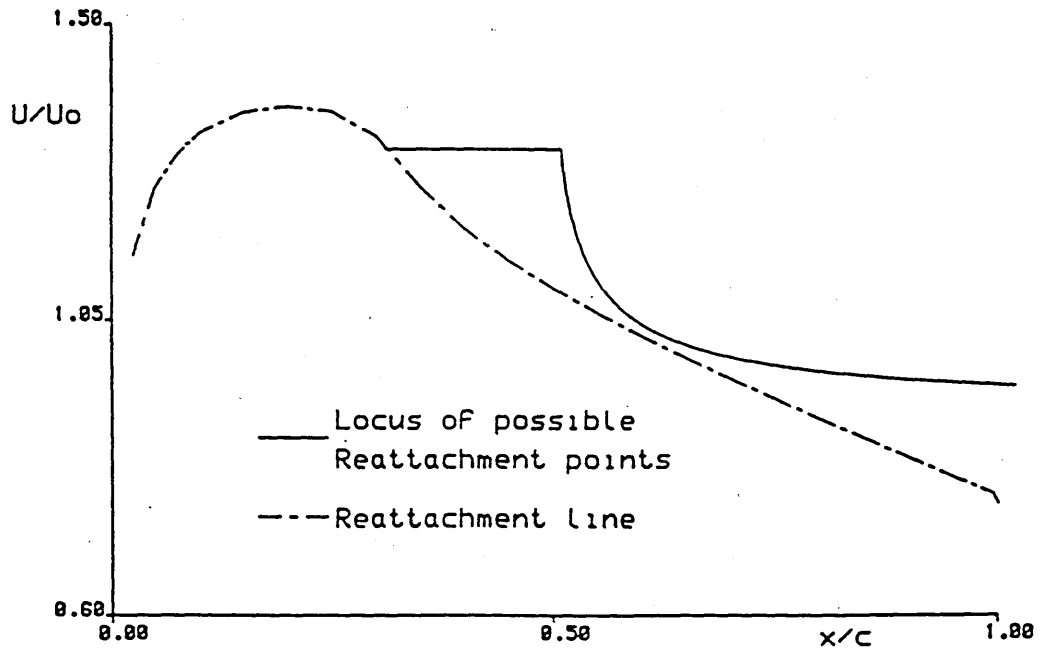


Fig. 4.8 Behaviour of Locus of Possible Reattachment Points With Respect to the Developed Reattachment line

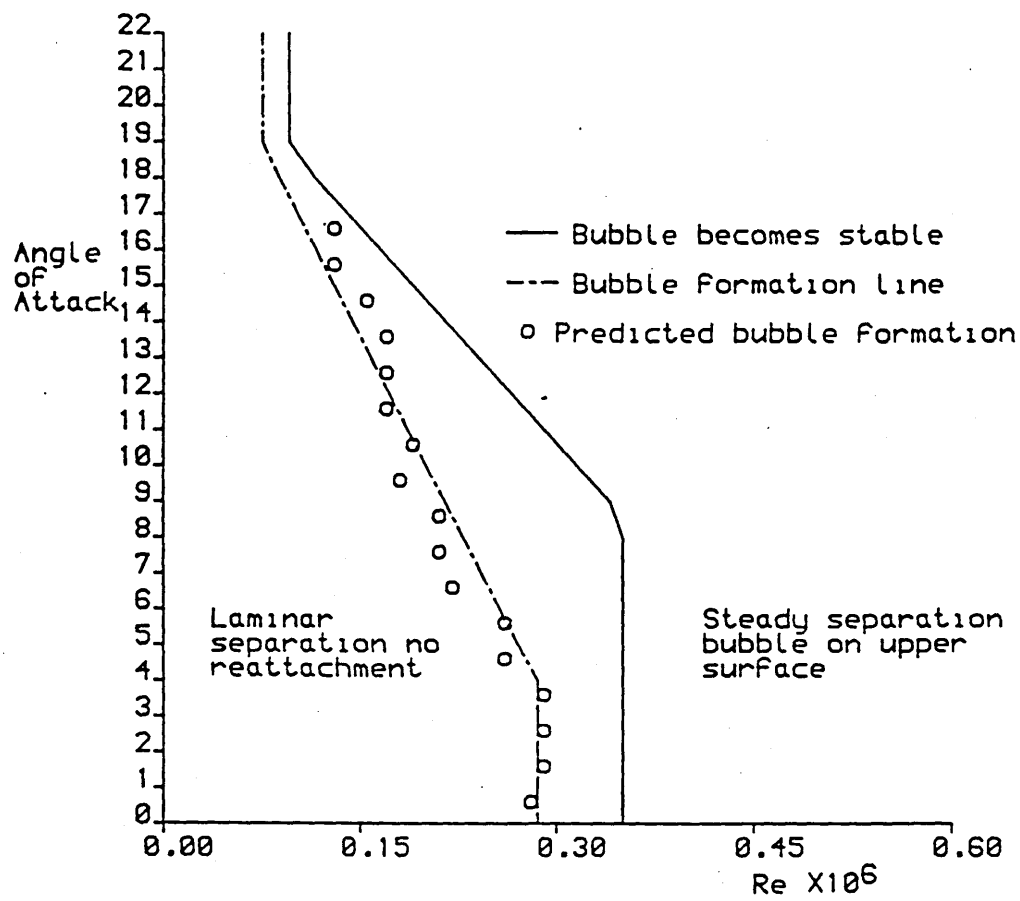


Fig. 4.9 Idealised Representation of Fig. 4.1, with Predicted Reattachment Points

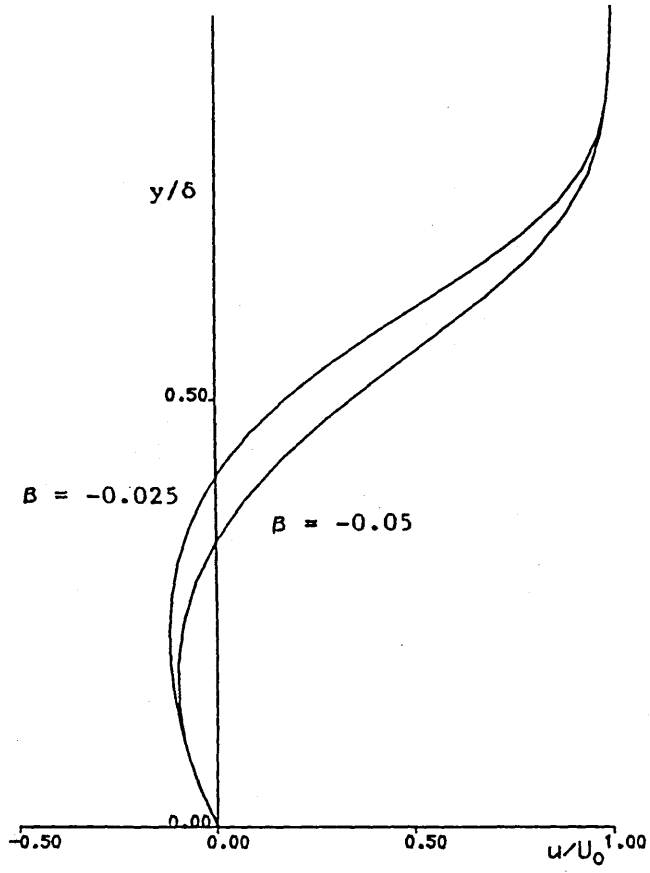


Fig. 5.1 Stewartson velocity profiles used to develop the separated flow profile family.

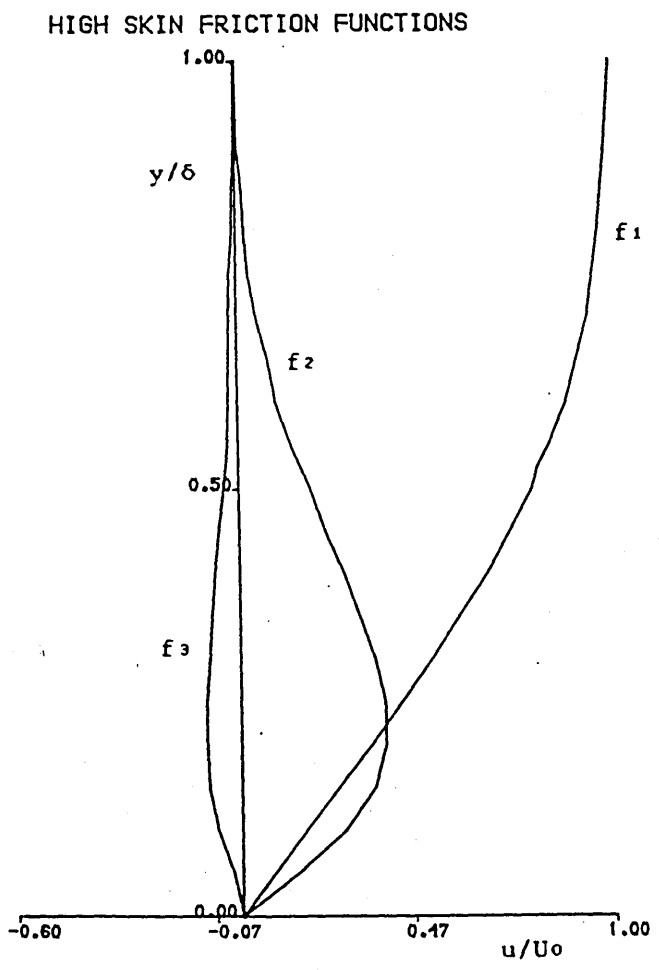


Fig. 5.2(a) Velocity profile function values for high skin friction cases.

SEPARATION PROFILE FUNCTIONS

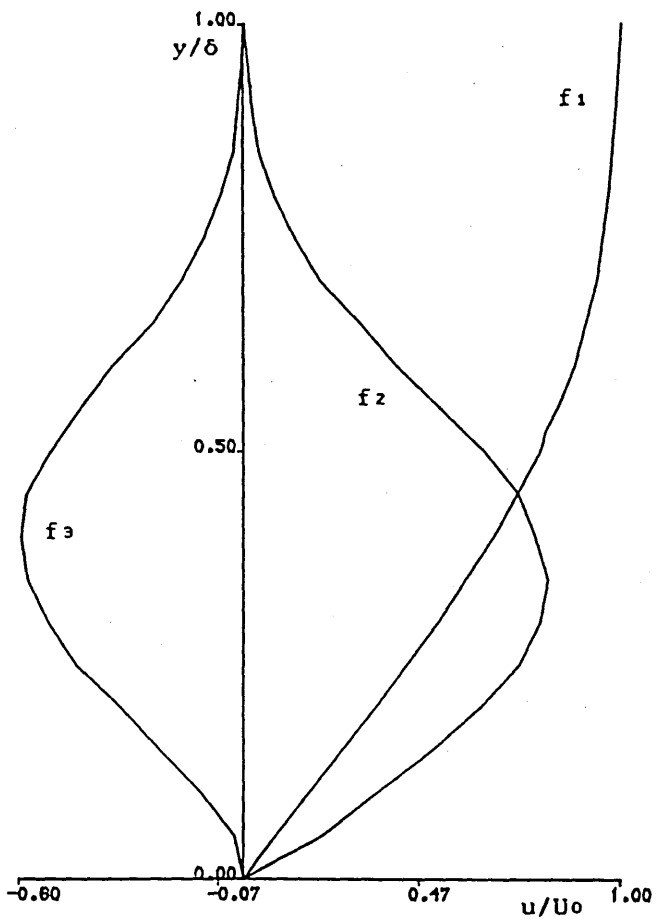


Fig. 5.2(b) Velocity profile function values for separation cases.

STEWARTSON PROFILE FUNCTIONS

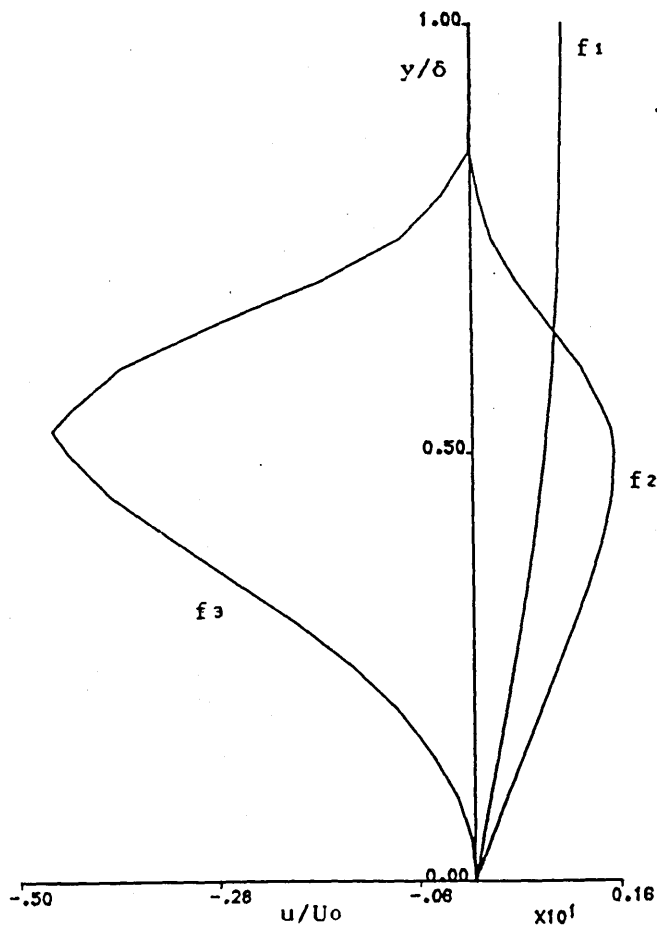


Fig. 5.2(c) Velocity profile function values for Stewartson profiles.

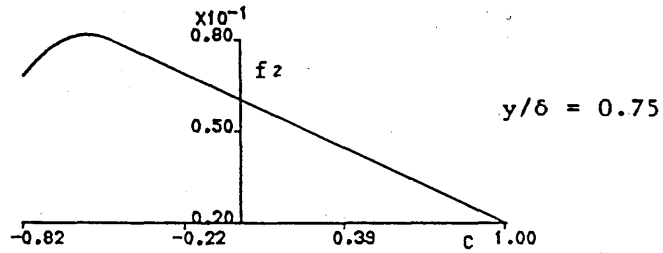
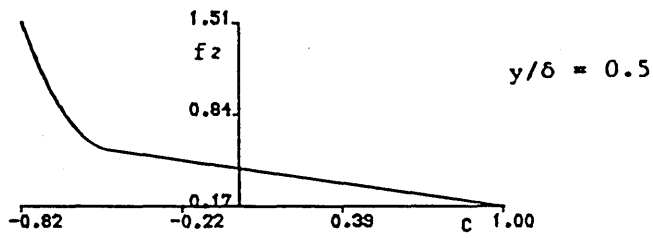
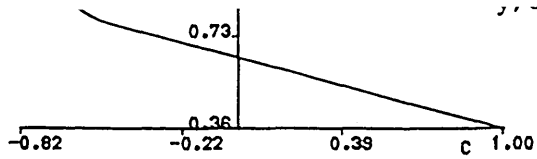


Fig. 5.3 Variation of the function f_2 with c .

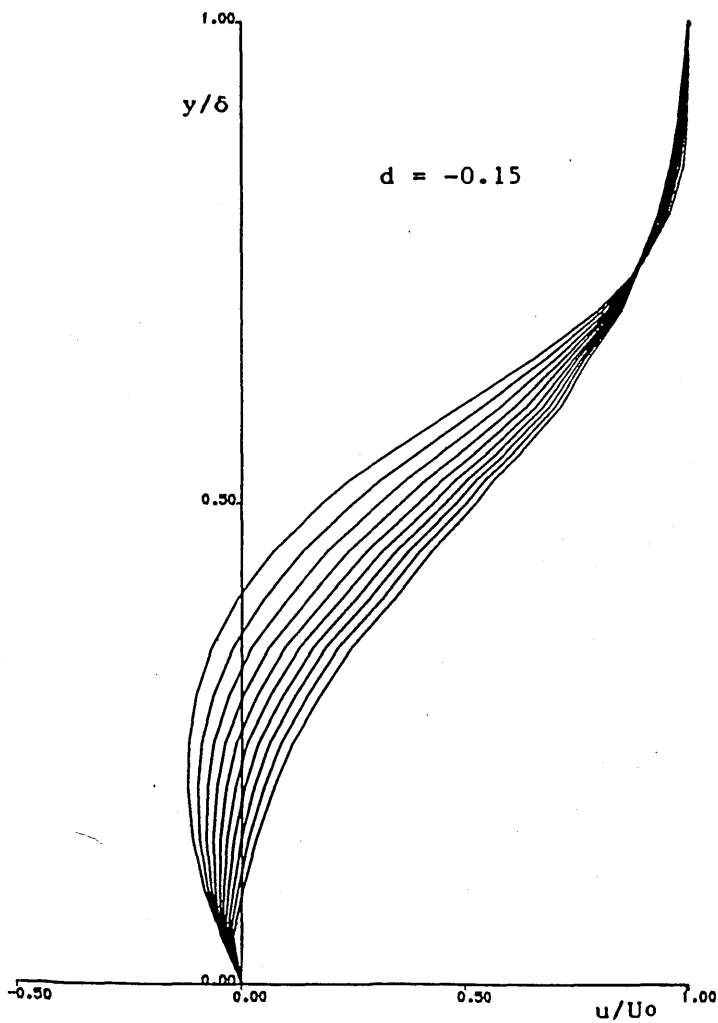


Fig. 5.4 Velocity profiles produced by varying the parameter c for a constant d .

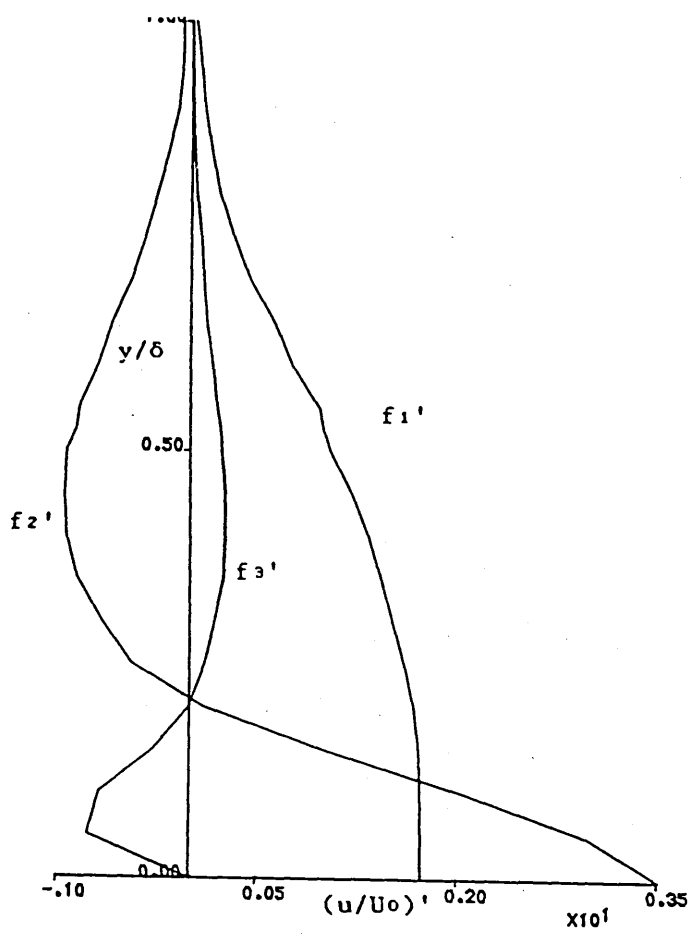


Fig. 5.5(a) Derivatives of profile functions for the high skin friction cases.

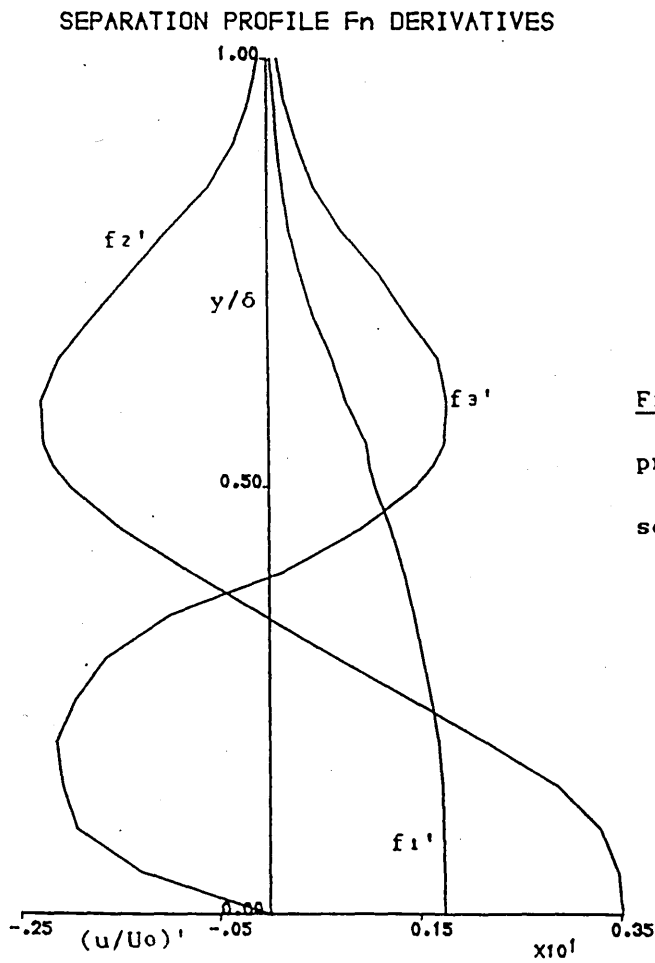


Fig. 5.5(b) Derivatives of profile functions for the separation cases.

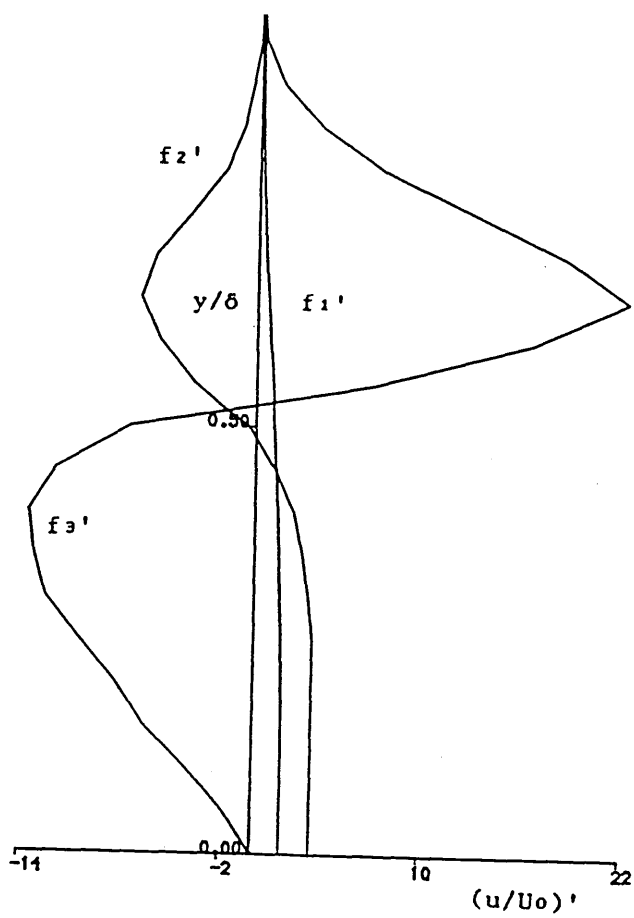


Fig. 5.5(c) Derivatives of profile functions for the Stewartson velocity profiles.

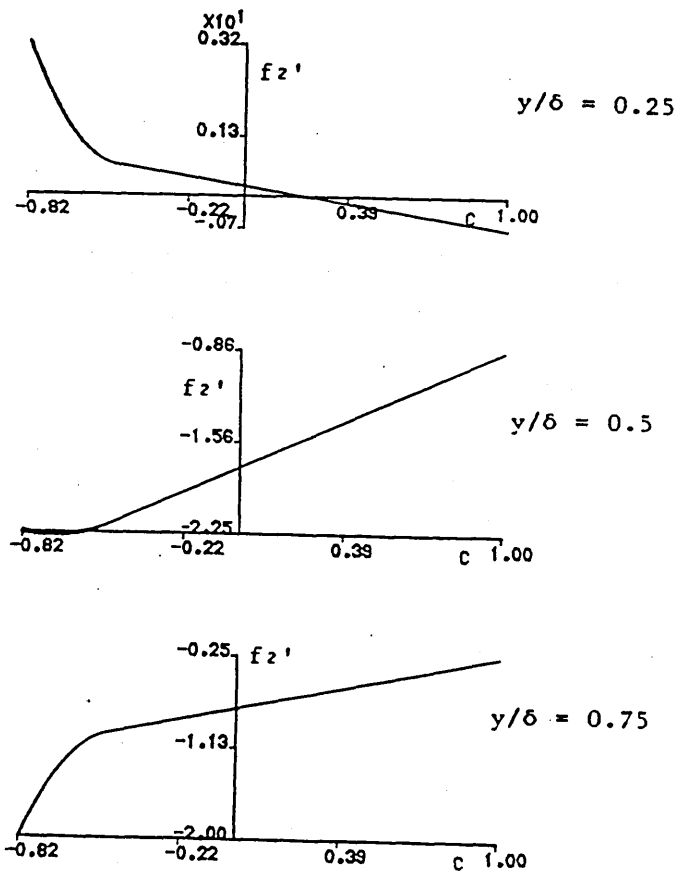


Fig. 5.6 Variation of f_2' with c .

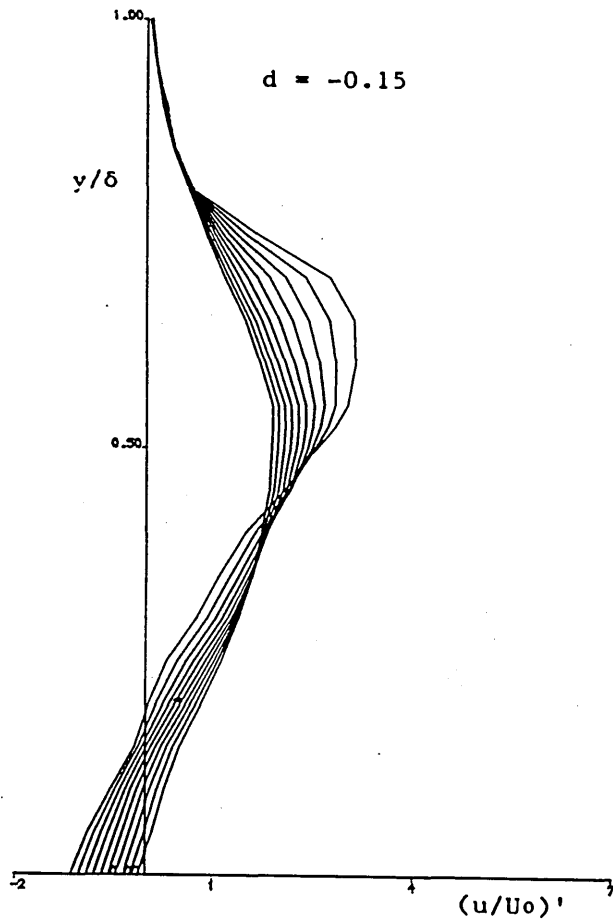
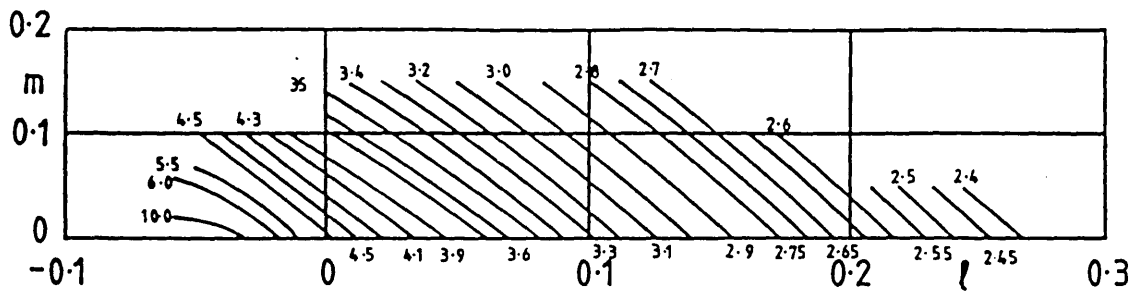
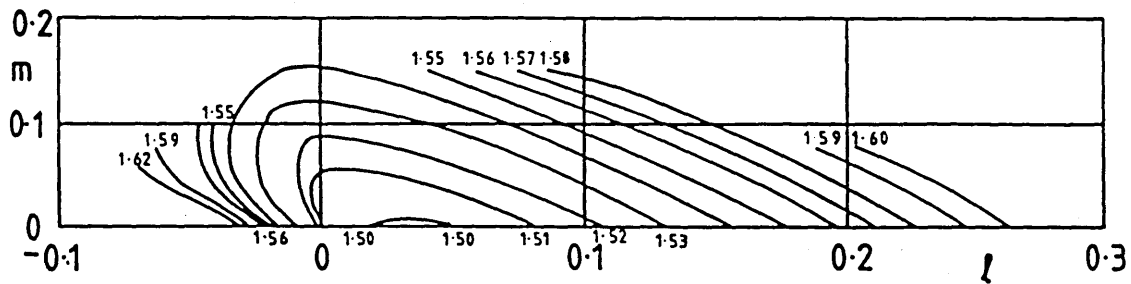


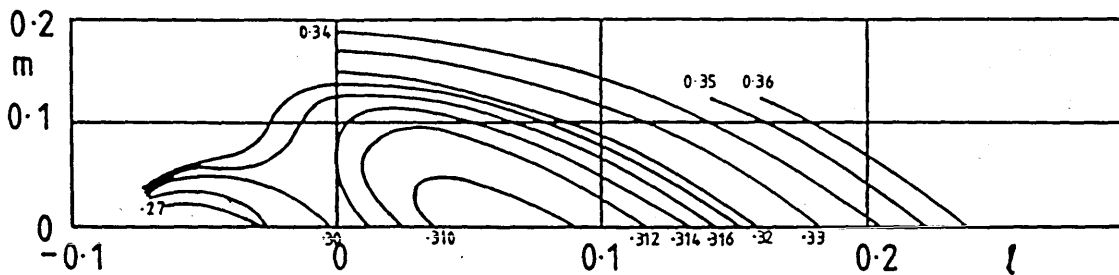
Fig. 5.7 Velocity profile derivatives produced by varying the parameter c for a constant d .



Contours of H



Contours of He



Contours of $2D^*$

Fig. 5.8 Parameter charts of Head extended for separated flow.

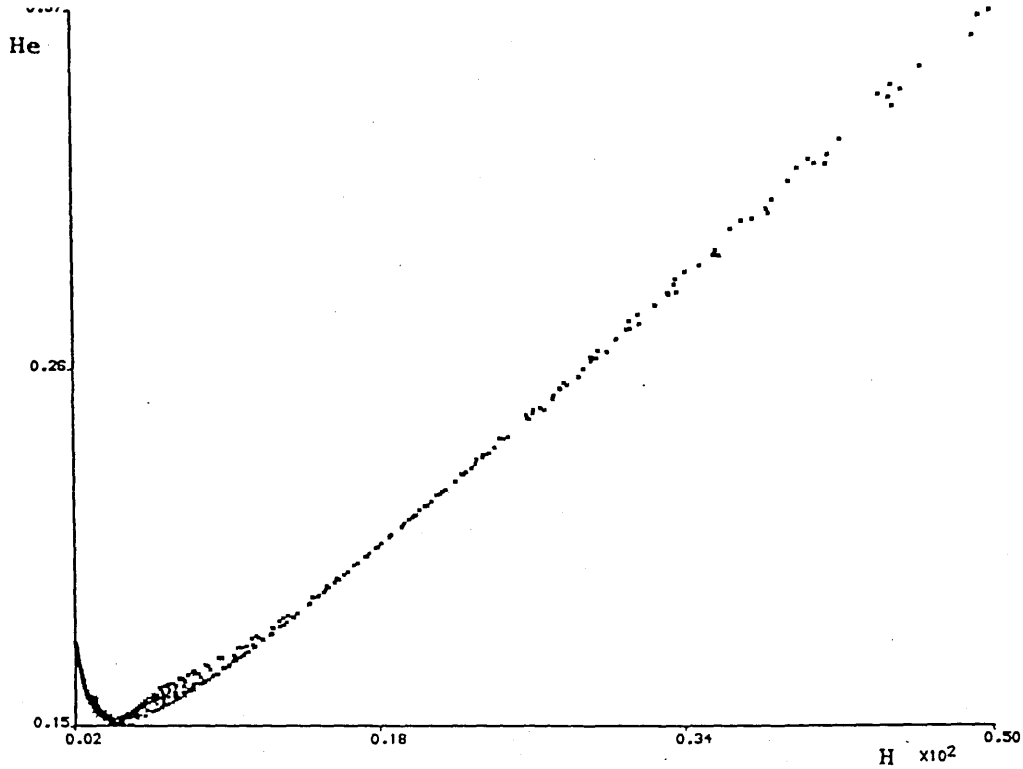


Fig. 5.9 Values of H versus He calculated from velocity profile family.

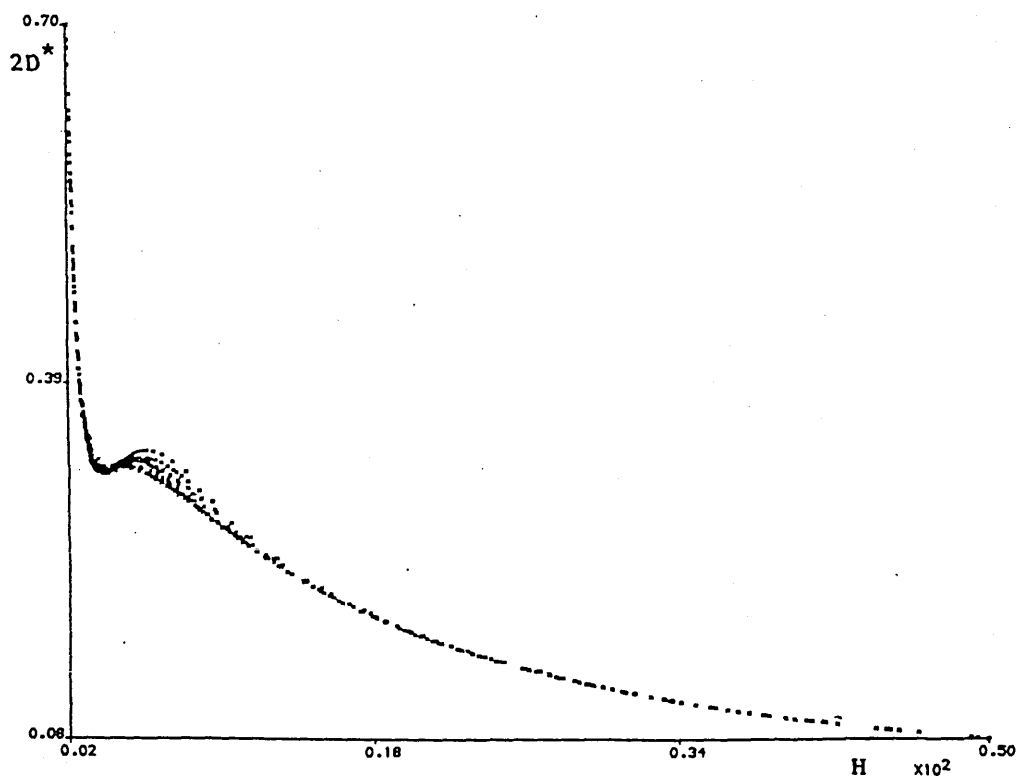


Fig. 5.10 Values of H versus 2D* calculated from velocity profile family.

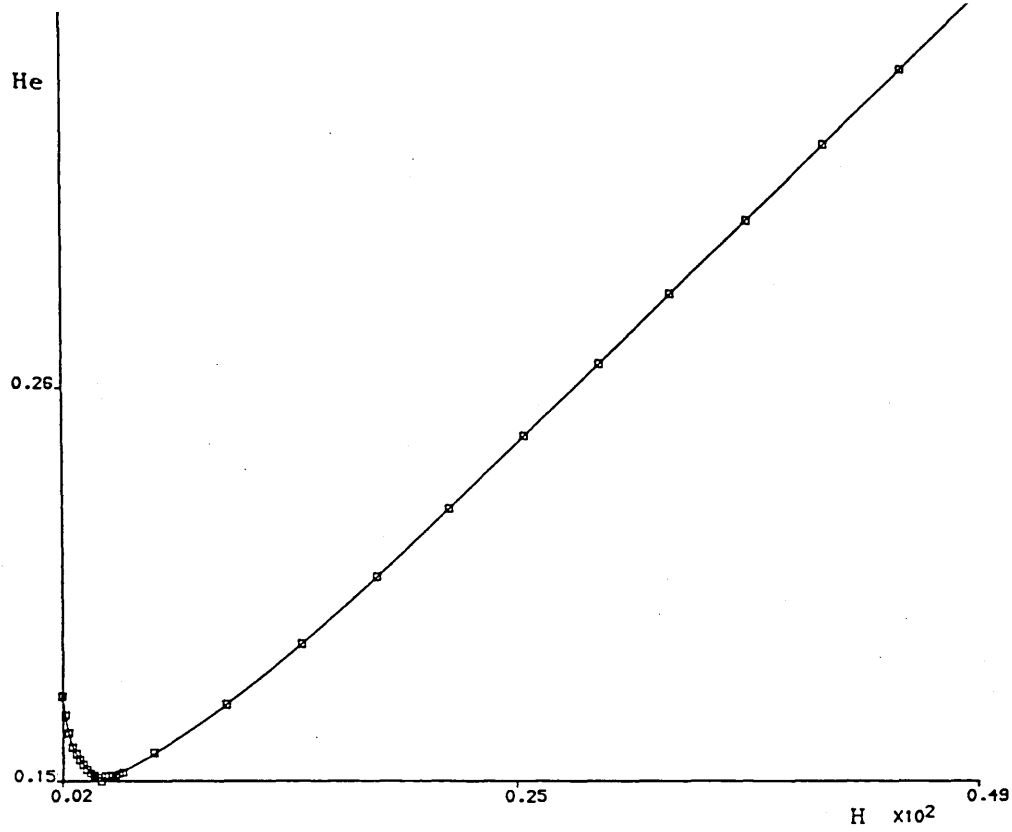


Fig. 5.11 Spline-fit representation of the H-He relation along with the filtered data points used to define the curve.

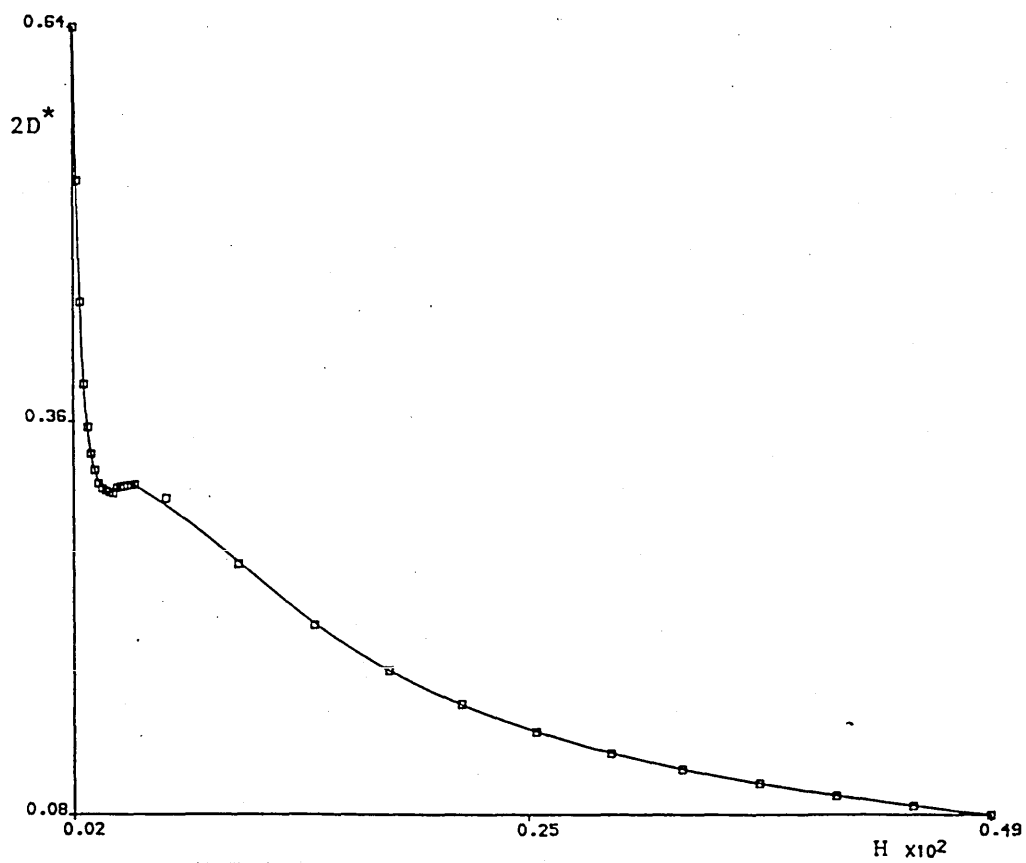


Fig. 5.12 Spline-fit representation of the H-2D* relation along with the filtered data points used to define the curve.

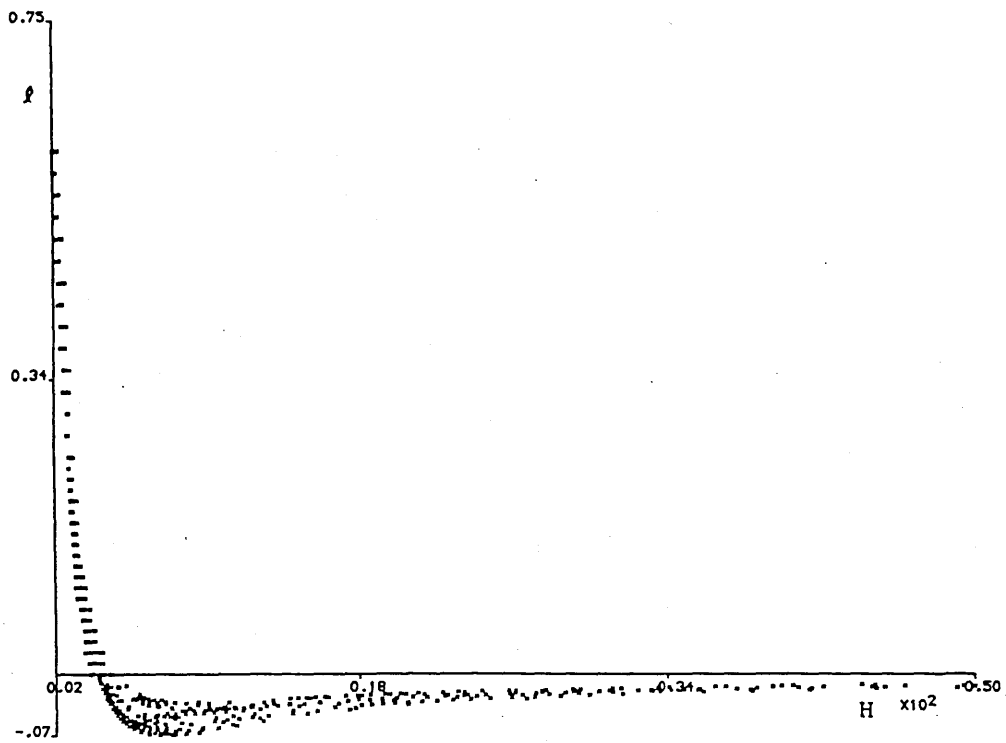


Fig. 5.13 Behaviour of Head's profile parameter l with varying form parameter.

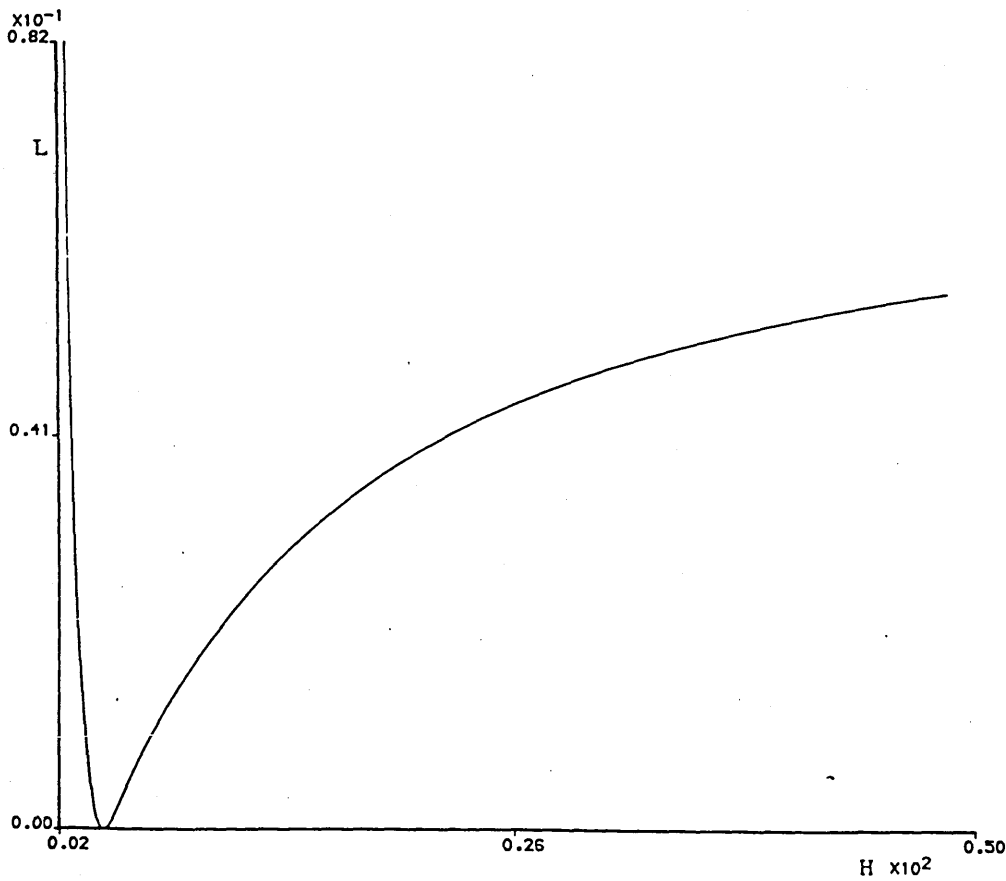


Fig. 5.14 Calculated spline-fit representation of the H-L relation.

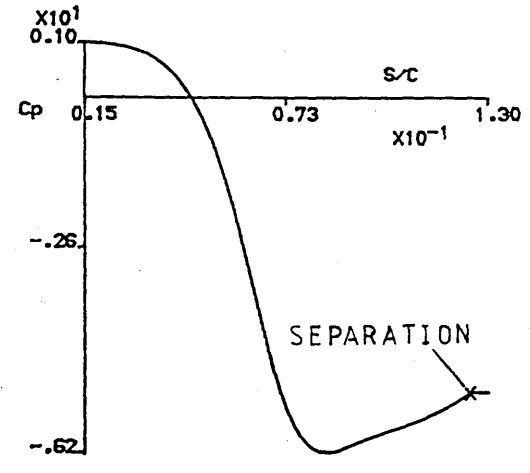
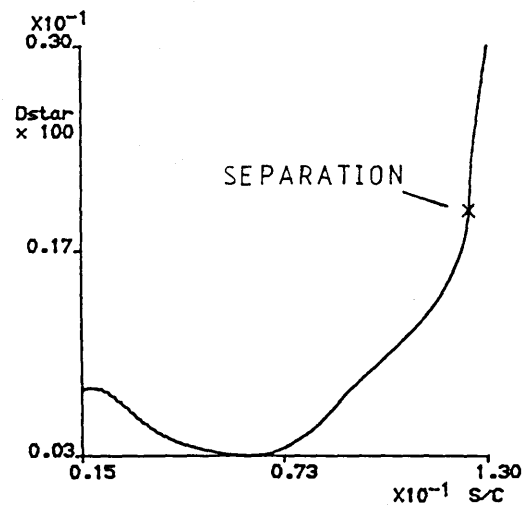
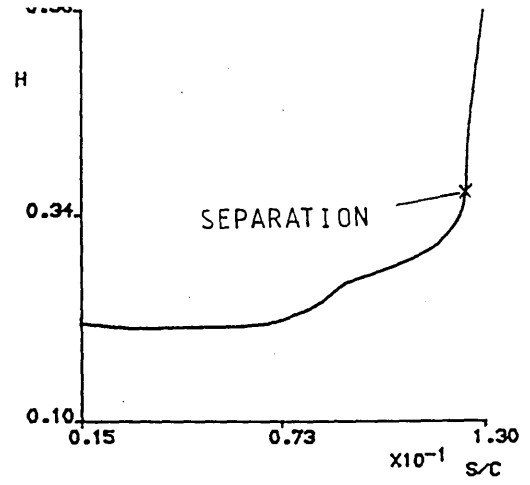
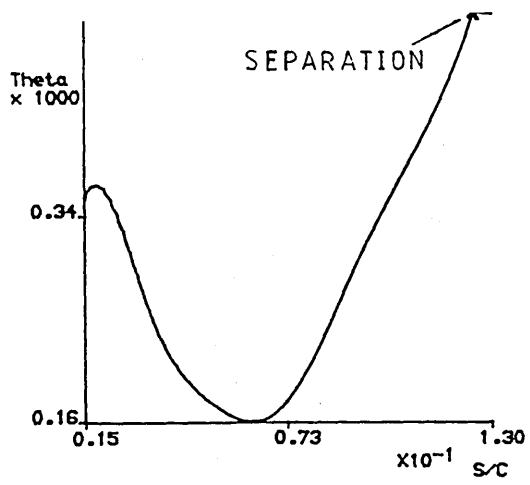


Fig. 5.15 Calculated boundary layer development for the GA(W)-1 aerofoil at 20 degrees, $Re = 6 \times 10^6$, with constant pressure plateau after separation.

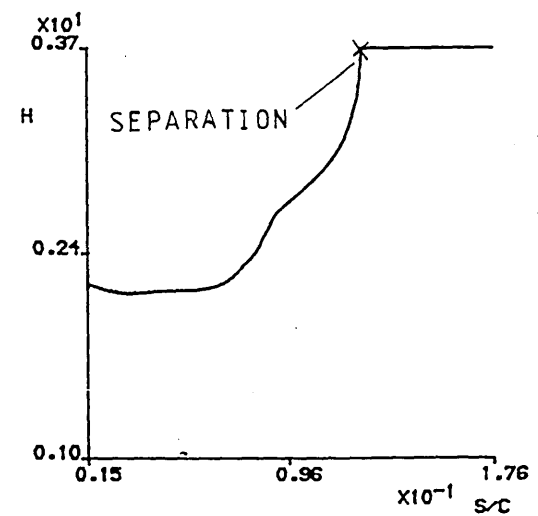
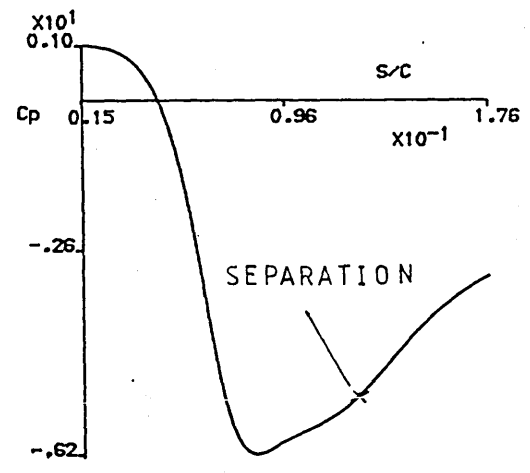


Fig. 5.16 Form parameter prediction obtained for the GA(W)-1 aerofoil at 20 degrees, $Re = 6 \times 10^6$, inviscid pressure distribution.

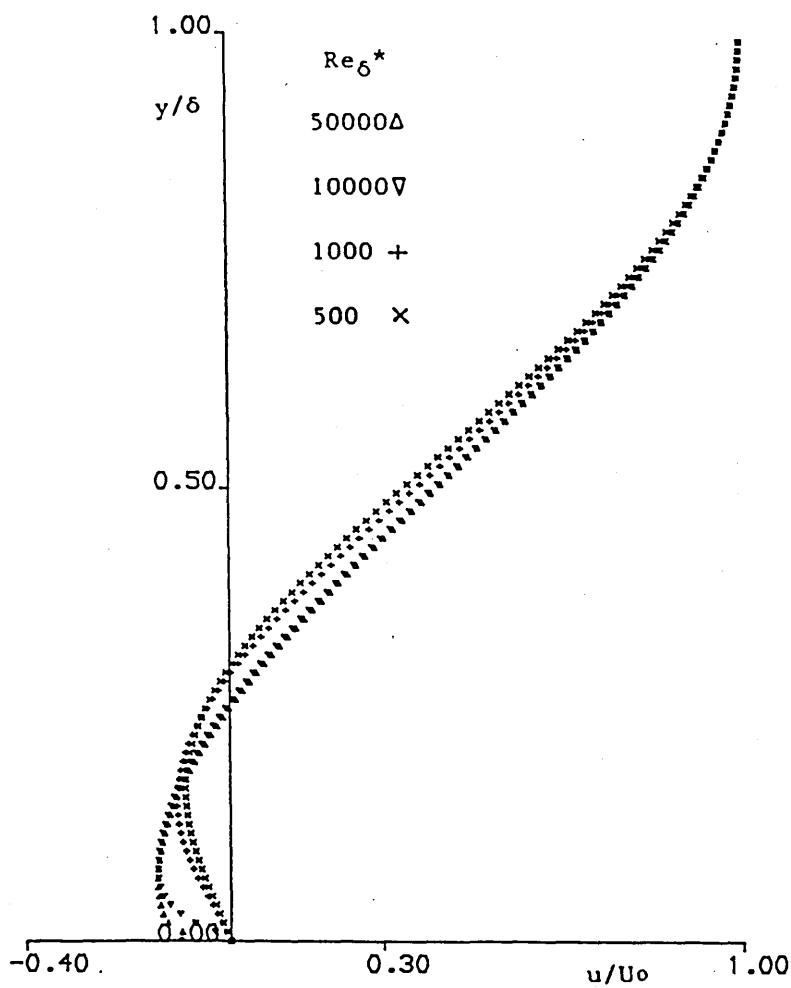
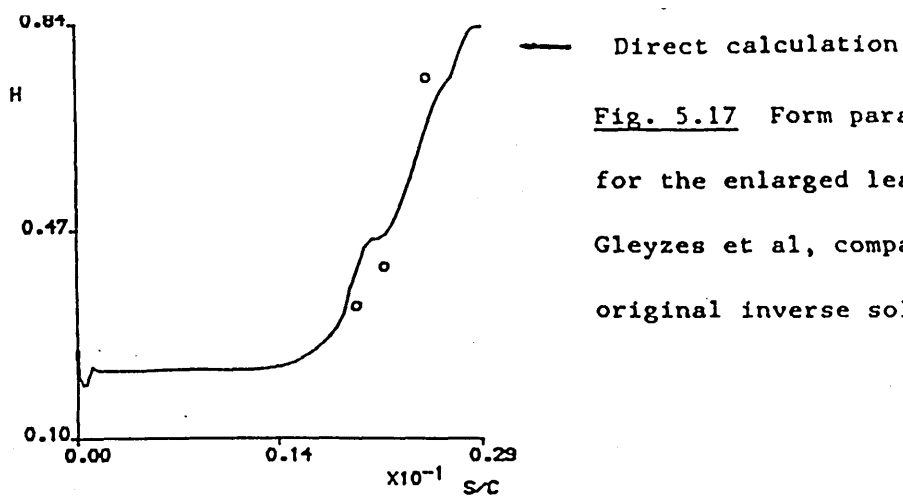


Fig. 5.18 Calculated velocity profiles for four different values of Re_{δ}^* , $H = 8.0$.

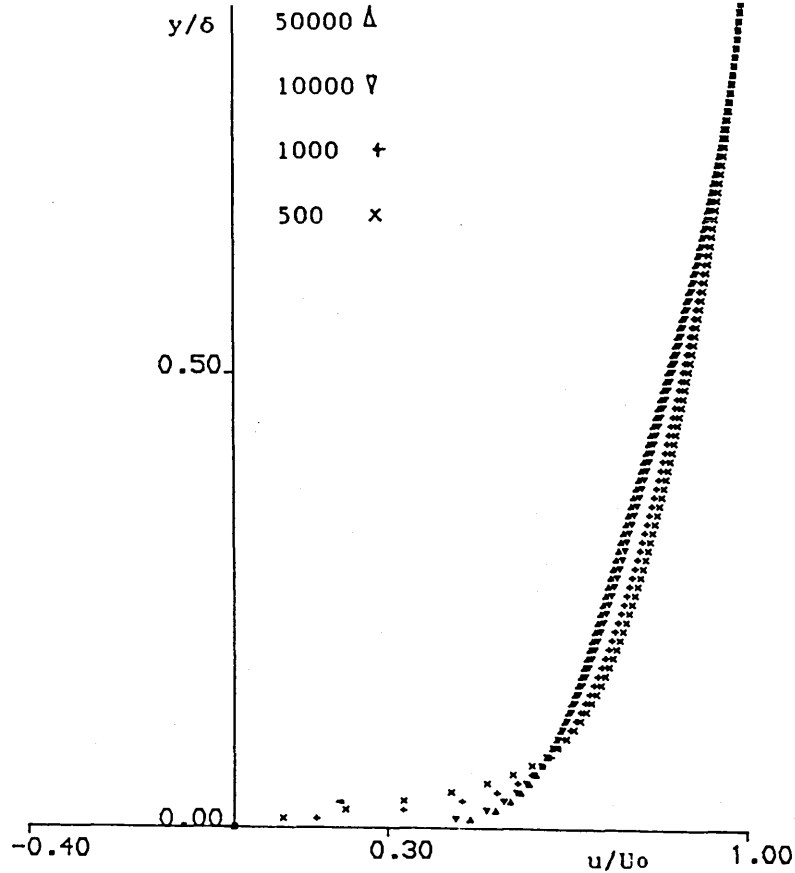


Fig. 5.19 Calculated velocity profiles for four different values of Re_{δ}^* , $H = 1.4$.

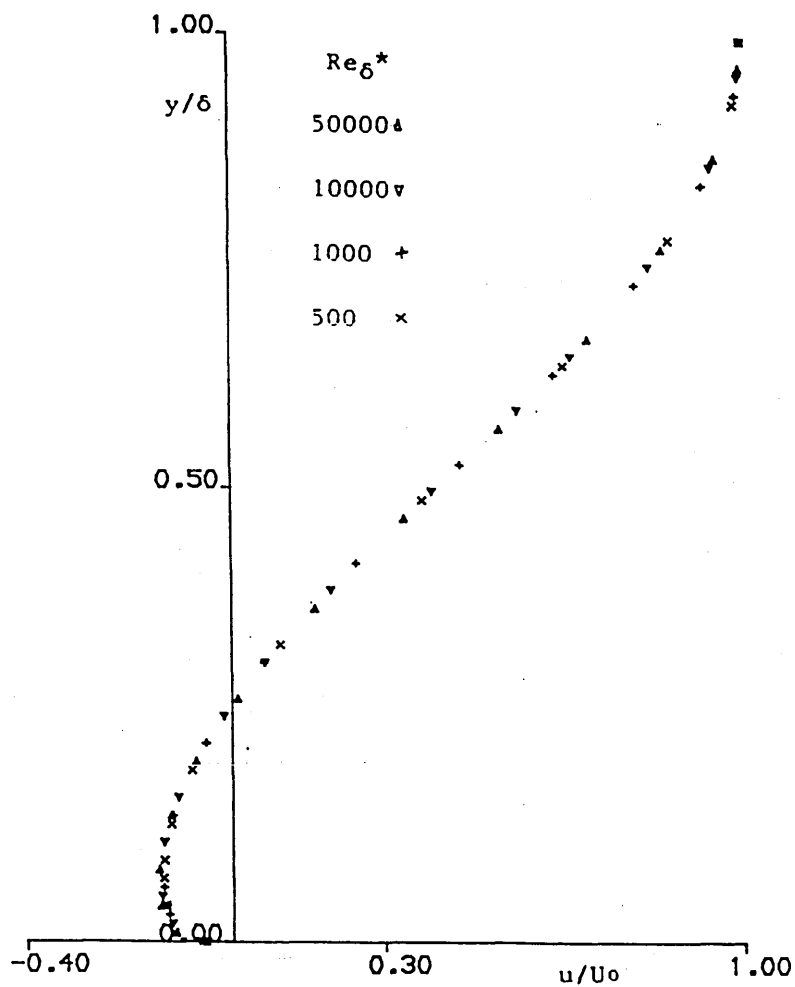


Fig. 5.20 Calculated velocity profiles for four different values of Re_{δ}^* , $H = 8.0$, with the extra exponential terms removed.

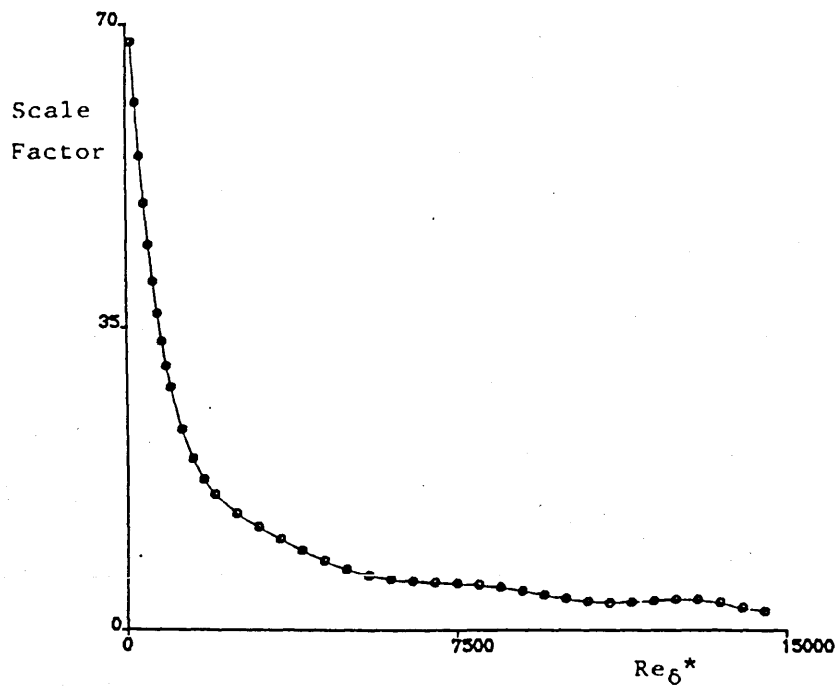
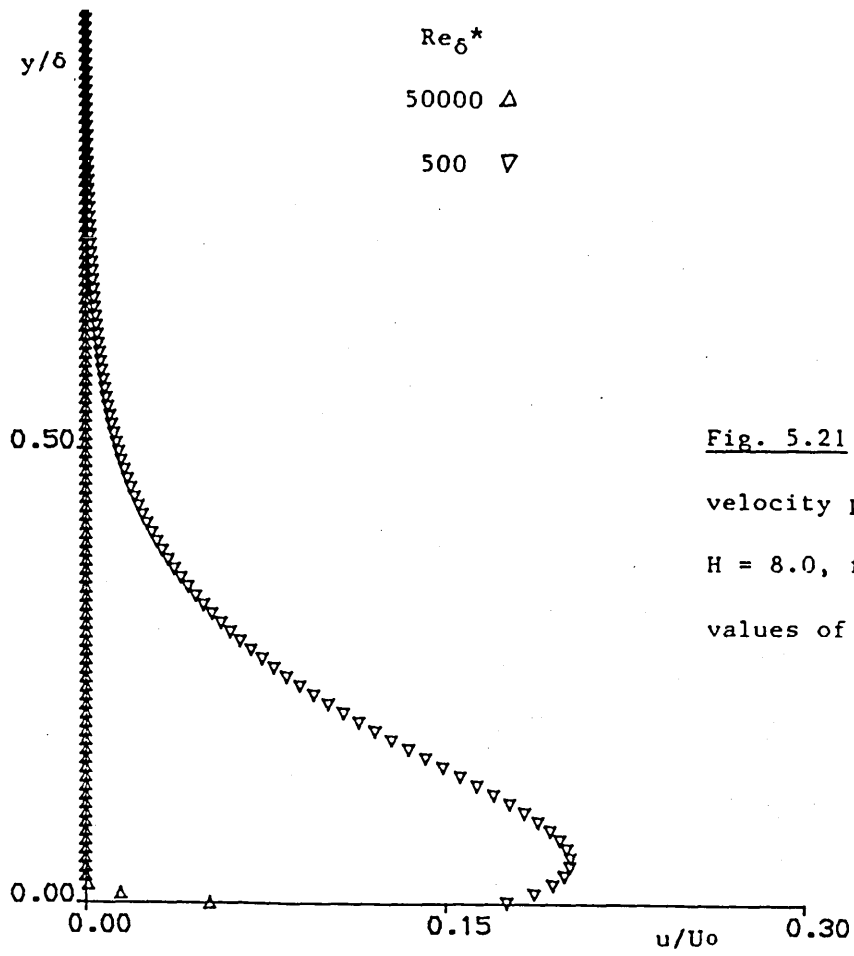


Fig. 5.22 Variation of the exponential term scale factor with Re_{δ}^* .

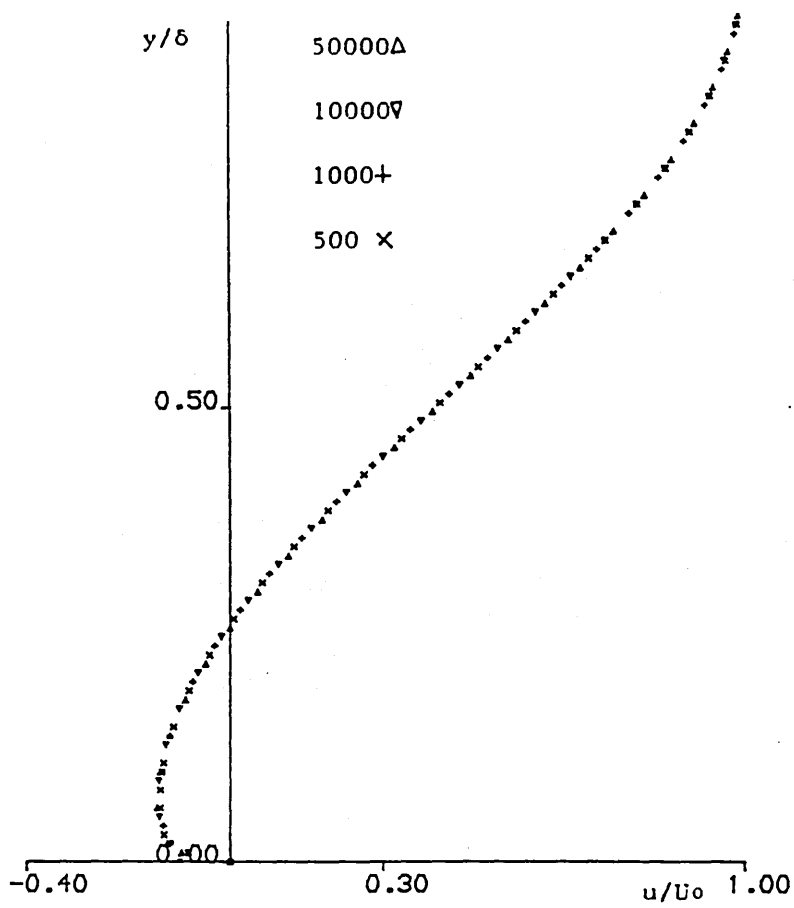


Fig. 5.23 Calculated velocity profiles for four different values of Re_δ^* , $H = 8.0$, with scaled exponential terms.

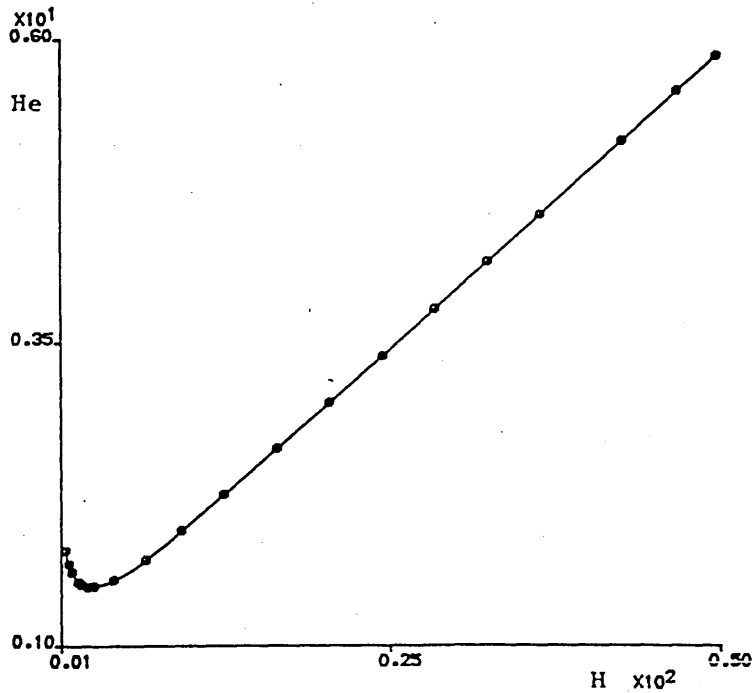


Fig. 5.24 Spline-fit representation of the calculated H-He relationship for turbulent flow.

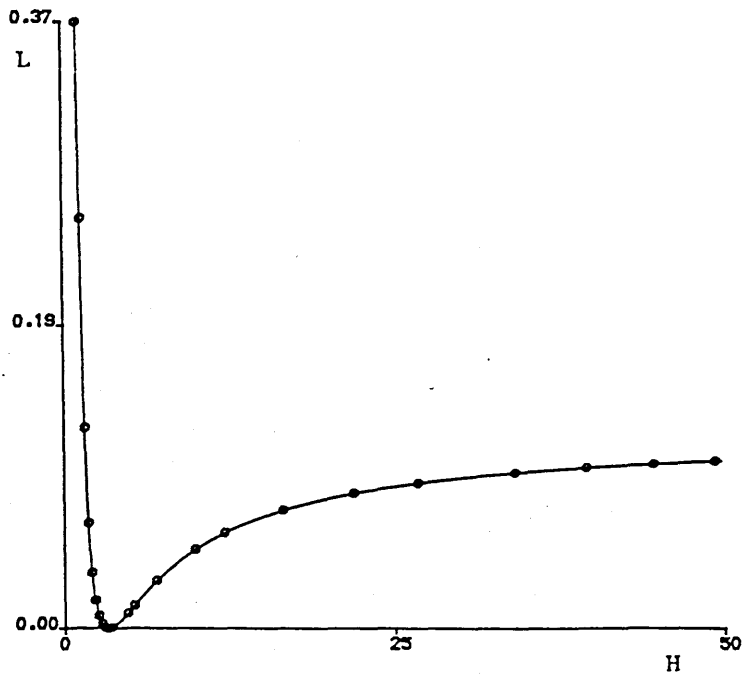


Fig. 5.25 Spline-fit representation of the calculated H-L relationship for turbulent flow.

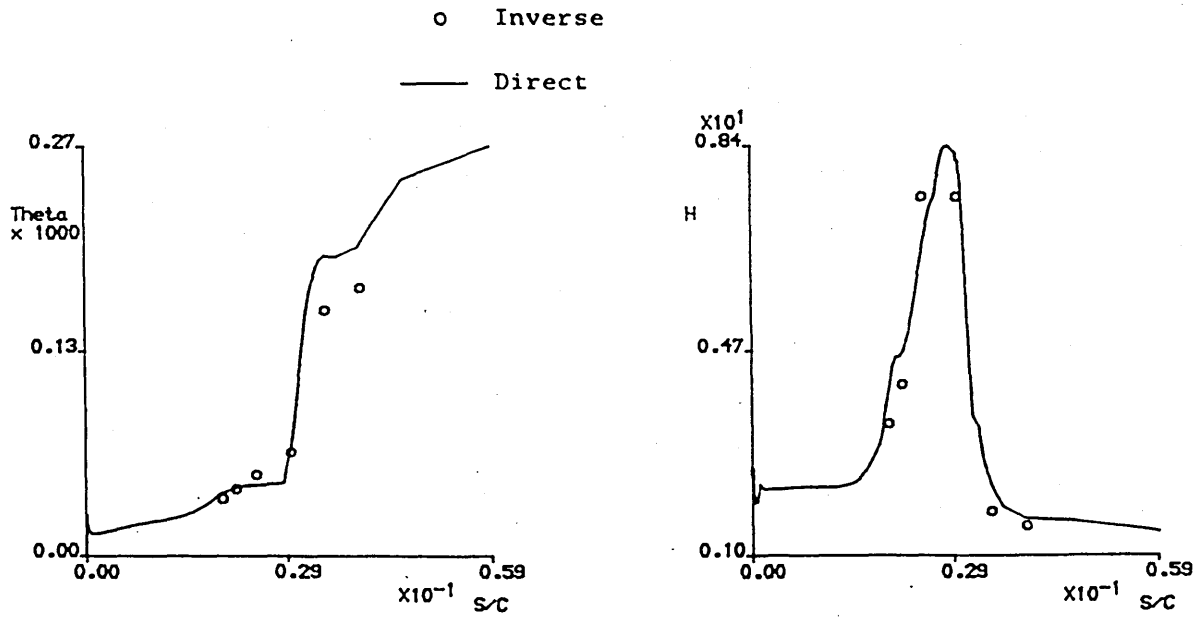
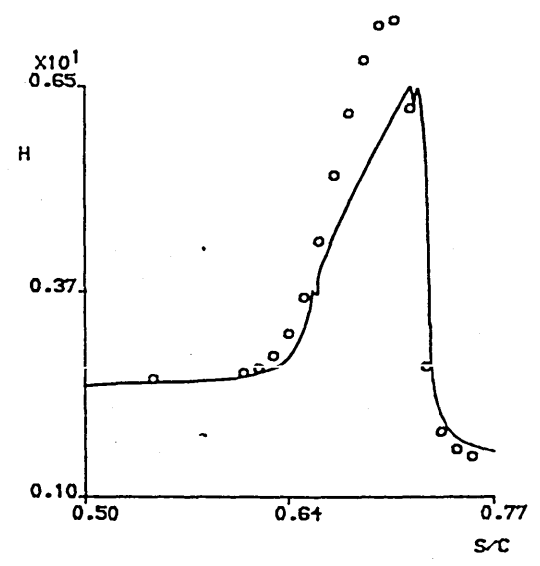
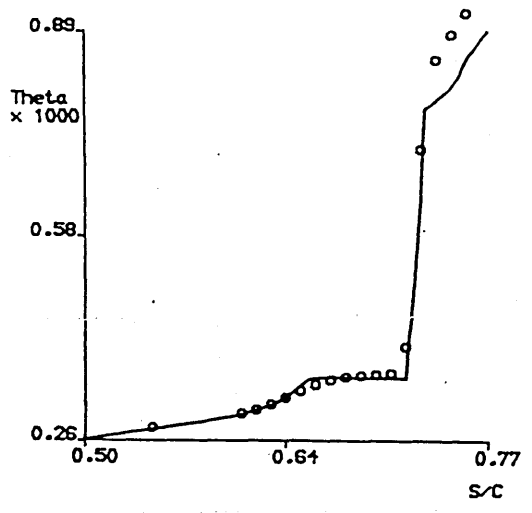
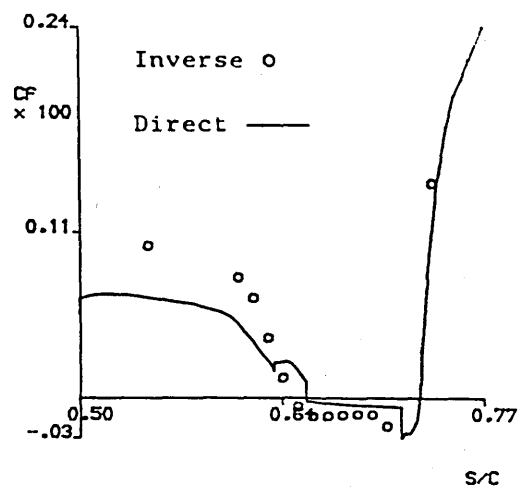
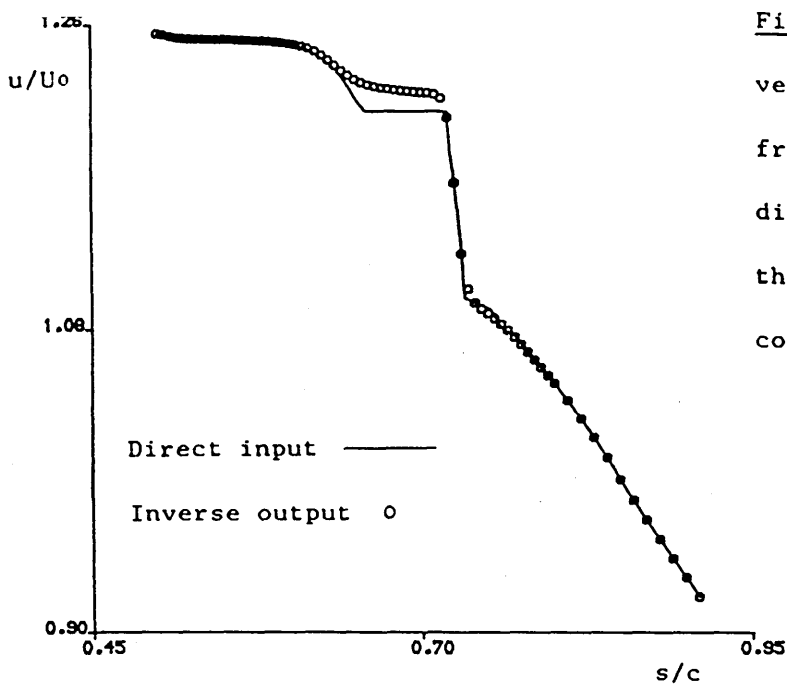


Fig. 5.26 Momentum thickness and form parameter predictions compared with the inverse solution for the enlarged leading edge case of Gleyzes et al.



to separation.

bubble.

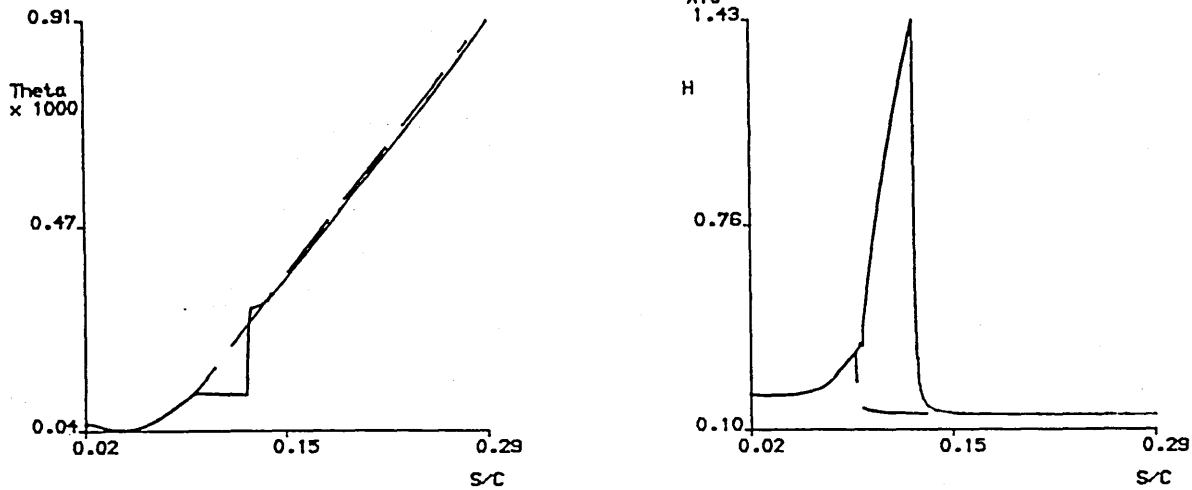


Fig. 5.29 Comparison between the boundary layer parameter predictions obtained for the NACA 4415 aerofoil, $Re = 1 \times 10^6$, $\alpha = 14.5^\circ$, for transition just prior to separation, and for the separated flow velocity distribution given by Horton's method.

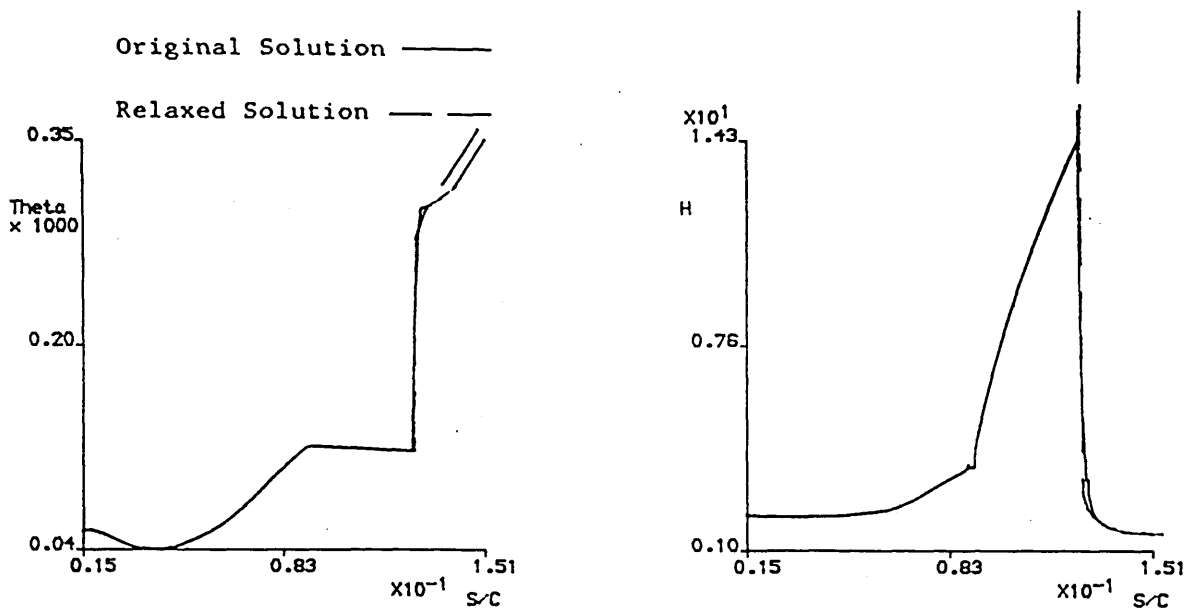


Fig. 5.30 Comparison between the boundary layer parameter predictions obtained for the NACA 4415 aerofoil, $Re = 1 \times 10^6$, $\alpha = 14.5^\circ$, for the separated flow velocity distribution given by Horton's method as calculated, and with relaxation at transition.



Fig. 6.1 GU25-5(11)8 aerofoil profile.

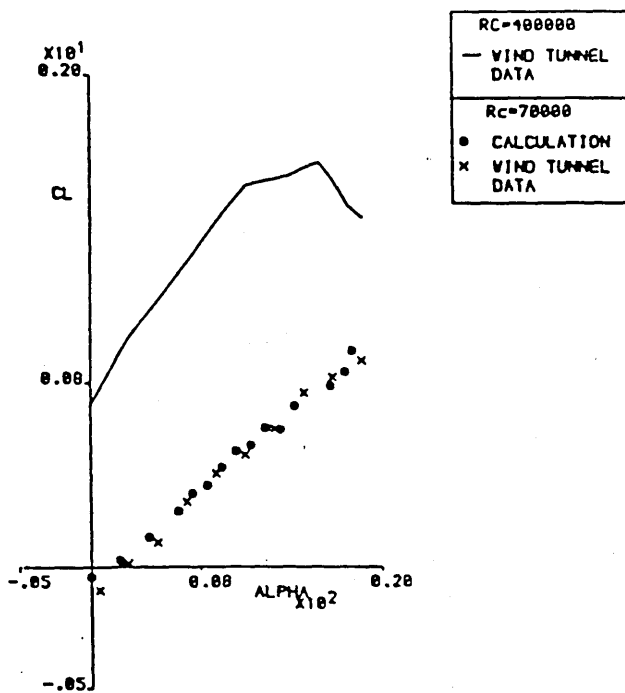


Fig. 6.2 Measured lift coefficient variation for the GU25-5(11)8 aerofoil at $Rc = 4 \times 10^5$ compared with the calculated and measured variations at $Rc = 7 \times 10^4$.

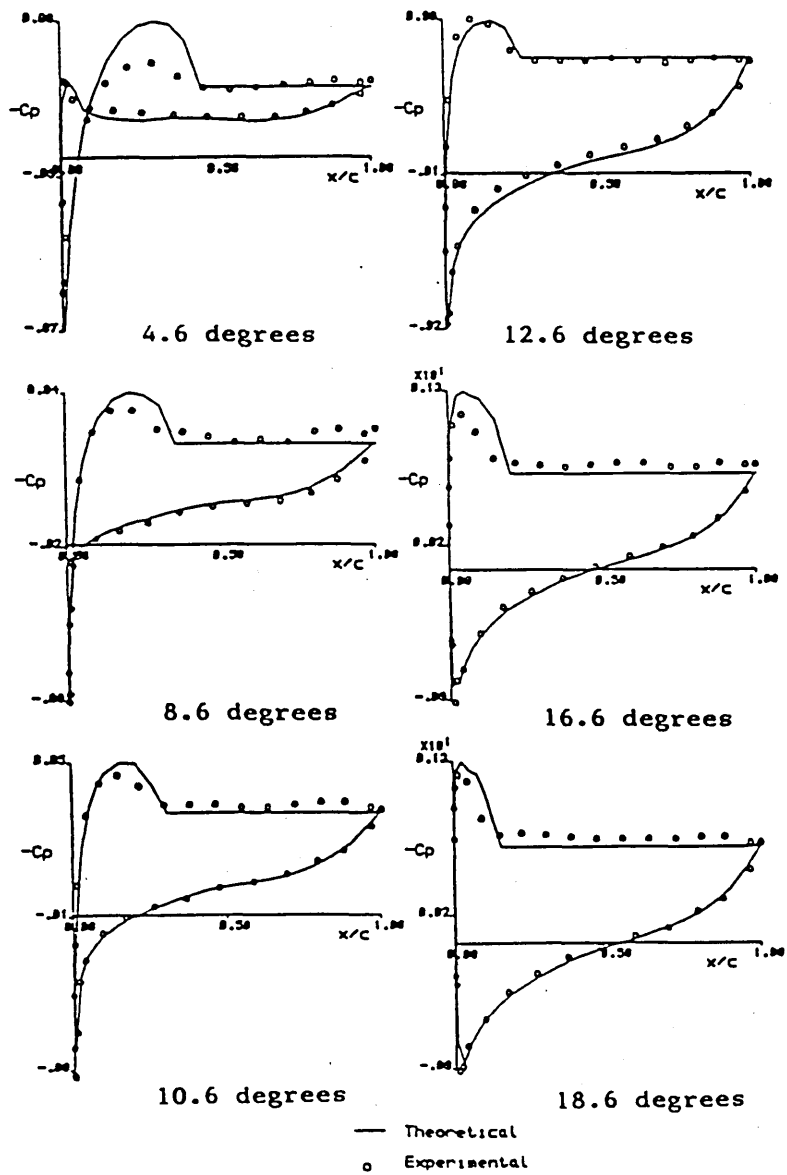


Fig. 6.3 Measured and calculated pressure coefficient distributions for the GU25-5(11)8 aerofoil at six angles of attack, $R_c = 7 \times 10^4$.

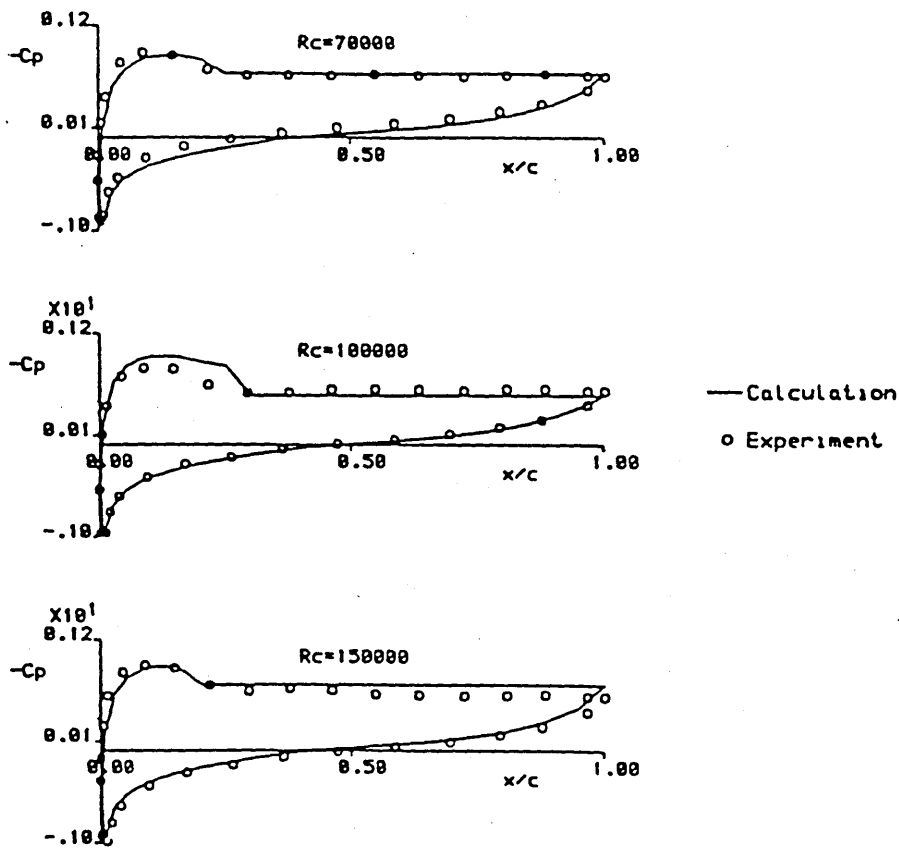


Fig. 6.4 Measured and calculated pressure coefficient distributions for the GU25-5(11)8 aerofoil for three Reynolds numbers, $\alpha = 12.6$ degrees.

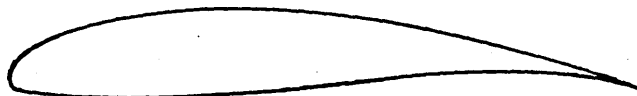


Fig. 6.5 Wortmann FX63-137 aerofoil profile

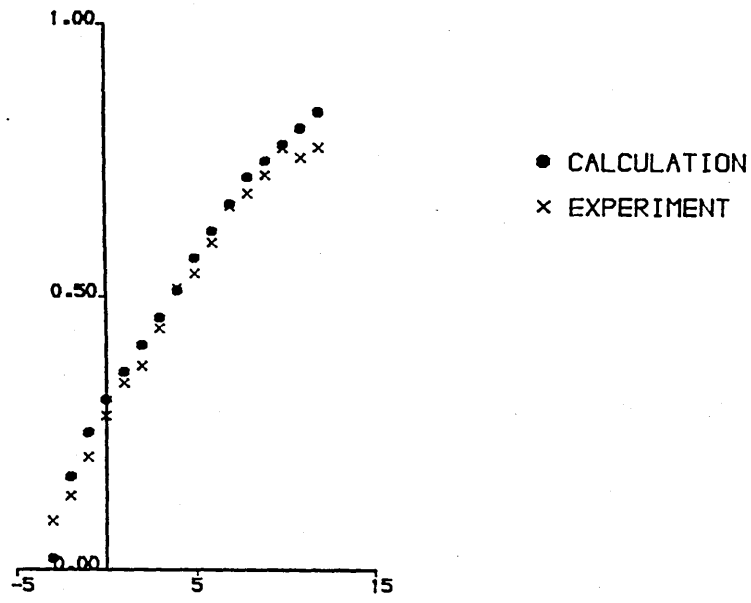


Fig. 6.6 Measured and calculated lift curves for the Wortmann FX63-137 aerofoil at $Re = 60000$.



Fig. 6.7 GA(W)-1 aerofoil profile.

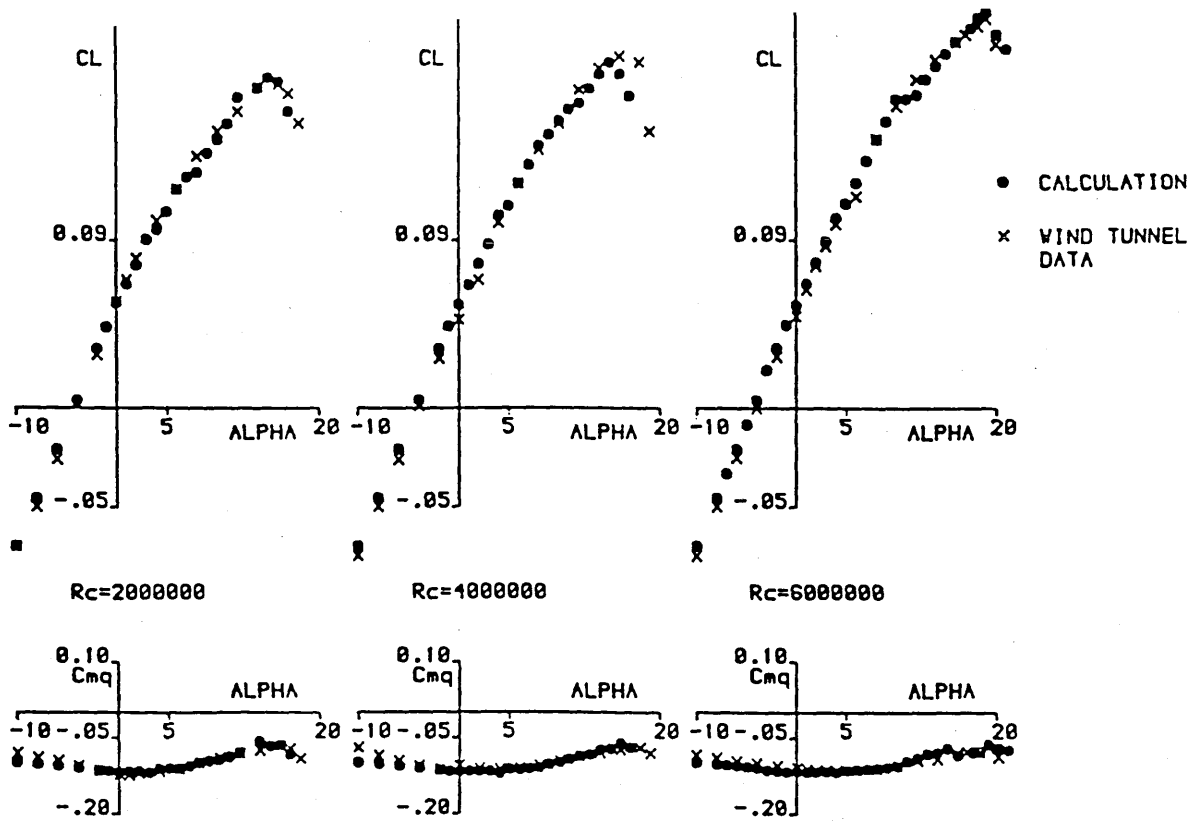


Fig. 6.8 Comparisons of calculated lift and pitching moment coefficient variations with wind tunnel data, for the GA(W)-1 aerofoil at three Reynolds numbers.

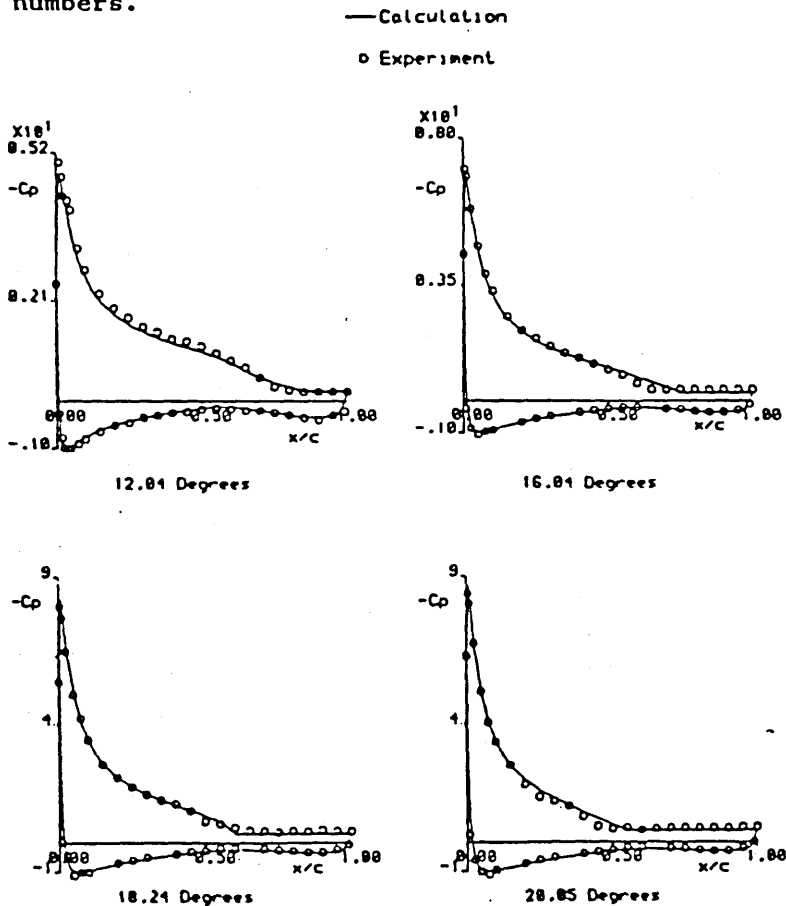
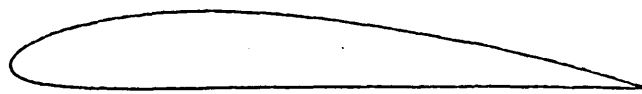
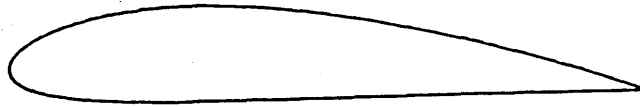


Fig. 6.9 Comparison of measured and calculated pressure coefficient distributions for the GA(W)-1 aerofoil at four angles of attack,

$Rc = 6 \times 10^6$.



4412



4415

Fig. 6.10 NACA 4412 and 4415 aerofoil sections.

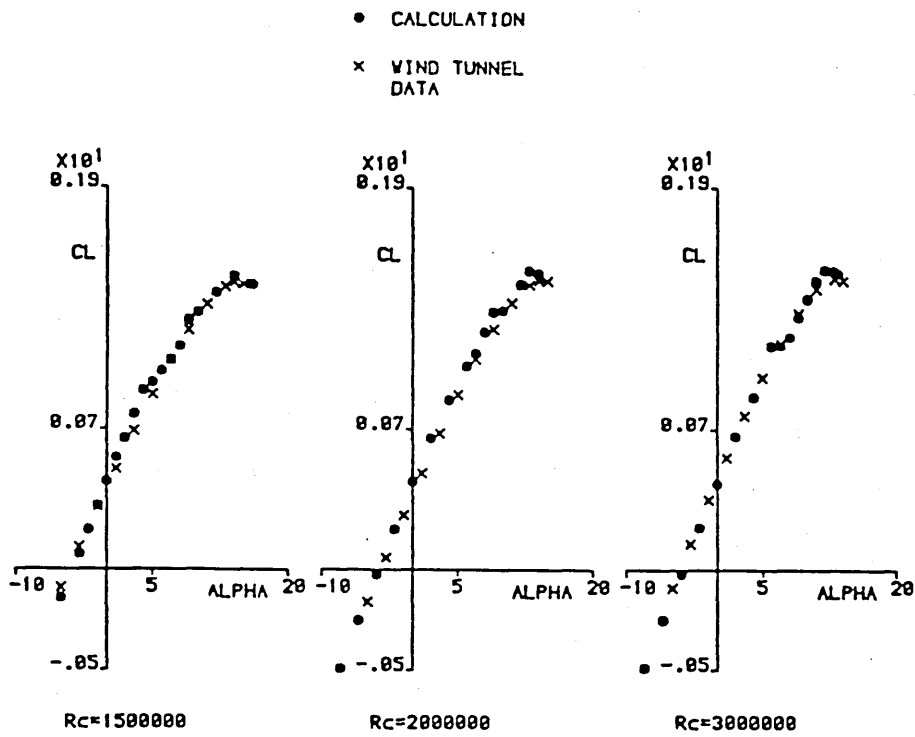


Fig. 6.11 Comparison of calculated lift coefficients with wind tunnel data for the NACA 4412 aerofoil at three Reynolds numbers.

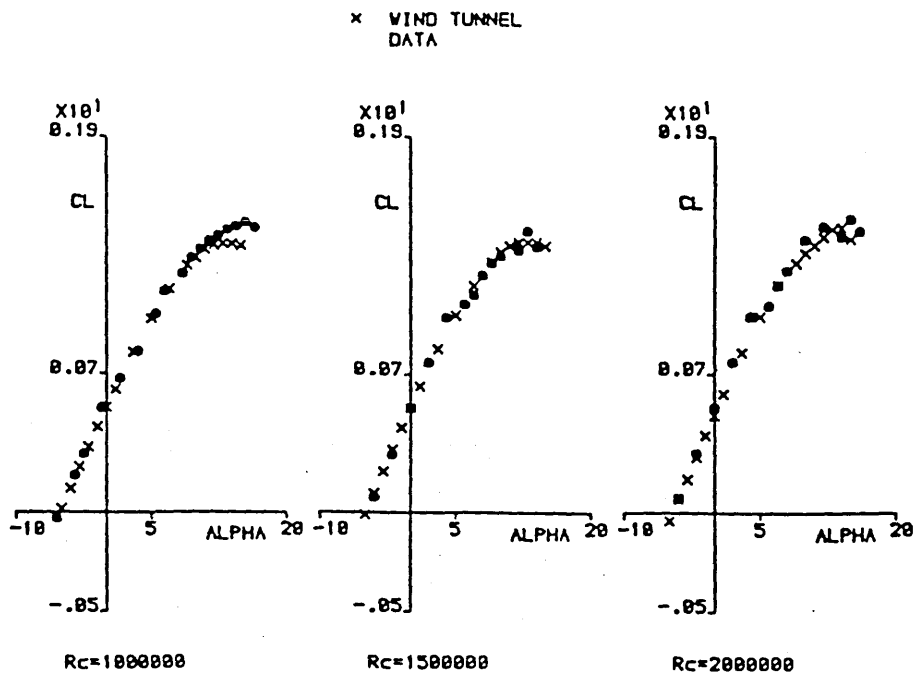


Fig. 6.12 Comparison of calculated lift coefficients with wind tunnel data for the NACA 4415 aerofoil at three Reynolds numbers.

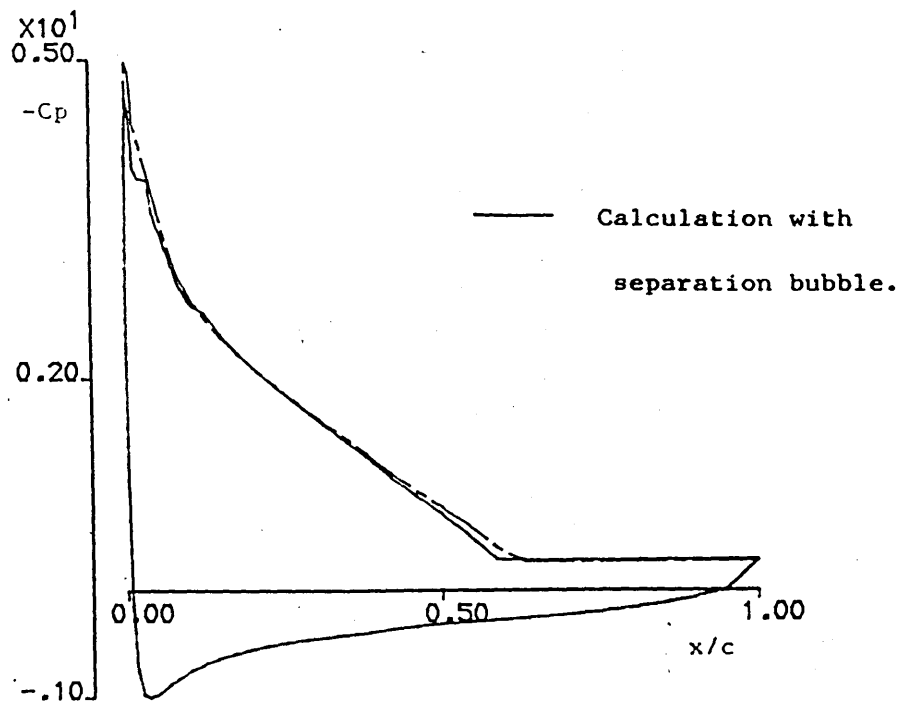


Fig. 6.13 Calculated pressure distributions for the NACA 4415 aerofoil at 14.5 degrees, $Rc = 10^6$, with and without separation bubble effects.



Fig. 6.14 NACA 23012 aerofoil profile.

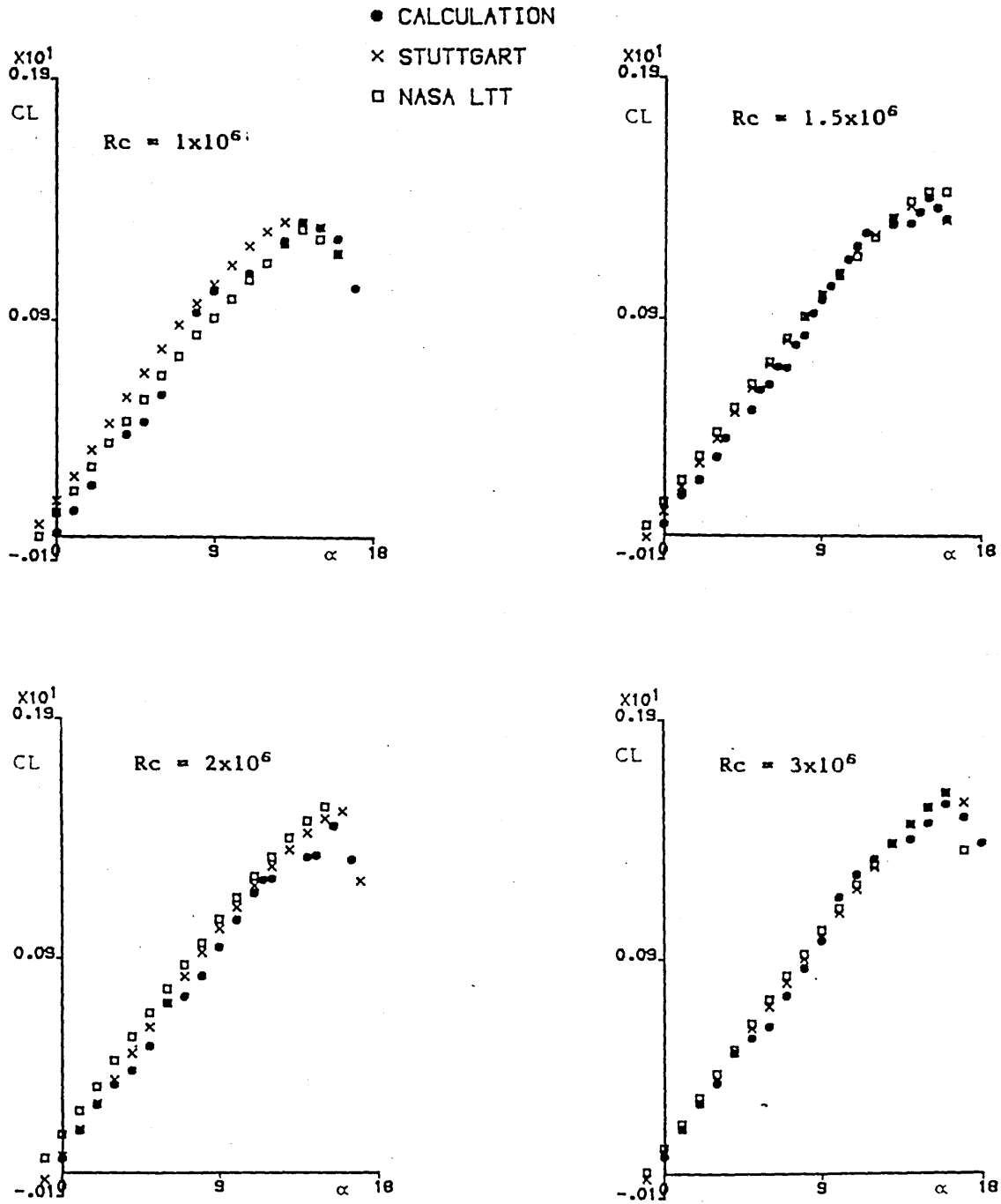


Fig. 6.15 Calculated lift coefficients for the NACA 23012 aerofoil at four Reynolds numbers, compared with two empirical data sources.

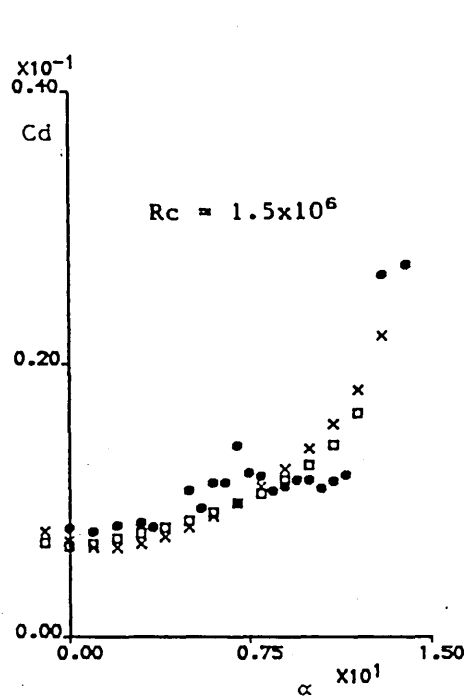
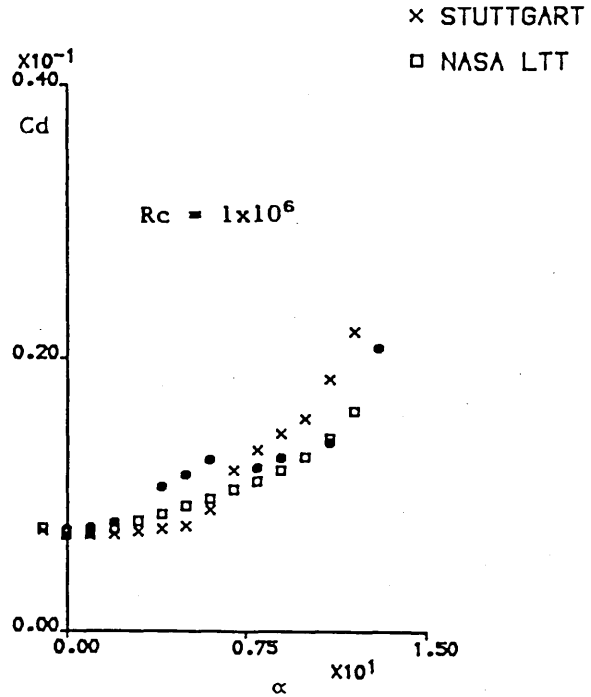


Fig. 6.16 Calculated drag coefficients for the NACA 23012 aerofoil at two Reynolds numbers, compared with two empirical data sources.



Fig. 6.17 Gottingen 797 aerofoil section.

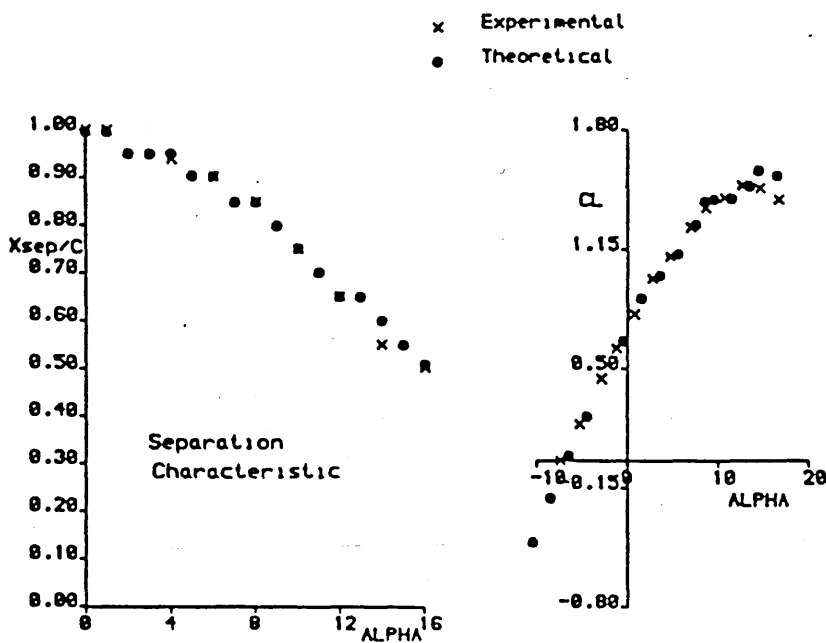


Fig. 6.18 Measured and calculated lift and separation characteristics for the GÖ 797 aerofoil,,
 $Rc = 1 \times 10^6$

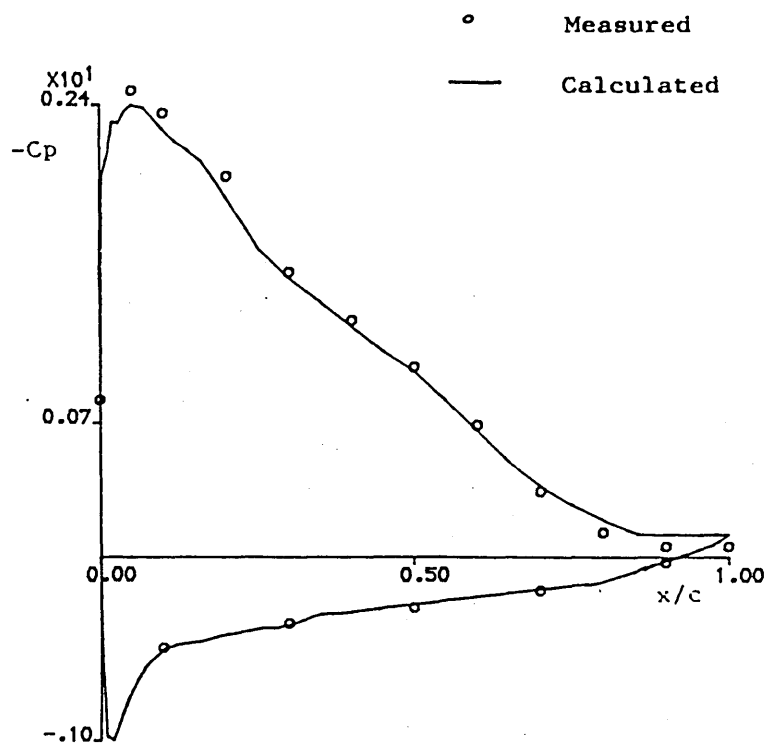


Fig. 6.19 Measured and calculated pressure coefficient distribution for the GÖ 797 aerofoil at 8 degrees, $R_c = 1 \times 10^6$.

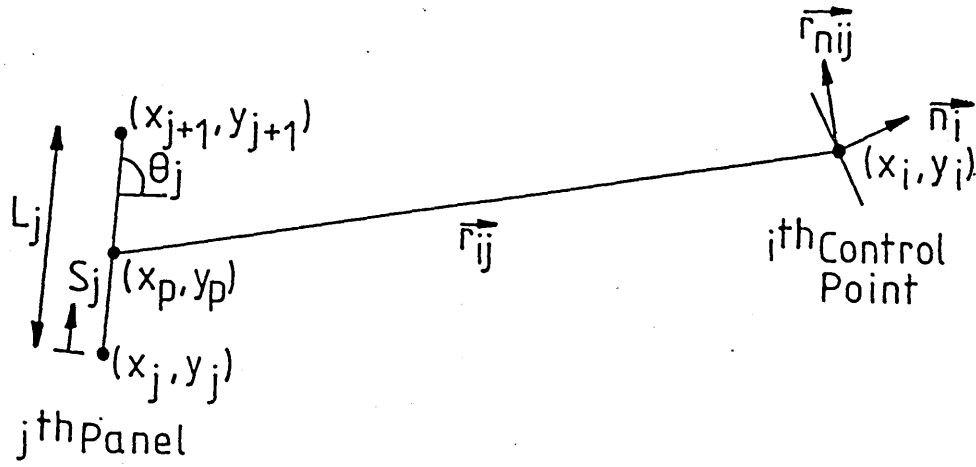


Fig. A1 Parameters for influence coefficient calculation.

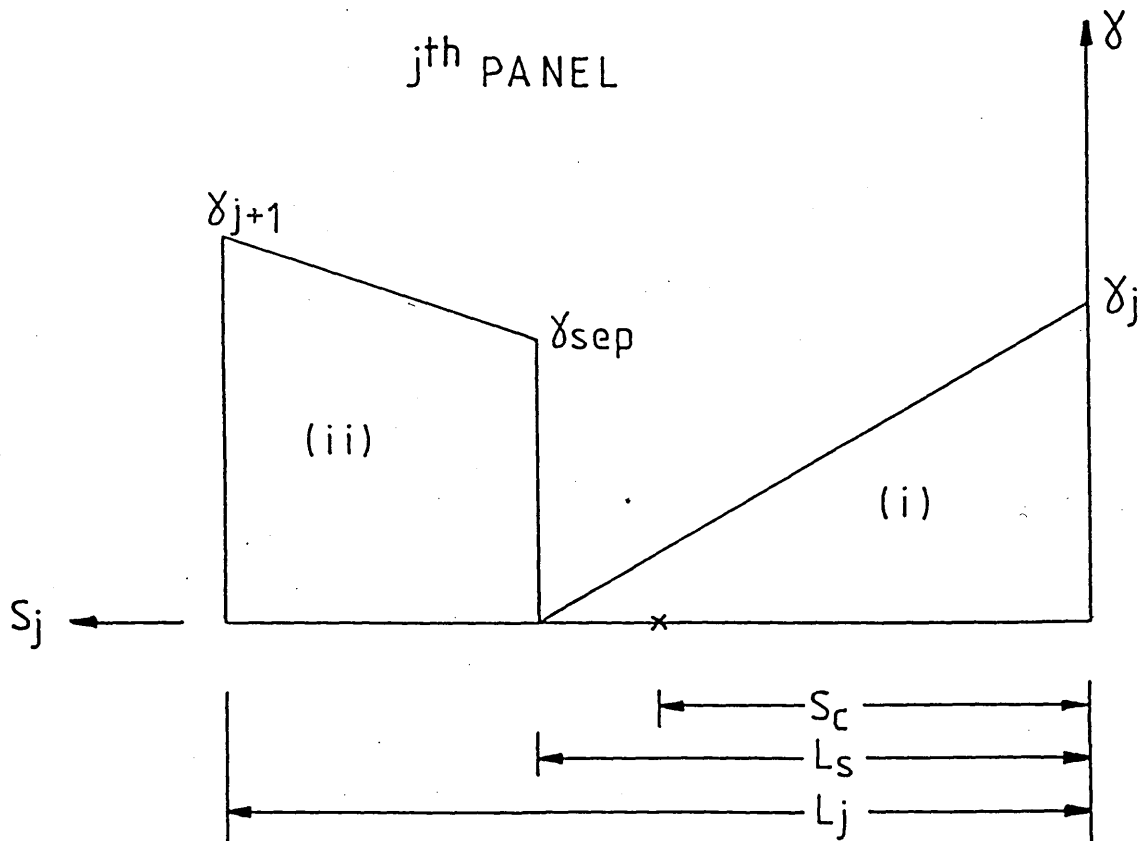


Fig. A2 Vorticity distribution on the separation panel.

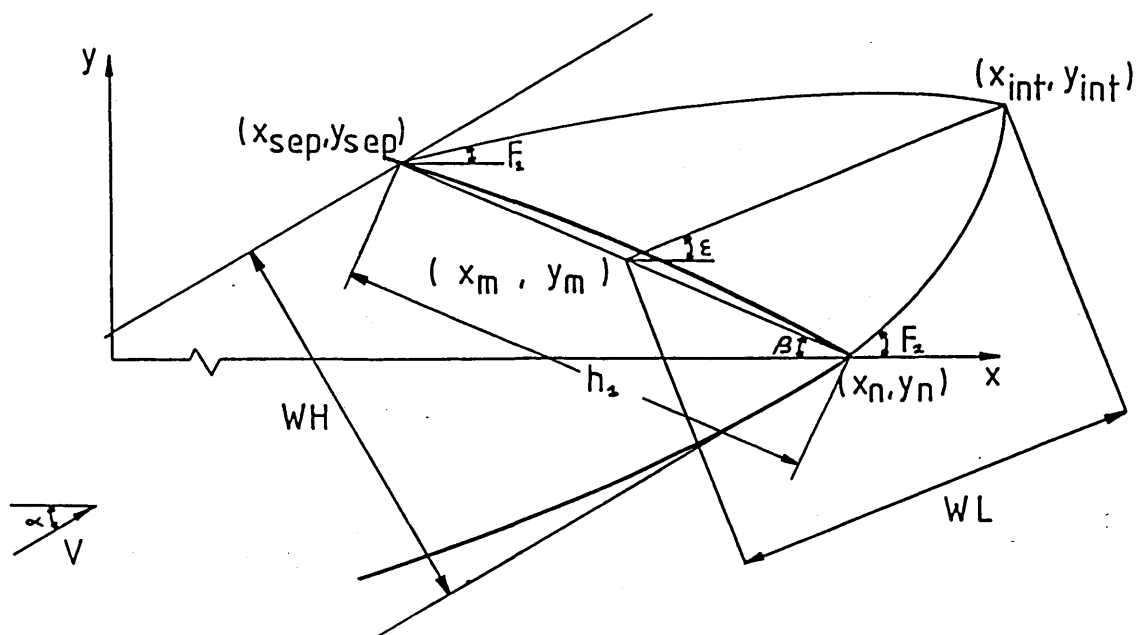


Fig. A3 Wake Factor calculation parameters.

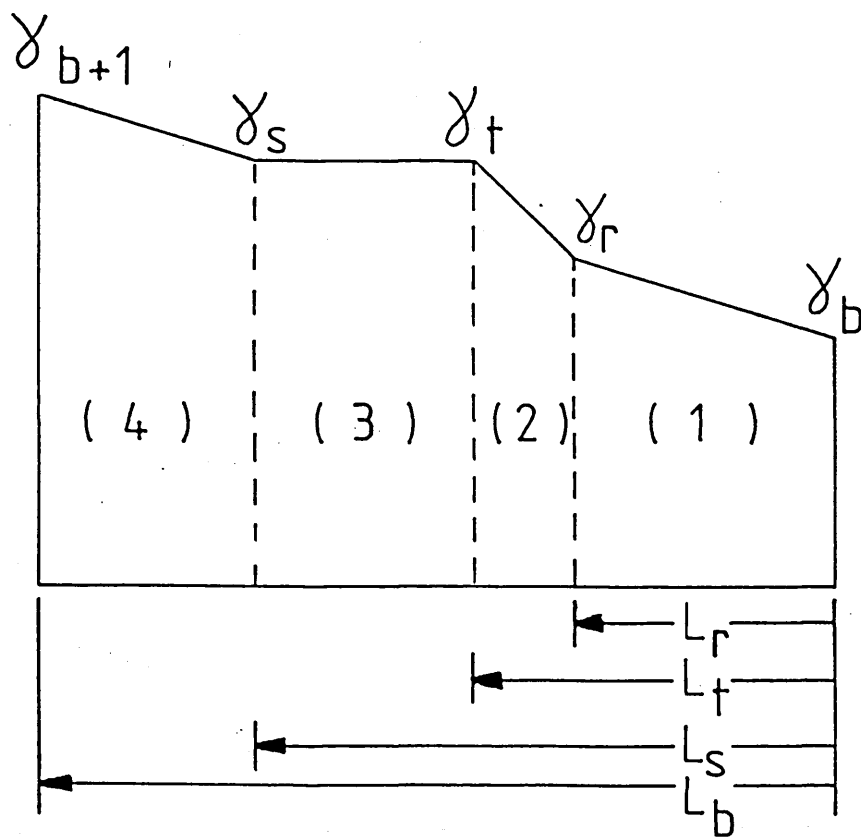


Fig. A4 Imposed vorticity distribution on 'bubble' panel.

GLASGOW
UNIVERSITY
LIBRARY